Title

First-principles studies of carbon nanostructures and spin-phonon and electron-phonon coupling in solids

Author

Chan, Kevin Timothy

Publication Date

2012

First-principles studies of carbon nanostructures and spin-phonon and electron-phonon coupling in solids

by

Kevin Timothy Chan

A dissertation submitted in partial satisfaction of the

requirements for the degree of

Doctor of Philosophy

in

Physics

in the

Graduate Division

of the

University of California, Berkeley

Committee in charge:

Professor Marvin L. Cohen, Chair
Professor Michael F. Crommie
Professor Daryl C. Chrzan

Fall 2012

First-principles studies of carbon nanostructures and spin-phonon and
electron-phonon coupling in solids

Abstract

First-principles studies of carbon nanostructures and spin-phonon and electron-phonon coupling in solids

by

Kevin Timothy Chan

Doctor of Philosophy in Physics

University of California, Berkeley

Professor Marvin L. Cohen, Chair

This work presents first-principles theoretical studies on two topics of condensed matter physics. The first topic is the adsorption of metal adatoms on graphene. Graphene, a two-dimensional material made of carbon atoms arranged in a honeycomb lattice, has many outstanding properties that can be enhanced or tailored by adsorbing adatoms on its surface. The second topic involves the coupling of spins or electrons to phonons in a solid. The interaction between different degrees of freedom of a material complicates the study of its properties but also leads to fascinating phenomena, such as superconductivity, and potential device applications. This dissertation is organized into six chapters:

- In Chapter One, we give an overview of this work and review the first-principles theory and methods used in our studies.

- Chapter Two focuses on structural, energetic, and electronic properties for a variety of adatom species adsorbed on the graphene surface. We classify different species as having mostly ionic or covalent character of bonding to graphene. For ionically bonded adatoms, charge transfer between the adatom and graphene is signficant. We find general trends relating the surface dipole moment, work function, and atomic ionization potential of the adatom species.

- In Chapter Three, we study the electronic structure of adatoms on graphene when a gate voltage is applied to control the number of electrons in the system. Lithium on graphene, a prototype system, and cobalt on graphene, an experimentally relevant case, are studied. We find that localized states on the adatom can be charged or discharged by the application of gate voltage, and we study the changes in potential and charge density of the system as electrons are added or removed.

- In Chapter Four, we extend the work in Chapter Three to consider the possibility of transforming the electronic structure of one species of adatom on graphene into that of another by applying a gate voltage. We find that within our model, such transformations are possible for certain adatom species.

- In Chapter Five, the zone-center phonons for the frustrated antiferromagnetic compound $ZnCr_2O_4$ are calculated. We find that the transition from nonmagnetic to antiferromagnetic ordering causes a splitting of certain degnerate phonon frequencies, in agreement with experimental results.
- In Chapter Six, the pressure dependence of electron-phonon coupling and the superconducting transition temperature (T_c) in elemental arsenic is studied. We find that an experimentally observed peak in T_c as a function of pressure is related to a structural transition and can be explained mainly by changes in electronic structure and phonon frequencies with pressure.

For my family: Mom, Dad, and Brian.

Contents

List of Figures

List of Tables

Acknowledgments

Most importantly, I thank my advisor, Marvin Cohen, for his support, guidance, and especially patience as I dealt with challenges, both in physics and in life, during the Ph.D. process. I am grateful for what I have learned from him about physics, scientific research, and being human.

I feel fortunate to have had the opportunity to collaborate with brilliant and caring physicists: Jay Sau, Peihong Zhang, Jeff Neaton, Hoonkyung Lee, and Brad Malone. I am also grateful to the other members of the Cohen and Louie groups, especially Jonathan Moussa, Jesse Noffsinger, Timur Bazhirov, Young-Woo Son, Feliciano Giustino, Li Yang, Filipe Ribeiro, Georgy Samsonidze, Sinisa Coh, Manos Kioupakis, Cheol Hwan Park, Jack Deslippe, David Strubbe, Sangkook Choi, David Prendergast, Manish Jain, and others. Thank you for your gifts of time, energy, conversation, and knowledge.

I thank Katherine de Raadt for all her help with the administrative tasks which are very important but often overlooked, and those experimentalists who taught me a bit about their work, especially Gavi Begtrup, Victor Brar, and Kwanpyo Kim.

This research was supported by the National Science Foundation and the U.S. Department of Energy. Computational resources were provided by NSF through TeraGrid and by DOE at Lawrence Berkeley National Laboratory's NERSC facility, Molecular Foundry, and Lawrencium computational cluster resource.

Chapter 1

Introduction

1.1 Overview

Condensed matter physics is a broad field encompassing the study of crystalline and disordered solids, surfaces, and molecules, as well as liquids, gases, and fluids. These systems are often called, generally, materials. Materials are encountered by humans in their daily lives and are an important part of the observable natural world. It is a human endeavor to understand how the natural world works, and how materials work in particular. Such understanding also leads to useful applications. The study of condensed matter physics is therefore a worthwhile pursuit.

Condensed matter systems range from the macroscopic to the nanometer and Angström scale. What unifies all the varied condensed matter systems is that they are all made up of constituent particles—nuclei and electrons—that interact via the electromagnetic force. While, at some level, the fundamental particles and interactions are simple, the variety of possible combinations of species of atoms and structures leads to a host of complex phenomena that invite us to understand them.

This thesis is concerned with several interesting phenomena of condensed matter physics. The first set of phenomena relates to a class of materials made of sp^2 carbon atoms. This class of materials has several outstanding properties. These materials are stable and strong, due to the strength of the sp^2 carbon bond. Graphite, the three-dimensional form of sp^2 carbon, is found naturally and is the most stable form of solid elemental carbon. The simple structure of these materials, based on the two-dimensional honeycomb lattice, possesses many symmetries. Since these materials are made of carbon, which has four valence electrons, they are capable of interacting with other elements and molecules. These materials can also form a variety of structures of different dimensionalities. Nanometer scale (on the order of tens or hundreds of atoms in length) sp^2 carbon-based materials are stable and have interesting quantum mechanical properties that are not observable in macroscopic materials.

Graphite is composed of layered sheets of carbon atoms in a two-dimensional honeycomb lattice. A single layer of graphite is called graphene. If one imagines taking a piece of graphene and forming it into a ball, one obtains a zero-dimensional object. The C_{60} molecule, or "buckyball", was discovered in 1985 [1]. The one-dimensional carbon nanotube, which can be thought of as a rolled up graphene ribbon, was dicovered a few years later [2].

The ability to efficiently isolate and study two-dimensional graphene in detail was discovered only recently [3]. Graphene posesses many unique properties and has been the subject of intense study in the last several years [4, 5]. In addition to its excellent strength and conducting properties which are also characteristic of carbon nanotubes, ideal graphene is a truly two-dimensional, one atom thick material; it is a semimetal with a pointlike Fermi surface; it posseses a linear electronic band dispersion and a linearly varying density of states near the Fermi level; and electrons at the Fermi level obey a Dirac-like equation analogous to relativistic particles. Chapters 2–4 of this thesis focus on graphene.

Chapter 5 of this thesis deals with a specific problem relating to the general phenomenon of magnetism. While magnetic materials have been known for a long time, they are still rich topic of current research. The interactions between microscopic magnetic moments in materials are not fully understood, as they involve the difficult problem of electron correlation [6]. These interactions lead to ferromagnetic, antiferromagnetic, and other types of long range magnetic order.

Materials synthesis and characterization advances have increased the number of magnetic materials available. Multiferroics, materials that couple magnetic to electric or mechanical degrees of freedom, are an especially exciting current topic of research and may have useful applications [7, 8]. Computer hard drives relying on the phenomenon of giant magnetoresistance [9] are a well-known application of magnetic materials.

Electron-phonon coupling is central to several properties of materials, most notably the temperature dependence of electrical resistivity and superconductivity. Superconductivity is one of the most fascinating topics in condensed matter physics. It was discovered in 1911 by Kamerlingh Onnes [10], but the microscopic theory of superconductivity was unknown until the work of Bardeen, Cooper, and Schrieffer (BCS) in 1957 [11]. In conventional superconductors, electron-phonon coupling is responsible for electron pairing. Since BCS, the active study of electron-phonon superconductors has continued; a few important recent results include the discoveries of surprisingly high superconducting transition temperatures in MgB_2 [12] and elemental lithium under pressure [13–15].

Since all materials are composed of nuclei and electrons, whose individual properties are known, and that interact via the well-known electromagnetic force, an ideal hope is to be able to determine theoretically all the properties of any condensed matter system from knowledge of its constituent atoms. While a complete understanding of all condensed matter from an atomistic perspective is not possible (at least, not yet), at the present it is possible to calculate many properties of many systems from first-principles, using only the identity of the atoms and their structure, with little or no empirical input.

The first-principles theoretical approach has proven very fruitful in understanding condensed matter systems. With current computer technology, such calculations can be made with high quantitative precision, allowing for valuable comparisons with experimental results. In addition, the accuracy of the first-principles approach makes it useful for making real predictions about materials, both existing and hypothetical, that subsequently can be verified experimentally.

This dissertation describes the application of first-principles theoretical methods to two classes of problems in condensed matter physics. The first class of problems involves developing our understanding of the adsorption of metal adatoms on graphene. There are a wide variety of metals that can be adsorbed on graphene to form different structures and modify the properties of graphene in interesting and useful ways. In Chapter 2, we study the total energy and electronic properties of adatoms adsorbed on graphene for a variety of metal species. We find that many adatoms have a binding energy of around 1 eV. We can classify different adatom species as having mainly ionic or covalent bonding character. For adatoms that bind ionically, we calculate the charge transfer between the adatom and the graphene. We study the relation between ionization energy of the isolated atom and the changes in work function and surface dipole moment when the adatom is adsorbed on the graphene sheet.

In Chapter 3, we study the adatom-graphene system when the number of electrons in the system is varied. Experimentally, the control of electron density in the graphene system can be achieved by applying a gate voltage, and the system can be simultaneously studied by scanning tunneling microscopy [16]. Calculations are performed for a lithium adatom on graphene, which serves as a prototype system, and for cobalt on graphene, a system that has been studied experimentally [17]. We find that applying a gate voltage to the adatom-graphene system can cause charging and discharging of localized adatom states, and we study the changes in potential and electron density due to this charging effect.

In Chapter 4, we explore the possibility of using gate voltage control to transform the electronic properties of one species of adatom on graphene into those of its neighbor in the Periodic Table. Transforming between potassium and calcium, cobalt and nickel, and nickel and copper are considered. Within our model, we find that this transformation, termed "alchemy", is possible in several cases.

The second class of problems involves the coupling of spins or electrons to phonons in solids. In Chapter 5, we study the compound $ZnCr_2O_4$, which is a frustrated antiferromagnet. Our first-principles calculations of phonon frequencies in this material show that phonon modes that are degenerate in frequency when no magnetic order is present are split when antiferromagnetic order is introduced. We explore different models for correlation in this system, and show that effects of correlation, in the form of a Hubbard U, are needed to get good agreement of phonon splittings with experimental results.

In Chapter 6, we study electron-phonon and superconductivity in elemental arsenic under pressure. Experimentally, arsenic is known to undergo a transition from the rhombohedral $A7$ structure to the simple cubic structure at around 25-32 GPa as pressure is increased. Near this transition, arsenic is also superconducting, with a maximum transition temperature of 2.4 K [18]. We calculate the electron-phonon coupling constant λ and superconducting transition temperature at various pressures near this structural transition and find good agreement with experiment. These calculations give physical insight into the reasons for the change in superconducting transition temperature with pressure in this system.

The rest of this introductory chapter (Sec. 1.2) describes the basic theory and first-principles methods used in this thesis. The main studies of this thesis follow in Chapters 2–6.

1.2 Basic theory and methods

In this section, we review the basic framework for studying condensed matter systems from first-principles theory. In Sec. 1.2.1, we first define the fundamental physics of the system by specifying the hamiltonian for electrons and ions interacting via the electromagnetic force. The problem is to solve the Schrödinger equation for the given hamiltonian. With the Born-Oppenheimer approximation, the problem is split into electronic and ionic parts. Solution of the electronic structure problem (Sec. 1.2.2) for fixed ionic positions gives properties such as the total energy, electronic band structure and density of states, and forces on the ions. Two tools for solving the electronic structure problem are reviewed: density functional theory and the plane-wave pseudopotential method. Electronic structure calculations are the basis for all the studies presented in this dissertation. We then present in Sec. 1.2.3 the basic theory for solving for the normal modes of the ions, or phonon modes. Two approaches to phonon calculations are presented: the frozen phonon approach, used in Chapter 5, and density functional perturbation theory, used in Chapter 6. Methods for treating magnetic systems, such as the magnetic adatoms on graphene studied in Chapters 2–4, and the magnetic material $\mathrm{ZnCr_2O_4}$ studied in Chapter 5, are also discussed (Sec. 1.2.4). The last part of this section (Sec. 1.2.5) describes the methods for using electronic structure and phonon calculations to study the electron-phonon interaction and superconductivity; these methods are applied in Chapter 6.

1.2.1 Defining the problem

From an atomistic perspective, a solid or molecule is a collection of negatively charged electrons and positively charged ions. The system is governed by the Schrödinger equation of quantum mechanics:

$$\hat{H}_{\text{Full}}\Psi_{\text{Full}} = E_{\text{Full}}\Psi_{\text{Full}}, \tag{1.1}$$

where $\hat{H}_{\text{Full}}$ is the full hamiltonian of the system, E_{Full} is the energy of the system, and Ψ_{Full} is the wavefunction for all the particles.

For a system with N_e electrons and N_i ions, we denote the positions of the particles by $\{\boldsymbol{r}\} = \{\boldsymbol{r}_1, \dots \boldsymbol{r}_{N_e}\}$ for the electrons and $\{\boldsymbol{R}\} = \{\boldsymbol{R}_1, \dots \boldsymbol{R}_{N_i}\}$ for the ions. (In this section, a bold variable denotes a vector in three-dimensional space.) The wavefunction $\Psi_{\text{Full}} = \Psi_{\text{Full}}(\{\boldsymbol{r}\}, \{\boldsymbol{R}\})$ is a function of the positions of all the particles. Throughout this section, we use lowercase and uppercase letters for electron and ion indices, respectively.

The Hamiltonian is given by

$$\begin{aligned}\hat{H}_{\text{Full}} &= -\sum_I \frac{\hbar^2}{2M_I}\boldsymbol{\nabla}_I^2 - \sum_i \frac{\hbar^2}{2m}\boldsymbol{\nabla}_i^2 + \frac{1}{2}\sum_{i\neq j}\frac{e^2}{|\boldsymbol{r}_i - \boldsymbol{r}_j|} + \frac{1}{2}\sum_{I\neq J}\frac{Z_I Z_J e^2}{|\boldsymbol{R}_I - \boldsymbol{R}_J|} - \sum_{I,i}\frac{Z_I e^2}{|\boldsymbol{r}_i - \boldsymbol{R}_J|} \\ &= \hat{T}_{\text{ion}} + \hat{T}_{\text{el}} + \hat{V}_{\text{el-el}} + \hat{V}_{\text{ion-ion}} + \hat{V}_{\text{el-ion}}. \end{aligned} \tag{1.2}$$

The sums are over all the particles in the system, M_I denotes the mass of ion I, m is the electron mass, e is the electron charge, and Z_I is the charge of ion I, in units of e. The first two terms are the kinetic energies of the ions and electrons, respectively, while the last three terms are the coulomb energies for the electron-electron, ion-ion, and electron-ion interaction. Relativistic effects, which are small for the systems we study, are ignored.

This complicated many-particle system cannot be solved exactly except for a small number of particles. Therefore, several approximations must be made to get a solution. The first approximation we make is to separate the electronic and ionic motion. This is generally referred to as the Born-Oppenheimer or adiabatic approximation [19].

The basic idea is that, since the ionic mass M is much larger than the electronic mass m in most systems, the motion of the electrons is much faster than that of the ions, and we can consider the motions of these two sets of particles separately. The Born-Oppenheimer approximation is justified formally by expanding the Hamiltonian in powers of $(m/M)^{1/4}$.

When considering the motion of the electrons, the ions can be considered as static, i.e., the kinetic energy of the ions is zero. The positions of the ions can be considered as parameters; for fixed $\{\boldsymbol{R}\}$, the hamiltonian for the electrons is

$$\hat{H}_{\text{el}}(\{\boldsymbol{R}\}) = \hat{T}_{\text{el}} + \hat{V}_{\text{el-el}} + \hat{V}_{\text{el-ion}}(\{\boldsymbol{R}\}) + \hat{V}_{\text{ion-ion}}(\{\boldsymbol{R}\}). \tag{1.3}$$

This hamiltonian can be solved for electronic wavefunctions $\{\Psi_n(\{\boldsymbol{r}\},\{\boldsymbol{R}\})\}$ and eigenvalues $\{E_n(\{\boldsymbol{R}\})\}$. The solution of this electron hamiltonian is the electronic structure problem. Some fundamental methods in first-principles electronic structure theory are discussed in Sec. 1.2.2.

When considering the motions of the ions, the electrons are assumed to respond instantaneously. The motion of the ions is adiabatic, such that the the electrons retain their same quantum numbers as the ions move. The hamiltonian for the ions, with electrons in state n, is

$$\hat{H}_{\text{ion}} = \hat{T}_{\text{ion}} + E_n(\{\boldsymbol{R}\}); \tag{1.4}$$

$E_n(\{\boldsymbol{R}\})$ acts as an effective potential energy for the ions. This hamiltonian can be solved for the ionic wavefunctions and eigenvalues $\{\chi_{\nu n}(\{\boldsymbol{R}\}), E_{\nu n}\}$; ν indexes the ionic eigenstates. The full wavefunction for both ions and electrons is

$$\Psi_{\text{Full},\nu n}(\{\boldsymbol{r}\},\{\boldsymbol{R}\}) = \chi_{\nu n}(\{\boldsymbol{R}\})\Psi_n(\{\boldsymbol{r}\},\{\boldsymbol{R}\}). \tag{1.5}$$

Quantizing the motion of the ions leads to a description in terms of phonons. Methods for computing phonon modes in condensed matter systems are discussed in Sec. 1.2.3.

For phenomena where the Born-Oppenheimer approximation fails, such as in superconductivity, electronic and ionic motions are coupled. As discussed in Sec. 1.2.5, the solutions of the hamiltonians in Eqs. 1.3 and 1.4 serve as the starting point for computing the electron-phonon interaction.

1.2.2 Electronic structure

The solution of the hamiltonian of Eq. 1.3 is the electronic structure problem; from this solution, one can determine quantities such as the total energy, the electronic band structure and density of states, and the forces on ions. Throughout this section, we assume fixed $\{\boldsymbol{R}\}$, so we drop this notation, and we use atomic units, so that $\hbar = m = e = 1$.

We discuss two important theoretical tools used in the electronic structure problem: density functional theory and the plane-wave pseudopotential method. We also show how forces on the ions can be calculated from density functional theory.

Density functional theory

The main idea and utility of density functional theory (DFT) [20,21] is the following. Instead of trying to find the full many-body wavefunction of the electrons, a function of all the electron coordinates, we try to find the ground-state density, which is a much simpler function of only one coordinate (the position in space), and from which many relevant physical properties can be determined. In the Kohn-Sham scheme, the true fully interacting ground-state density can be determined by solving a tractable independent-particle problem.

Our discussion roughly follows Ref. [22]. Let us consider a general interacting electron system moving in an external potential $V_{\text{ext}}(\boldsymbol{r})$, whose hamiltonian is

$$\hat{H} = \hat{T} + \hat{V}_{\text{int}} + \hat{V}_{\text{ext}}, \tag{1.6}$$

where we have dropped the subscript on H_{el} and $\hat{T}_{\text{el}}$, and

$$\hat{V}_{\text{ext}} = \sum_i \int V_{\text{ext}}(\boldsymbol{r})\delta(\boldsymbol{r} - \boldsymbol{r}_i)d\boldsymbol{r}. \tag{1.7}$$

For a given state $|\Psi\rangle$, the energy is

$$\begin{aligned} E &= \langle\Psi|\hat{H}|\Psi\rangle = \langle\hat{H}\rangle \\ &= \langle\hat{T}\rangle + \langle\hat{V}_{\text{int}}\rangle + \langle\hat{V}_{\text{ext}}\rangle, \end{aligned} \tag{1.8}$$

and the density is

$$n(\boldsymbol{r}) = \langle\Psi|\hat{n}(\boldsymbol{r})|\Psi\rangle, \tag{1.9}$$

where the density operator is

$$\hat{n}(\boldsymbol{r}) = \sum_{i=1}^{N_e} \delta(\boldsymbol{r} - \boldsymbol{r}_i). \tag{1.10}$$

The first theorem of DFT states that an external potential $V_{\text{ext}}(\boldsymbol{r})$ is uniquely defined by the ground state density $n_0(\boldsymbol{r})$, up to a constant. Since $V_{\text{ext}}(\boldsymbol{r})$ defines the hamiltonian, $n_0(\boldsymbol{r})$ in principle defines all the properties of the system.

The second theorem of DFT states that there exists a universal functional $F[n]$ of the density n such that minimizing the total energy functional

$$E[n] = F[n] + E_{\text{ext}}[n] \tag{1.11}$$

over densities $n(r)$ integrating to N_e electrons gives the ground state density n_0 and the ground state energy $E[n_0]$ for the $V_{\text{ext}}(\boldsymbol{r})$. Here,

$$E_{\text{ext}}[n] = \int V_{\text{ext}}(\boldsymbol{r})n(\boldsymbol{r})d\boldsymbol{r}, \tag{1.12}$$

and

$$F[n] = \langle\hat{T}\rangle + \langle\hat{V}_{\text{int}}\rangle. \tag{1.13}$$

The energies $\langle\hat{T}\rangle$ and $\langle\hat{V}_{\text{int}}\rangle$ are implicitly functionals of n via the Levy-Lieb formulation [22].

Eq. 1.3 describes an interacting electron system, with $\hat{V}_{\text{int}} = \hat{V}_{\text{el-el}}$, and

$$V_{\text{ext}}(\boldsymbol{r}) = \sum_I \frac{Z_I}{|\boldsymbol{r} - \boldsymbol{R}_I|}, \tag{1.14}$$

so the DFT theorems apply. The term $\langle \hat{V}_{\text{ion-ion}} \rangle = E_{\text{ion-ion}}$ is a constant number which we are free to include in our hamiltonian.

The Kohn-Sham ansatz states that the ground state density n_0 for the fully interacting electron system can be obtained by taking the ground state density from the solution of an independent-particle problem. The independent-particle wavefunction is $\Psi_{KS}(\{\boldsymbol{r}\}) = \psi_1(\boldsymbol{r}_1) \dots \psi_{N_e}(\boldsymbol{r}_{N_e})$, and the density is

$$n(\boldsymbol{r}) = \sum_i |\psi_i(\boldsymbol{r})|^2. \tag{1.15}$$

In this scheme, the total energy functional is written as

$$E_{KS}[n] = T_s[n] + E_{\text{ext}}[n] + E_H[n] + E_{XC}[n] + E_{\text{ion-ion}}, \tag{1.16}$$

where

$$E_H[n] = \frac{1}{2} \int \frac{n(\boldsymbol{r})n(\boldsymbol{r}')}{|\boldsymbol{r} - \boldsymbol{r}'|} d\boldsymbol{r} d\boldsymbol{r}' \tag{1.17}$$

is the Hartree energy, and

$$T_s[n] = -\frac{1}{2} \sum_i \int \psi_i^*(\boldsymbol{r}) \boldsymbol{\nabla}^2 \psi_i(\boldsymbol{r}) d\boldsymbol{r} \tag{1.18}$$

is the independent-particle kinetic energy, while $E_{XC}[n]$ is the as-yet unspecified exchange-correlation functional.

The ground state density of the independent-particle problem minimizes the Kohn-Sham total energy functional $E_{KS}[n]$ and therefore is stationary with respect to variations in the wavefunctions. Taking the variation of Eq. 1.16 and applying normalization constraints to the wavefunctions leads to the Kohn-Sham equations:

$$\left[-\frac{1}{2} \boldsymbol{\nabla}^2 + V_{\text{ext}}(\boldsymbol{r}) + V_H(\boldsymbol{r}) + V_{XC}(\boldsymbol{r}) \right] \psi_i(\boldsymbol{r}) = \epsilon_i \psi_i(\boldsymbol{r}), \tag{1.19}$$

where

$$V_{XC}(\boldsymbol{r}) = \frac{\delta E_{XC}[n]}{\delta n} \tag{1.20}$$

and

$$V_H(\boldsymbol{r}) = \int \frac{n(\boldsymbol{r}')}{|\boldsymbol{r} - \boldsymbol{r}'|} d\boldsymbol{r}'; \tag{1.21}$$

or, defining the Kohn-Sham hamiltonian, the single particle kinetic energy operator, and the Kohn-Sham potential by

$$\begin{aligned} \hat{H}_{KS} &= -\frac{1}{2} \boldsymbol{\nabla}^2 + V_{\text{ext}}(\boldsymbol{r}) + V_H(\boldsymbol{r}) + V_{XC}(\boldsymbol{r}) \\ &= \hat{T}_s + V_{KS}(\boldsymbol{r}), \end{aligned} \tag{1.22}$$

the Kohn-Sham equation is

$$\hat{H}_{KS}\psi_i = \epsilon_i\psi_i. \tag{1.23}$$

Given an accurate $E_{XC}[n]$, the Kohn-Sham equations can be solved self-consistently for $\psi_i(\boldsymbol{r})$, V_H, V_{XC}, and $n(\boldsymbol{r})$, leading to the ground state density n_0 and energy $E[n_0]$ of our original interacting electron problem.

The simplest and most common approximation to $E_{XC}[n]$ is the local density approximation (LDA):

$$E_{XC}[n(\boldsymbol{r})] = \int n(\boldsymbol{r})\epsilon_{XC}(n(\boldsymbol{r}))d\boldsymbol{r}, \tag{1.24}$$

where $\epsilon_{XC}(n)$ is the exchange-correlation enegy per electron of the interacting homogeneous electron gas of density n. Accurate calculations of $\epsilon_{XC}(n)$ were performed by Ceperley and Alder [23]; a commonly used parametrization of these results for use in first-principles calculations is given in Ref. [24].

While the LDA can be expected to work well for systems close to the homogeneous electron gas, it also works surprisingly well for many non-homogeneous systems. The LDA is used in Chapters 5 and 6.

Generalized-gradient approximations (GGAs) can improve upon some deficiencies of the LDA, especially for surfaces and molecules [25]. In the GGA, $E_{XC}[n]$ is approximated as a semilocal functional of n:

$$E_{XC}[n(\boldsymbol{r})] = \int f(n(\boldsymbol{r}), \boldsymbol{\nabla} n(\boldsymbol{r}))d\boldsymbol{r}. \tag{1.25}$$

The GGA of Perdew, Burke, and Ernzerhof [26] is used for several calculations in Chapters 2–4 and 5.

While the Kohn-Sham energy eigenvalues have no rigorous meaning, they are often taken as an approximation for the electronic band structure or excitation spectrum of a system. As one-electron states, the Kohn-Sham orbitals can be used as a starting point for many-body perturbation approaches for calculating more accurate excitation energies, including, for example, the electron-phonon interaction, as discussed in Sec. 1.2.5.

Plane-waves and pseudopotentials

In the previous section, Kohn-Sham DFT was used to transform the electronic many-body problem, Eq. 1.3, into an independent-particle problem: the solution of the Kohn-Sham equations, Eq. 1.19.

In this thesis, we will use the plane-wave pseudopotential (PWPP) method [27–29] to solve the Kohn-Sham equations. A plane-wave basis is used to represent the wavefunctions ψ_i and density n, while the external potential $V_{\text{ext}}(\boldsymbol{r})$ is replaced by a sum of atomic pseudopotentials, simplifying the calculation.

Plane waves are a natural basis set for electrons in a periodic lattice. Even for systems that are not periodic in three dimensions, the PWPP method can be successfully applied by using the supercell approximation [30]. The fact that many metals are well-described by the nearly-free-electron approximation suggests that accurate calculations in some solids can be achieved with a reasonably sized plane-wave basis set. The pseudopotential makes possible accurate calculations non-nearly-free-electron systems as well [28].

Furthermore, fast-fourier-transform numerical methods allow for efficient transformation between real and reciprocal space, making the self-consistent solution of the potential, density, and wavefunctions computationally feasible. Details of the PWPP method and implementation can be found in reviews [27, 29].

We now review some of the theory of pseudopotentials, following loosely the discussion in Ref. [22]. The idea of the pseudopotential is to treat some electrons in our system as *core* electrons which are tightly bound to individual nuclei, while other electrons are treated as *valence* electrons which are more dispersed and may participate in bonding or are in some cases itinerant. Since we are working in an independent-electron approximation, we are free to partition the electron states into core and valence in this way. If we think of a molecule or solid as a collection of atoms, then the core electron wavefunctions hardly differ between an isolated atom and an atom surrounded by other atoms. By assuming the the core is "frozen," we can remove these electrons from our problem and simplify the calculations. However, when treating the valence electrons, the effect of the core electrons must still be considered. The pseudopotential for a given ion is the effective potential that the valence electrons feel due to the combination of the nucleus and the core electrons.

We can expect the pseudopotential of an ion to be softer (have smaller Fourier components at large wavevectors) and more repulsive than the full potential of the nucleus, $V(r) = -Z_I/r$. In the interstitial regions of many solids, the wavefunctions are smooth and nearly-free-electron-like. Also, since the valence wavefunctions must be orthogonal to the core electrons, the effective potential of the core electrons will work to push the valence wavefunctions away from the nucleus.

A precursor of the modern pseudopotential method is the orthogonalized plane-wave (OPW) method of Herring [31]. Phillips and Kleinman [32] and Antončik [33] took the OPW transformation and formulated it in terms of a psuedopotential. We briefly sketch their formulation here, using Dirac bra-ket notation. For simplicity, let us consider an isolated atom system within the Kohn-Sham independent-particle scheme. Let $|\psi\rangle$ be a valence eigenstate of H_{KS} with eigenvalue ϵ, so that by Eq. 1.19,

$$H_{\mathrm{KS}}|\psi\rangle = \epsilon|\psi\rangle. \tag{1.26}$$

Define a pseudoeigenstate by

$$\begin{aligned} |\psi\rangle &= |\psi_{\mathrm{ps}}\rangle + \sum_i a_i|\phi_i\rangle \\ a_i &= -\langle\phi_i|\psi_{\mathrm{ps}}\rangle, \end{aligned} \tag{1.27}$$

where $|\phi_i\rangle$ are core electron states with eigenvalues ϵ_i. Here $|\psi\rangle$ is explicitly orthogonal to the core states. Inserting Eq. 1.27 into Eq. 1.26, we find that $|\psi_{\mathrm{ps}}\rangle$ satisfies its own Schrödinger-like equation with eigenvalue ϵ,

$$(H + \hat{V}_r)|\psi_{\mathrm{ps}}\rangle = \epsilon|\psi_{\mathrm{ps}}\rangle, \tag{1.28}$$

where

$$\hat{V}_r = (\epsilon - \epsilon_i)\sum_i |\phi_i\rangle\langle\phi_i| \tag{1.29}$$

is a repulsive potential, since $\epsilon > \epsilon_i$. The repulsive potential is also nonlocal. The total pseudopotential is

$$\hat{V}_{\text{ps}} = \hat{V}_{\text{KS}} + \hat{V}_r. \tag{1.30}$$

Thus, if we replace the original potential by the pseudopotential (Eq. 1.30) and solve Eq. 1.28, we get the eigenvalues of the original Hamiltonian as well as the pseudoeigenfunctions, which can be used to reconstruct the original eigenfunctions if the core states $\{|\phi_i\rangle\}$ are known. Ideally the solution of the problem with the pseudopotential is easier than the original problem.

In general, the pseudopotential is not restricted to the form of Eqs. 1.29 and 1.30, and the flexibility can be used to generate pseudopotentials with desired characteristics. For example, one can try to generate pseudopotentials that are accurate, in the sense that the scattering properties or valence eigenvalues are given correctly. Two other desired characteristics of pseudopotentials are smoothness and transferability. A smoother pseudopotential requires fewer plane-waves to perform an accurate calculation. If a pseudopotential is transferable, it can be used in a variety of different systems with accurate results. This eliminates the need to generate a separate pseudopotential for each system studied.

We now discuss several classes of pseudopotentials. The pseudopotential of Eq. 1.30 is a total, screened pseudopotential, in the sense that the Hartree and exchange-correlation contributions of the valence electrons are included in the potential. If one subtracts the Hartree and exchange-correlation contributions of the valence electrons, one gets an unscreened, ionic pseudopotential. The screened pseudopotential can give accurate results because it includes the screening of the valence electrons for the particular system under consideration; however, it is less transferable than the ionic pseudopotential, with which the valence electrons screen according to each specific environment the psuedopotential is used in.

There are two approaches to generating pseudopotentials that give the correct properties. Empirical pseudopotentials try to fit properties to experimental data for an atom, molecule, or solid. *Ab initio* pseudopotentials do not use experimental input, but rather try to fit properties to all-electron calculations for single atoms with known atomic number.

In the empirical pseudopotential method, the total, screened pseudopotential is fit to experimental data, such as absorption spectra of semiconductors, and then used to reproduce the band structure throughout the Brillouin zone. This method has been shown to be very accurate [34, 35].

We will consider the case of an ionic pseudopotential that is transferable to different environments, such that a potential that is valid for an isolated atom will also be valid in a molecule or solid. Assuming spherical symmetry for an atomic pseudopotential, the general, semilocal form is

$$\hat{V}_{SL} = \sum_{lm} |Y_{lm}\rangle V_l(r) \langle Y_{lm}|, \tag{1.31}$$

where the Y_{lm} are spherical harmonics for angular momentum l and angular momentum z-component m.

In the present work, we use *ab initio* norm-conserving pseudopotentials (NCPP) and later variants, ultrasoft pseudopotentials and projector augmented-wave potentials.

The construction of NCPP involves the fitting of the pseudopotential to an all-electron calculation at a given reference electronic configuration by obeying the conditions laid out by Hamann, Schlüter, and Chiang (HSC) [36]:

1. the all-electron and pseudo valence eigenvalues agree;
2. beyond a chosen core radius r_c, the all-electron and pseudo wavefunctions are equal;
3. norm conservation: for each valence eigenstate, the integrals of the all-electron and pseudo charge density agree for $r > r_c$;
4. the logarithmic derivatives, and their first energy derivatives, of the all-electron and pseudo valence wavefunctions agree for $r > r_c$.

A pseudopotential obeying these conditions gives the correct scattering properties and the correct valence eigenvalues for the reference configuration, by construction.

The general procedure for constructing NCPPs involves the calculation of all-electron wavefunctions and eigenvalues at the reference configuration for each angular momentum channel l, the construction of pseudowavefunctions that satisfy the HSC conditions, the inversion of the radial Schrödinger equation to get the potentials from the pseudowavefunctions, and unscreening by removing the valence contributions to the Hartree and exchange-correlation potentials to get the final $V_l(r)$.

The freedom in choosing the form of the pseudowavefunctions for $r < r_c$, and the choice of the cutoff radius r_c, allow one to obtain pseudopotentials that balance needs for accuracy, softness, and transferability. HSC proposed their own form for the pseudowavefunctions. In the present work, the forms of Bachelet, Hamann, and Schlüter [37] (Chapter 6) and Troullier and Martins [38] (Chapter 3–5) are used. The method of Kleinman and Bylander [39] is used to transform the semilocal pseudopotential (Eq. 1.31) into a separable, nonlocal pseudopotential that is computationally efficient.

For certain atoms, such as alkali atoms, there is significant overlap of the core and valence charge densities. Because of the nonlinearity of the exchange-correlation potential with respect to density, the standard construction of NCPP can lead to errors. In the nonlinear core correction method [40], part of the core charge density is retained in the pseudopotential to more accurately calculate exchange-correlation effects.

In some cases, norm-conserving pseudopotentials are still hard and require a large plane-wave cutoff. Examples include p-states in C or O or d-states in first row transition metals, where there are no core states of the same angular momentum to orthogonalize to. In such cases, it is beneficial to use ultrasoft pseudopotentials [41]. With ultrasoft pseudopotentials, the norm-conservation condition is relaxed in order to obtain smoother pseudopotentials. The tradeoff is that the resulting pseudowavefunctions are not orthogonal, so that additional augmentation functions, localized in the core region, and an overlap operator must be included in the calculation. Overall, ultrasoft pseudopotentials make possible calculations that are computationally infeasible with NCPP. Ultrasoft pseudoptentials are used in Chapters 3 and 4 for certain species of atoms.

The projector augmented-wave (PAW) method [42, 43] can be viewed as a generalization of the ultrasoft pseudopotential method, with some advantages. Like ultrasoft pseudopotentials, PAW potentials allow one to solve for smooth psuedowavefunctions with a plane-wave basis set. However, the PAW method also retains the full all-electron wavefunctions for valence and core states, in a manner similar to, but more general than, linear augmented-plane-wave methods or linear muffin tin orbital methods [44]. In the PAW method, pairs of pseudo and all-electron partial waves, and corresponding projectors, are defined, all within a core region localized about an atom. The partial waves and projectors are similar to the augmentation functions and pseudopotential projectors in the ultrasoft method, but in the PAW method the full all-electron wavefunction can be reconstructed. Expectation values of physical operators are determined by evaluating the expectation value for the smooth pseudowavefunctions, retaining the computational advantages of the plane-wave basis, as well as one-center integrals evaluated on radial grids in the core region, which are also computationally efficient. Thus, with some additonal complexity, the PAW method provides additional physical information above the pseudopotential method. We use PAW potentials in Chapter 2.

Ionic forces

After an electronic structure calculation has been performed, the forces on the ions in the system can be computed. The input from the electronic structure calculation is the ground state electron density. The force on atom I is given by

$$\boldsymbol{F}_I = -\frac{\partial E(\{\boldsymbol{R}\})}{\partial \boldsymbol{R}_I}. \tag{1.32}$$

Within DFT, we have

$$-\frac{\partial E(\{\boldsymbol{R}\})[n]}{\partial \boldsymbol{R}_I} = -\int n(\boldsymbol{r})\frac{\partial V_{\text{ext}}(\boldsymbol{r})}{\partial \boldsymbol{R}_I}d\boldsymbol{r} - \frac{\partial E_{\text{ion-ion}}(\{\boldsymbol{R}\})}{\partial \boldsymbol{R}_I} - \int \frac{\partial E(\{\boldsymbol{R}\})}{\partial n(\boldsymbol{r})}\frac{\partial n(\boldsymbol{r})}{\partial \boldsymbol{R}_I}d\boldsymbol{r}. \tag{1.33}$$

The first two terms on the right side are due to the explicit derivative with respect to ionic position; the third term is implicit through the derivative with respect to the charge density. At the ground state, the third term is zero, because $\partial E/\partial n$ is constant, and the integral of $\partial n/\partial R_I$ over all space is zero due to charge conservation.

The relaxation of the ionic positions of a system to their equilibrium values proceeds as follows. An electronic structure calculation is performed for $\{\boldsymbol{R}\}$ fixed at guessed starting positions. From this calculation, forces are obtained, which are subsequently used to move the ions towards a better guess. Electronic structure and force calculations, and updates of ionic positions, are repeated until equilibrium positions are reached and the forces on the ions are below a threshold value. Expressions similar to those for the forces hold for the stress [22], which can be used to relax the unit cell parameters to equilibrium as well.

1.2.3 Phonons

We now turn to the solution of the hamiltonian describing the ionic motion, Eq. 1.4. For given $\{\boldsymbol{R}\}$, the term $E_n(\{\boldsymbol{R}\})$ can be determined by the methods of Sec. 1.2.2. Within the Born-Oppenheimer approximation, we assume that the state n represents the ground state at fixed $\{\boldsymbol{R}\}$, so we drop the subscript n. The solution of this hamiltonian, for ionic positions near their equilibrium values, gives the phonon frequencies and eigendisplacements of the system. The phonon frequencies are experimentally measurable quantities (as discussed in Chapters 5 and 6), and the phonon modes enter into the electron-phonon interaction (studied in Chapter 6). Our discussion follows Ref. [45].

For a solid or molecule in its equilibrium geometry, with ionic positions $\{\boldsymbol{R}_0\}$, the forces on the ions are zero. Let us define $E(\{\boldsymbol{u}\}) = E(\{\boldsymbol{R}\}) - E(\{\boldsymbol{R}_0\})$, with $\boldsymbol{u}_I = \boldsymbol{R}_I - \boldsymbol{R}_{I,0}$. In the harmonic approximation, which is valid for small $\{\boldsymbol{u}\}$, we can expand E to second order. The first order term is zero, and we have

$$E(\{\boldsymbol{u}\}) = \sum_{IJ\alpha\beta} C_{IJ}^{\alpha\beta} u_I^\alpha u_J^\beta, \tag{1.34}$$

where α, β index the Cartesian direction, I, J index the ion number, and $C_{IJ}^{\alpha\beta}$ are the interatomic force constants

$$C_{IJ}^{\alpha\beta} = \frac{\partial^2 E}{\partial R_I^\alpha R_J^\beta} = -\frac{\partial F_I^\alpha}{\partial R_J^\beta}. \tag{1.35}$$

The sums run over all the ions in the molecule or crystal.

For now, we treat the system classically; the main formulas carry over to the quantum case. The normal modes of the system are given by the eigenvectors U_I^α and eigenvalues ω^2 of the interatomic force constant matrix, from the equation

$$\sum_{J,\beta} (C_{IJ}^{\alpha\beta} - M_I \omega^2 \delta_{IJ} \delta_{\alpha\beta}) U_J^\beta = 0. \tag{1.36}$$

In an infinite periodic crystalline solid, we can write the atomic position vector as $\boldsymbol{R}_{I,0} = \boldsymbol{R}_l + \boldsymbol{\tau}_s$, where $\boldsymbol{R}_l$ is the position of the lth unit cell in the Bravais lattice, and $\boldsymbol{\tau}_s$ is the position of the atom in the unit cell. We also let $\boldsymbol{u}_s(l) = \boldsymbol{u}_I$, i.e., the displacement from equilibrium of the atom s in cell l.

With this notation, the interatomic force constants are

$$C_{st}^{\alpha\beta}(l,m) = \frac{\partial^2 E}{\partial u_s^\alpha(l) \partial u_t^\beta(m)} = C_{st}^{\alpha\beta}(\boldsymbol{R}_l - \boldsymbol{R}_m), \tag{1.37}$$

which depend on l and m only through the difference $\boldsymbol{R}_l - \boldsymbol{R}_m$. Then the interatomic force constants are $C_{st}^{\alpha\beta}(\boldsymbol{R}_l)$, defined relative to a reference cell with $m = 0$.

The dynamical matrix is the Fourier transform of the intearatomic force constants:

$$\tilde{C}_{st}^{\alpha\beta}(\boldsymbol{q}) = \sum_l e^{-i\boldsymbol{q}\cdot\boldsymbol{R}_l} C_{st}^{\alpha\beta}(\boldsymbol{R}_l), \tag{1.38}$$

where $\boldsymbol{q}$ is a wavevector in the first Brillouin zone. Then, for each wavevector $\boldsymbol{q}$, the normal mode frequencies $\omega(\boldsymbol{q})$ and diplacement patterns $U_s^\alpha(\boldsymbol{q})$ are the eigenvalues and eigenvectors of the dynamical matrix $\tilde{C}_{st}^{\alpha\beta}(\boldsymbol{q})$:

$$\sum_{t,\beta} (C_{st}^{\alpha\beta}(\boldsymbol{q}) - M_s \omega^2(\boldsymbol{q}) \delta_{st} \delta_{\alpha\beta}) U_t^\beta(\boldsymbol{q}) = 0. \tag{1.39}$$

The normal modes at different wavevectors are decoupled and behave as independent harmonic oscillators.

The dynamical matrix can also be written as a derivative with respect to lattice distortions of wavevector $\boldsymbol{q}$. Defining $\boldsymbol{u}_s(\boldsymbol{q})$ as the amplitude of the lattice distortion

$$\boldsymbol{u}_s(l) = \boldsymbol{u}_s(\boldsymbol{q}) e^{i\boldsymbol{q}\cdot\boldsymbol{R}_l}, \tag{1.40}$$

we have

$$\tilde{C}_{st}^{\alpha\beta}(\boldsymbol{q}) = \frac{1}{N_c} \frac{\partial^2 E}{\partial u_s^{*\alpha}(\boldsymbol{q}) \partial u_t^{\beta}(\boldsymbol{q})}. \tag{1.41}$$

From the quantum mechanical perspective, because the different normal modes are decoupled, we can solve each of them independently as is done for a simple harmonic oscillator. Then

$$\hat{H}_{\text{ion}} = \sum_{\boldsymbol{q}\nu} (n_{\boldsymbol{q}\nu} + \frac{1}{2}) \hbar\omega_{\boldsymbol{q}\nu}, \tag{1.42}$$

where

$$n_{\boldsymbol{q}\nu} = b_{\boldsymbol{q}\nu}^{\dagger} b_{\boldsymbol{q}\nu} \tag{1.43}$$

is the number operator giving the number of phonons in mode $\boldsymbol{q}\nu$, and $b_{\boldsymbol{q}\nu}^{\dagger}$ and $b_{\boldsymbol{q}\nu}$ are the phonon creation and annihilation operators.

To find the normal modes of a system, we need to calculate the interatomic force constants in real space or the dynamical matrix in wavevector space. The two main first-principles approaches to these calculations are the frozen phonon approach and density-functional perturbation theory.

Frozen phonons

In the frozen phonon approach, the interatomic force constants are calculated by displacing atoms a finite small distance away from their equilibrium positions and calculating the forces on the resulting atoms. For a displacement ΔR_J^{β} "frozen in" to the structure, the force on another atom (Eq. 1.32) can be computed as already described. Then the interatomic force constant (Eq. 1.35) is computed as

$$C_{IJ}^{\alpha\beta} = -\frac{\partial F_I^{\alpha}}{\partial R_J^{\beta}} \approx \frac{\Delta F_I^{\alpha}}{\Delta R_J^{\beta}}. \tag{1.44}$$

For each displacement, a separate self-consistent DFT calculation is required. An advantage of the frozen phonon approach is that no new methodology is required; the self-consisent Kohn-Sham DFT can be applied as before. A disadvantage of this approach is that for $\boldsymbol{q} \neq 0$, a supercell is required. For small $\boldsymbol{q} \neq 0$, the supercell is very large and computationally expensive. The frozen phonon approach has been shown to be very accurate in many system, such as semiconductors [46]. In Chapter 5, the frozen phonon method is used to calculate $\boldsymbol{q} = 0$ phonon modes in the material ZnCr_2O_4.

Density-functional perturbation theory

In the density-functional perturbation theory (DFPT) approach [45, 47–50], the derivatives of the energy E are calculated at the equilibrium positions of the ions, with no explicit displacement of the ionic positions. This method requires knowledge of the linear response of the density with respect to the perturbation. The discussion of DFPT here mainly follows Ref. [45].

In DFT, we can get the interatomic force constants (Eq. 1.35) by differentiating Eq. 1.33 with respect to ionic coordinates:

$$\frac{\partial^2 E(\{\boldsymbol{R}\})}{\partial \boldsymbol{R}_I \partial \boldsymbol{R}_J} = \int \frac{\partial n(\boldsymbol{r})}{\partial \boldsymbol{R}_J} \frac{\partial V_{\text{ext}}(\boldsymbol{r})}{\partial \boldsymbol{R}_I} d\boldsymbol{r} + \delta_{IJ} \int n(\boldsymbol{r}) \frac{\partial^2 V_{\text{ext}}(\boldsymbol{r})}{\partial \boldsymbol{R}_I \partial \boldsymbol{R}_J} d\boldsymbol{r} + \frac{\partial^2 E_{\text{ion-ion}}(\{\boldsymbol{R}\})}{\partial \boldsymbol{R}_I \partial \boldsymbol{R}_J}. \quad (1.45)$$

Only the first two terms on the right side of Eq. 1.45 depend on the electronic structure. The second term depends on the density $n(\boldsymbol{r})$, which is obtained from the original DFT calculation, and the first depends on the linear response $\partial n(\boldsymbol{r})/\partial \boldsymbol{R}_I$ of the density to a perturbation involving the movement of an ion.

To obtain this linear response, we first note that, taking the derivative of Eq. 1.15,

$$\frac{\partial n(\boldsymbol{r})}{\partial \boldsymbol{R}_I} = 2\text{Re} \sum_i \psi_i^*(\boldsymbol{r}) \frac{\partial \psi_i(\boldsymbol{r})}{\partial \boldsymbol{R}_I}, \quad (1.46)$$

recalling that the sum is over occupied states i. For a time-reversal invariant hamiltonian, we can drop the requirement to take the real part.

Taking the derivative of the Kohn-Sham equations (Eq. 1.19), with $\hat{H}_{\text{KS}}$ and V_{KS} defined as in (Eq. 1.22) we have

$$(H_{\text{KS}} - \epsilon_i) \frac{\partial \psi_i(\boldsymbol{r})}{\partial \boldsymbol{R}_I} = -\left(\frac{\partial V_{\text{KS}}(\boldsymbol{r})}{\partial \boldsymbol{R}_I} - \frac{\partial \epsilon_i}{\partial \boldsymbol{R}_I} \right) \psi_i(\boldsymbol{r}), \quad (1.47)$$

where

$$\frac{\partial V_{\text{KS}}(\boldsymbol{r})}{\partial \boldsymbol{R}_I} = \frac{\partial V_{\text{ext}}(\boldsymbol{r})}{\partial \boldsymbol{R}_I} + \int \frac{1}{|\boldsymbol{r} - \boldsymbol{r}'|} \frac{\partial n(\boldsymbol{r}')}{\partial \boldsymbol{R}_I} d\boldsymbol{r}' + \int \frac{\partial V_{XC}(\boldsymbol{r})}{\partial n(\boldsymbol{r}')} \frac{\partial n(\boldsymbol{r}')}{\partial \boldsymbol{R}_I} d\boldsymbol{r}' \quad (1.48)$$

and

$$\frac{\partial \epsilon_i}{\partial \boldsymbol{R}_I} = \langle \psi_i | \frac{\partial V_{\text{KS}}(\boldsymbol{r})}{\partial \boldsymbol{R}_I} | \psi_i \rangle. \quad (1.49)$$

Equations 1.46, 1.47, and 1.48 can be solved self-consistently for the density response $\partial n(\boldsymbol{r})/\partial \boldsymbol{R}_I$, wavefunction derivatives $\partial \psi_i(\boldsymbol{r})/\partial \boldsymbol{R}_I$, and potential response $\partial V_{\text{KS}}(\boldsymbol{r})/\partial \boldsymbol{R}_I$. The result allows us to compute the derivative in Eq. 1.45.

An alternate, equivalent form, combining these three equations into one large linear system, is the following:

$$(H_{\text{KS}} - \epsilon_i) \frac{\partial \psi_i(\boldsymbol{r})}{\partial \boldsymbol{R}_I} + \sum_j (K_{ij} \frac{\partial \psi_j}{\partial \boldsymbol{R}_I})(\boldsymbol{r}) = -\frac{\partial V_{\text{ext}}(\boldsymbol{r})}{\partial \boldsymbol{R}_I} \psi_i(\boldsymbol{r}), \quad (1.50)$$

with orthogonality constraints

$$\langle \psi_n | \frac{\partial \psi_j(\boldsymbol{r})}{\partial \boldsymbol{R}_I} \rangle = 0, \quad (1.51)$$

and with the operator K_{ij} defined as

$$(K_{ij}\frac{\partial\psi_j(\boldsymbol{r})}{\partial\boldsymbol{R}_I})(\boldsymbol{r}) = 2\int \psi_n(\boldsymbol{r})\left(\frac{1}{|\boldsymbol{r}-\boldsymbol{r}'|}+\frac{\partial V_{XC}(\boldsymbol{r})}{\partial n(\boldsymbol{r}')}\right)\psi_m^*(\boldsymbol{r}')\frac{\partial\psi_j(\boldsymbol{r}')}{\partial\boldsymbol{R}_I}d\boldsymbol{r}'. \tag{1.52}$$

For periodic crystals, we can compute the dynamical matrix in wavevector space instead of the interatomic force constants in real space. The equation in wavevector space corresponding to 1.45 is

$$\begin{aligned}\tilde{C}_{st}^{\alpha\beta}(\boldsymbol{q}) = \frac{1}{N_c}\Bigg[\int\left(\frac{\partial n(\boldsymbol{r})}{\partial u_s^\alpha(\boldsymbol{q})}\right)^*\frac{\partial V_{\text{ext}}(\boldsymbol{r})}{\partial u_t^\beta(\boldsymbol{q})}d\boldsymbol{r} + \delta_{st}\int n(\boldsymbol{r})\frac{\partial^2 V_{\text{ext}}(\boldsymbol{r})}{\partial u_s^{*\alpha}(\boldsymbol{q}=0)\partial u_t^\beta(\boldsymbol{q}=0)}d\boldsymbol{r}\\ +\frac{\partial^2 E_{\text{ion-ion}}(\{\boldsymbol{R}\})}{\partial u_s^{*\alpha}(\boldsymbol{q})\partial u_t^\beta(\boldsymbol{q})}\Bigg].\end{aligned} \tag{1.53}$$

Only the first two terms of the right hand side depend on the electronic structure. The first term requires the calculation of the density response due to the lattice distortion $\boldsymbol{u}_s(\boldsymbol{q})$ of wavevector $\boldsymbol{q}$. Because of the linearity of the DFPT equations (Eqs. 1.46, 1.47, and 1.48 or Eq. 1.50), this density response is also of wavevector $\boldsymbol{q}$. Thus in calculating the dynamical matrix, the $\boldsymbol{q}$-dependence factors out, and we need only compute functions in the original unit cell; no supercell is needed to compute the dynamical matrix at arbitrary wavevector $\boldsymbol{q}$ in the first Brillouin zone. The fact that no supercell is required is a significant advantage of the DFPT approach over the frozen phonon approach. To obtain a full phonon dispersion throughout the Brillouin zone, as is done in Chapter 6, one can calculate the dynamical matrix on a grid of $\boldsymbol{q}$-vectors using DFPT, Fourier transform to real space to obtain the real-space interatomic force constants, and then Fourier transform back to $\boldsymbol{q}$-space for a set of $\boldsymbol{q}$-points on an arbitrarily fine grid. The accuracy of this Fourier interpolation will depend on the extent of the force constants in real space in comparison to the fineness of the original $\boldsymbol{q}$-grid for which the dynamical matrices were calculated with DFPT.

1.2.4 Magnetism

Magnetism in a solid arises from the polarization of electron spin or orbital angular momentum. In this thesis, we are interested mostly in magnetic moments that are localized in space and are associated with a particular ion or atom, rather than spin polarization of itinerant electrons. These localized moments often retain atomic-like d character, such as in the transition metals. The interaction of these localized moments arranged in a regular crystal lattice can give rise to long-range ferromagnetic, antiferromagnetic, or more complex order. The interaction between local magnetic moments can be affected by their relative positions, giving rise to spin-phonon interactions (as in Chapter 5). Screening of local magnetic moments by itinerant electrons is also interesting and can lead to the Kondo effect [51].

An approach to studying magnetism from first-principles in a solid is to calculate the electronic structure, allowing for spin and orbital polarization, and to map the results to a simple model, such as a Heisenberg, Anderson [52], or Hubbard [53] model. With first-principles calculations, it is possible to associate local moment values to atoms by projecting the electronic states onto local orbitals, and to calculate parameters in the models, such as the exchange coupling constant J between neighboring local moments in the Heisenberg model. The projection onto local orbitals is not uniquely defined; one can choose to project onto harmonics within spheres of finite radii about certain atoms, or onto pseudoatomic orbitals, for example.

So far, in our discussion of DFT in Section 1.2.2, we assumed that that the densities for spin-up and spin-down electrons $n^{\uparrow}(\boldsymbol{r})$ and $n^{\downarrow}(\boldsymbol{r})$ were equal, and $n(\boldsymbol{r}) = n^{\uparrow}(\boldsymbol{r}) + n^{\downarrow}(\boldsymbol{r})$. We can allow the spin-up and spin-down densities to be different, so that spin-polarization is possible. The differences in densities for spin up and spin down are handled in the total energy functional, and in particular the exchange-correlation functional. In the local spin density approximation (LSDA) [21], the spin-polarized generalization of the LDA, we have

$$E_{XC}[n^{\uparrow}(\boldsymbol{r}), n^{\downarrow}(\boldsymbol{r})] = \int n(\boldsymbol{r})\epsilon_{XC}(n^{\uparrow}(\boldsymbol{r}), n^{\downarrow}(\boldsymbol{r}))d\boldsymbol{r}, \tag{1.54}$$

where $\epsilon_{XC}(n^{\uparrow}(\boldsymbol{r}), n^{\downarrow}(\boldsymbol{r}))$ is the exchange-correlation energy per electron of the interacting homogeneous electron gas for spin densities $n^{\uparrow}(\boldsymbol{r})$ and $n^{\downarrow}(\boldsymbol{r})$. A similar generalization is possible for spin-polarized GGA. Here the spins are assumed to be collinear (axis of quantization is the same for all points in space), but the generalization to noncollinear spins is possible.

In some magnetic systems, such as transition metal oxides or the cuprates, the LSDA ground state is far from the experimental one. For example, CoO and FeO are metallic in the LSDA but are insulators experimentally. In such systems with localized d electrons, correlation is important and is not treated correctly by the LSDA. One way of understanding this error is that in the LSDA, the localization of electrons is driven by exchange, with an energy scale of ~1 eV, while physically, in these strongly-correlated materials, localization is driven by an on-site coulomb interaction between electrons, with an energy scale of ~10 eV [54]. From another perspective, the LSDA suffers from self-interaction error [24, 55], in which the interaction of the electron with itself via the hartree term in the energy is not completely cancelled out by the exchange term. In addition, the LSDA does not allow for orbital polarization (except in the case of external effects such as crystal field splittings), instead tending to distribute electrons among the different orbitals equally [56].

Some of the problems of the LSDA can be corrected within a DFT framework by the LDA+U method [54, 57–59]. The LDA+U method is motivated by the Hubbard and Anderson models [52, 53], in which strongly-correlated electron systems are treated with tight-binding orbitals and a parameter U that characterizes the on-site coulomb interaction between two electrons. These localized electrons could be, for example, the d electron states from transition metal ions in a solid. For a localized (atomic-like) orbital, U can be defined as

$$U = E(n+1) + E(n-1) - 2E(n), \tag{1.55}$$

where $E(n_d)$ is the total energy of the system with a localized-orbital occupancy of n_d. For non-integer localized-orbital occupancies, as can happen in DFT, we can define U as

$$U = \frac{\delta^2 E_{\text{tot}}}{\delta n_d^2}. \tag{1.56}$$

In the LDA+U method, it is assumed that the total energy of a correlated system is well-described by the LSDA, but the orbital energies are not. As in the Anderson impurity model [52], electrons are separated into two subsystems: localized (usually d) electrons and delocalized (usually s and p) electrons. The localized states interact via the on-site Hubbard U coulomb energy, which is screened by the delocalized electrons. For the LDA+U method, the LDA energy functional is modified to include a Hubbard U term for the localized states; a double-counting term is also subtracted off because the LDA already includes on-site coulomb interactions in the total energy in an averaged way:

$$E_{\mathrm{LDA}+U} = E_{\mathrm{LDA}} + E_{\mathrm{Hub}} - E_{\mathrm{DC}}. \tag{1.57}$$

In a simple approximation neglecting exchange and nonsphericity and assuming a single atomic site, we have

$$\begin{aligned} E_{\mathrm{Hub}} &= \frac{1}{2}U\sum_{i\neq j} n_i n_j & (1.58)\\ E_{\mathrm{DC}} &= U\frac{N(N-1)}{2}, & (1.59)\end{aligned}$$

where n_i is the occupancy of the i-th localized state. Then the eigenvalues for the localized states are given by

$$\epsilon_i = \frac{\partial E_{\mathrm{LDA}+U}}{\partial n_i} = \epsilon_{\mathrm{LDA}} + U(\frac{1}{2} - n_i), \tag{1.60}$$

where ϵ_{LDA} is the LDA eigenvalue. Thus the U correction shifts the orbital energies by $-U/2$ and $+U/2$ for occupied and unoccupied orbitals, respectively, giving a gap of U. Shifting the orbital energies so that the gap is closer to the true gap for electronic excitations should improve the description of the ground state, even though we would not necessarily expect the orbital energies from DFT to be accurate.

More generally, we can write the LDA+U functional as

$$E_{\mathrm{LDA}+U}[n^{\sigma}(\boldsymbol{r}), \{n^{I\sigma}_{mm'}\}] = E_{\mathrm{LDA}}[n(\boldsymbol{r})] + E_{\mathrm{Hub}}[\{n^{I\sigma}_{mm'}\}] - E_{\mathrm{DC}}[\{n^{I\sigma}\}], \tag{1.61}$$

where $n^{I\sigma}_{mm'}$ is the occupation matrix for localized orbitals on atom I, and $n^{I\sigma} = \sum_m n^{I\sigma}_{mm}$. The index m labels the localized orbitals and usually corresponds to the magnetic quantum number. The occupation matrix will be defined shortly. In a fully rotationally invariant formulation, [56], including exchange, the Hubbard term is

$$\begin{aligned} E_{\mathrm{Hub}}[\{n^{I\sigma}_{mm'}\}] = \frac{1}{2}\sum_{\{m\},\sigma,I} &\{\langle m, m''|V_{ee}|m'm'''\rangle n^{I\sigma}_{mm'} n^{I,-\sigma}_{m''m'''} + \\ &(\langle m, m''|V_{ee}|m', m'''\rangle - \langle m, m''|V_{ee}|m''', m'\rangle) n^{I\sigma}_{mm'} n^{I\sigma}_{m''m'''}, \end{aligned} \tag{1.62}$$

with

$$\langle m, m''|V_{ee}|m'm'''\rangle = \sum_{k=0}^{2l} a_k(m, m', m'', m''')F^k, \tag{1.63}$$

where l is the angular momentum of the localized electrons,

$$a_k(m, m', m'', m''') = \frac{4\pi}{2k+1} \sum_{q=-k}^{k} \langle lm|Y_{kq}|lm'\rangle \langle lm''|Y_{kq}^{*}|lm'''\rangle, \tag{1.64}$$

and F^k are radial Slater integrals; $|lm\rangle$ and Y_{kq} are spherical harmonics. For d electrons, the F^k are expressed in terms of screened coulomb and exchange interactions U and J:

$$U = F^0, \tag{1.65}$$

$$J = \frac{F^2 + F^4}{14}, \tag{1.66}$$

and F^4/F^2 is set to a constant, its approximate value in atoms (≈ 0.625 for $3d$ elements). The expression for J for f electrons involves F^6. The U and J (equivalently the F^k) are treated as parameters in the theory.

The double-counting term is

$$E_{\mathrm{DC}}[\{n^{I\sigma}\}] = \sum_I \frac{U}{2} n^I (n^I - 1) - \sum_I \frac{J}{2} [n^{I\uparrow}(n^{I\uparrow} - 1) + n^{I\downarrow}(n^{I\downarrow} - 1)], \tag{1.67}$$

with $n^I = n^{I\uparrow} + n^{I\downarrow}$.

The definition of the occupation matrix is not unique. For our work, we define the occupation matrix in terms of a projection operator $P^I_{mm'}$ [55]:

$$n^{I\sigma}_{mm'} = \sum_{\boldsymbol{k},\nu} f^{\sigma}_{\boldsymbol{k}\nu} \langle \psi^{\sigma}_{\boldsymbol{k}\nu} | P^I_{mm'} | \psi^{\sigma}_{\boldsymbol{k}\nu} \rangle, \tag{1.68}$$

where $\psi^{\sigma}_{\boldsymbol{k}\nu}$ are the valence electronic wave functions of the system and $f^{\sigma}_{\boldsymbol{k}\nu}$ is the corresponding occupation number (ν is the band index). We define our projection operator to project states onto localized orbitals, and we choose atomic pseudowavefunctions ϕ^I_m for our localized orbitals:

$$P^I_{mm'} = |\phi^I_m\rangle\langle\phi^I_{m'}|. \tag{1.69}$$

For our work on $ZnCr_2O_4$ in Chapter 5, we make use of a plane-wave pseudopotential implementation of the rotationally invariant LDA+U method, as described in Ref. [60]. For treating correlations on transition metal adatoms on graphene in Chapters 3 and 4, we use a simplified rotationally invariant scheme [55].

There are several approaches to handling the U (or J) parameter in LDA+U calculations. For a fully first-principles calculation, U should also be calculated. Several methods for calculating U are given in the literature, [54, 55]. A more empirical approach can be taken, where U is chosen such that the calculated value of some physical quantity matches that of experiment; this is our approach in Chapter 5. In other cases, when a direct comparison with experiment is not possible, it is reasonable to explore a range of U values and check the dependence of the results on this parameter; this approach is followed in Chapters 3 and 4.

1.2.5 Electron-phonon interaction

Many-body formalism

So far, we have described methods of calculating the electronic structure of a condensed matter system for ions in fixed positions (Sec. 1.2.2) and the normal modes for the ionic motion of the system in the harmonic approximation (Sec. 1.2.3). The Kohn-Sham orbitals and eigenvalues from Sec. 1.2.2 are within the independent-electron approximation and are approximations to the excited states of the full system, described by the hamiltonian of Eq. 1.2. Likewise, the normal modes and frequencies from Sec. 1.2.3 are each independent of the excitations of other phonon modes.

However, many interesting physical phenomena involve the interaction of electrons with ionic motion. To describe this electron-phonon interaction, we will use the language of second quantization and the many-body formalism. In this section, we focus on periodic solids, and in particular metals.

Given single-electron energies and states $\epsilon_{n\boldsymbol{k}}, \psi_{n\boldsymbol{k}}$, and phonon frequencies and displacements $\omega_{\mathbf{q}\nu}, U_{\mathbf{q}\nu}$, we can write down the hamiltonian of the interacting electron-phonon system as

$$\begin{aligned} H &= \sum_{n\boldsymbol{k}} \epsilon_{n\boldsymbol{k}} c^\dagger_{n\boldsymbol{k}} c_{n\boldsymbol{k}} + \sum_{\mathbf{q}\nu} \omega_{\mathbf{q}\nu}(b^\dagger_{\mathbf{q}\nu} b_{\mathbf{q}\nu} + \frac{1}{2}) + \sum_{n,m,\boldsymbol{k},\boldsymbol{q},\nu} g^\nu_{mn}(\mathbf{k},\mathbf{q})(c^\dagger_{m,\boldsymbol{k}+\boldsymbol{q}} c_{n\boldsymbol{k}} b_{\mathbf{q}\nu} + \text{h.c.}) \\ &= H_e + H_p + H_{ep}, \end{aligned} \tag{1.70}$$

where $c^\dagger_{n\boldsymbol{k}}, c_{n\boldsymbol{k}}$ and $b^\dagger_{\mathbf{q}\nu}, b_{\mathbf{q}\nu}$ are creation and annihilation operators for electrons and phonons, respectively, and h.c. denotes hermitian conjugate. The electron-phonon matrix element is

$$g^\nu_{mn}(\mathbf{k},\mathbf{q}) = \left(\frac{\hbar}{2M\omega_{\mathbf{q}\nu}}\right)^{1/2} \langle m, \mathbf{k}+\mathbf{q}|\delta_{\mathbf{q}\nu} V_{SCF}|n,\mathbf{k}\rangle, \tag{1.71}$$

M is the ionic mass, and $\delta_{\mathbf{q}\nu} V_{SCF}$ is the derivative of the self-consistent potential (that the single-electron states experience) with respect to a collective ionic displacement corresponding to phonon wavevector $\mathbf{q}$ and mode ν. This hamiltonian is often referred to as the Frölich hamiltonian [61, 62]. The single particle electron states and phonon modes are obtained using the methods of Sections 1.2.2 and 1.2.3. Since, in the calculation of the phonon modes, the electrons are allowed to respond to the ionic motion, $\delta_{\mathbf{q}\nu} V_{SCF}$ is screened by the Coulomb interaction, and the phonon frequencies are screened by both the Coulomb and electron-phonon interactions.

We have neglected the hamiltonian for the electron-electron interaction; electron-electron effects enter into the electronic states in a mean-field way via the Hartree and exchange-correlation potentials, and through screening of the phonon frequencies and of $\delta_{\mathbf{q}\nu} V_{SCF}$, but are not treated fully. The electron-electron interaction in the context of superconductivity will be treated via the the coulomb pseudopotential μ^*.

Eventually, we will want to compute the superconducting properties of a solid. It turns out that, within the Nambu-Gorkov-Eliashberg theory [63–65] (or Eliashberg theory for short), we can determine the superconducting properties from the electron-phonon properties of the normal, non-superconducting state. Thus for now, we focus on the normal state.

For the normal state of a metallic solid, the Frölich hamiltonian can be solved using the Green's function formalism [66–69]. We let G and D denote the electron and phonon propagators. From Dyson's equation, we have

$$\begin{aligned} G(p) &= G_0(p) + G_0(p)\Sigma(p)G(p), & (1.72) \\ D(q) &= D_0(q) + D_0(q)\Pi(q)D(q); & (1.73) \end{aligned}$$

the subscript 0 denotes the bare propagator, $\Sigma(p)$ and $\Pi(q)$ are the (irreducible) electron and phonon self-energies, respectively, and p and q are the electron and phonon four-momenta, respectively. Many properties of interest can be determined from the self-energies.

For the normal state, Migdal [70] showed that with certain approximations, the self-energies are computed correctly to order $(m/M)^{1/2}$, with m and M being the electronic and ionic masses, even for strong coupling (large g). The approximations are the following: the vertex Γ can be replaced by the bare coupling g, the Feynman diagrams only up to first order are included, and G can be replaced by G_0.

In the Migdal approximation, following the rules for Feynman diagrams, the expression for the phonon self-energy is

$$\Pi_{\mathbf{q}\nu} = -2i \sum_{nm} \int \frac{dk}{(2\pi)^4} |g^{\nu}_{mn}(\mathbf{k}, \mathbf{q})|^2 G_0(k+q) G_0(k); \tag{1.74}$$

the factor of 2 is for spins, and k and q are four-momenta. The expression for the electron self-energy can be found similarly. The bare electron propagator is

$$G_0(\boldsymbol{k}, \omega) = \frac{1}{\omega - \epsilon_{n\boldsymbol{k}} + i\eta(\boldsymbol{k}, \omega)}. \tag{1.75}$$

Putting this expression in to 1.74, and focusing only on the imaginary part of the phonon self energy, we can integrate over energy to get

$$\Pi''_{\mathbf{q}\nu} = 2\pi \sum_{mn} \int_{BZ} \frac{d\boldsymbol{k}}{\Omega_{BZ}} |g_{mn,\nu}(\boldsymbol{k}, \boldsymbol{q})|^2 (f_{n\boldsymbol{k}} - f_{m\boldsymbol{k}+\boldsymbol{q}}) \delta(\omega_{\mathbf{q}\nu} + \epsilon_{n\boldsymbol{k}} - \epsilon_{m\boldsymbol{k}+\boldsymbol{q}}), \tag{1.76}$$

where $f_{n\boldsymbol{k}}$ is the Fermi-Dirac occupation function. In the "double-δ approximation", the term $f_{n\boldsymbol{k}} - f_{m\boldsymbol{k}+\boldsymbol{q}}$ is approximated by $\omega_{\mathbf{q}\nu}\delta(\epsilon_{m\boldsymbol{k}+\boldsymbol{q}} - \epsilon_F)$ and $\delta(\omega_{\mathbf{q}\nu} + \epsilon_{n\boldsymbol{k}} - \epsilon_{m\boldsymbol{k}+\boldsymbol{q}})$ by $\delta(\epsilon_{n\boldsymbol{k}} - \epsilon_F)$, were ϵ_F is the Fermi energy. Then Eq. 1.76 becomes

$$\Pi''_{\mathbf{q}\nu} = 2\pi\omega_{\mathbf{q}\nu} \sum_{mn} \int_{BZ} \frac{d\boldsymbol{k}}{\Omega_{BZ}} |g_{mn,\nu}(\boldsymbol{k}, \boldsymbol{q})|^2 \delta(\epsilon_{m\boldsymbol{k}+\boldsymbol{q}} - \epsilon_F) \delta(\epsilon_{n\boldsymbol{k}} - \epsilon_F); \tag{1.77}$$

The imaginary part of the phonon self-energy is the phonon linewidth $\Pi''_{\mathbf{q}\nu} = \gamma_{\mathbf{q}\nu}$, which is related to the lifetime of a phonon due to the electron-phonon interaction.

An important quantity in the theory of electron-phonon interactions and superconductivity is the Eliashberg spectral function $\alpha^2F(\omega)$, which gives the frequency spectrum of coupling of electronic states on the Fermi surface due to phonons. In terms of the phonon linewidths, $\alpha^2F(\omega)$ can be written as [71]

$$\alpha^2F(\omega) = \frac{1}{2\pi N(\epsilon_F)} \sum_{\nu} \int_{BZ} \frac{d\boldsymbol{q}}{\Omega_{BZ}} \frac{\gamma_{\mathbf{q}\nu}}{\omega_{\mathbf{q}\nu}} \delta(\omega - \omega_{\mathbf{q}\nu}), \tag{1.78}$$

where $N(\epsilon_F)$ is the density of states at the Fermi level per unit cell per spin.

The electron-phonon coupling constant λ is given by the integral

$$\lambda = 2\int_0^\infty \frac{\alpha^2 F(\omega)}{\omega} d\omega. \tag{1.79}$$

The constant λ is also called the mass enhancement parameter, as it characterizes the renormalization of the electronic mass for states at the Fermi level due to electron-phonon interactions:

$$m^* = (1+\lambda)m. \tag{1.80}$$

It also enters as a parameter into common formulas for the superconducting transition temperature T_c.

The main role of first-principles calculations in the theory of electron-phonon interactions is the computation of the electron-phonon matrix element $g^\nu_{mn}(\mathbf{k},\mathbf{q})$. If $g^\nu_{mn}(\mathbf{k},\mathbf{q})$ is computed from first principles, then the electron-phonon properties follow from the above described many-body Green's function machinery. The first-principles calculation of electronic states and phonon normal modes and frequencies is described in Sections 1.2.2 and 1.2.3. The variation in the self-consistent potential for the electrons due to a phonon perturbation, $\delta_{\mathbf{q}\nu} V_{SCF}$, is also obtained in a first-principles phonon calculation. Thus, all the ingredients for a first-principles calculation of $g^\nu_{mn}(\mathbf{k},\mathbf{q})$ are available. Further details of the calculations are given in Chapter 6.

Superconductivity

Superconductivity is perhaps the most interesting physical phenomenon arising from the electron-phonon interaction. Here we briefly review the Bardeen, Cooper, and Schrieffer (BCS) theory of superconductivity [11], and then touch upon Eliashberg theory [63–65], which is an extension of the BCS theory, and its relation to electron-phonon interactions in the normal state. The Eliashberg theory is the basis for our first-principles calculation of superconducting T_c.

The main idea of the BCS theory is that an attractive interaction between electrons leads a superconducting ground state in which electrons form Cooper pairs. The pairing and correlations between pairs explain the experimentally observed superconducting properties, including the energy gap for electronic excitations, zero resistance, the Meissner effect, and the discontinuity of the specific heat as a function of temperature.

Our discussion of BCS follows Ref. [66]. In BCS, it is assumed that the most important pairing is between states of opposite spin and momentum. The "reduced" hamiltonian describing this interaction is given by

$$H_{\text{red}} = \sum_{\boldsymbol{k}\sigma} \epsilon_{\boldsymbol{k}} n_{\boldsymbol{k}\sigma} + \sum_{\boldsymbol{k}\boldsymbol{k}'} V_{\boldsymbol{k}'\boldsymbol{k}} c^\dagger_{\boldsymbol{k}'\uparrow} c^\dagger_{-\boldsymbol{k}'\downarrow} c_{-\boldsymbol{k}\downarrow} c_{\boldsymbol{k}\uparrow}, \tag{1.81}$$

where $n_{\boldsymbol{k}\sigma} = c^\dagger_{\boldsymbol{k}\sigma} c_{\boldsymbol{k}\sigma}$, σ denotes the spin, and $V_{\boldsymbol{k}'\boldsymbol{k}}$ is the effective interaction between electrons. For simplicity we assume a single band.

Solving the reduced hamiltonian for the BCS ground state $|\psi_0\rangle$ (for temperature $T = 0$), one finds that the energy required to create a quasiparticle of momentum $\boldsymbol{k}$ in the superconducting state is

$$E_{\boldsymbol{k}} = (\epsilon_{\boldsymbol{k}}^2 + \Delta_{\boldsymbol{k}}^2)^{1/2}, \tag{1.82}$$

where the energy gap parameter $\Delta_{\boldsymbol{k}}$ satisfies an integral equation

$$\Delta_{\boldsymbol{k}} = -\sum_{\boldsymbol{k}'} V_{\boldsymbol{k}\boldsymbol{k}'} \frac{\Delta_{\boldsymbol{k}'}}{2E_{\boldsymbol{k}'}} \tag{1.83}$$

with the constraint that the expectation value of the number of electrons is fixed:

$$\langle\psi_0| \sum_{\boldsymbol{k}\sigma} n_{\boldsymbol{k}\sigma} |\psi_0\rangle = \sum_{\boldsymbol{k}} (1 - \frac{\epsilon_{\boldsymbol{k}}}{E_{\boldsymbol{k}}}) = N_0. \tag{1.84}$$

We can solve the gap equation if we approximate the interaction to be constant and attractive within a shell of width $2\omega_c$ about the Fermi surface:

$$V_{\boldsymbol{k}\boldsymbol{k}'} = \begin{cases} -V & \text{if } |\epsilon_{\boldsymbol{k}}| \text{ and } |\epsilon_{\boldsymbol{k}'}| < \omega_c \\ 0 & \text{otherwise.} \end{cases} \tag{1.85}$$

Then we get

$$\Delta_{\boldsymbol{k}} = \begin{cases} \Delta_0 & \text{if } |\epsilon_{\boldsymbol{k}}| < \omega_c \\ 0 & \text{otherwise,} \end{cases} \tag{1.86}$$

with

$$\Delta_0 \simeq 2\omega_c \exp\left[-\frac{1}{N(0)V}\right] \tag{1.87}$$

in the weak coupling limit, $N(0)V \lesssim 1/4$; $N(0)$ is the density of states at the Fermi level.

At finite temperature ($\beta = 1/k_B T$), the gap equation is

$$\Delta_{\boldsymbol{k}} = -\sum_{\boldsymbol{k}'} V_{\boldsymbol{k}'\boldsymbol{k}} \frac{\Delta_{\boldsymbol{k}}}{2E_{\boldsymbol{k}}} \tanh\frac{\beta E_{\boldsymbol{k}}}{2}. \tag{1.88}$$

Again using the approximation for $V_{\boldsymbol{k}\boldsymbol{k}'}$ of Eq. 1.85, we can solve for the gap and find that it decreases as T increases from 0. At the superconducting transition temperature T_c, the gap vanishes. In the weak coupling limit, we have for the superconducting transition temperature

$$T_c = 1.14\omega_c \exp\left[-\frac{1}{N(0)V}\right]. \tag{1.89}$$

Although the origin of the attractive interaction is not specified in the BCS theory, it is known from the isotope effect that the attraction in conventional superconductors comes from the electron-phonon interaction. Then the cutoff freqency for the interaction ω_c can be associated with some phonon frequency, such as the Debye frequency ω_D. From Eq. 1.89, we see that the main physical quantities determining T_c in the BCS theory are the strength of the interaction V, the density of states at the Fermi level $N(0)$, and the phonon frequency $\omega_c = \omega_D$.

In the Eliashberg theory, the BCS theory is extended to include retardation and damping effects. The hamiltonian is the same as in the normal state theory of Migdal (Eq. 1.70). However, in the superconducting state, the anomalous Green's functions, or off-diagonal elements of the Green's function matrix in Nambu-Gorkov formalism, are allowed to be nonzero. Solving for the self-energy using the first-order diagrams leads to the Eliashberg equations for the superconducting gap $\Delta(\boldsymbol{k}, \omega)$.

In many known superconductors, the gap is mostly isotropic, or independent of $\boldsymbol{k}$. In the isotropic approximation, McMillan [72] solved the Eliashberg equations numerically and fitted the results with a simple form for T_c, using only a few parameters. In the calculation of T_c in Chapter 6, we use the Allen-Dynes [73] form of the McMillan equation:

$$T_c = \frac{\omega_{\log}}{1.2} \exp\left(-\frac{1.04(1+\lambda)}{\lambda - \mu^*(1+0.62\lambda)}\right), \tag{1.90}$$

where μ^* is the Coulomb psuedopotential [74], which describes the repulsive electron-electron interaction, and $\omega_{\log}$ is the logarithmic average of the phonon frequencies (see Eq. 6.7). For weak coupling, this equation reduces to the BCS result (Eq. 1.89), where $N(0)V$ in BCS corresponds to $\lambda - \mu^*$ in the McMillan equation. In the McMillan equation, the important electron-phonon parameters are $\omega_{\log}$ and λ, which can be determined from the Eliashberg spectral function (Eq. 1.78). The Eliashberg spectral function incorporates information about the electron-phonon coupling strength, $N(0)$, and the phonon frequencies, the same physical quantities entering into the BCS result.

Chapter 2

First-principles study of metal adatom adsorption on graphene

In this chapter, the adsorption of 12 different metal adatoms on graphene is studied using first principles density functional theory with the generalized gradient approximation. The adsorption energy, geometry, density of states (DOS), dipole moment, and work function of each adatom-graphene system are calculated. For the adatoms studied from Groups I, II, and III of the periodic table, the results are consistent with ionic bonding, and the adsorption is characterized by minimal change in the graphene electronic states and large charge transfer. For transition, noble, and Group IV metals, the calculations are consistent with covalent bonding, and the adsorption is characterized by strong hybridization between adatom and graphene electronic states. For ionically bonded adatoms, the charge transfer is calculated quantitatively using two methods, one based on the DOS and the other based on the real space charge density. A variation in dipole moments and work function shifts across the different adatoms is observed. In particular, the work function shift shows a general correlation with the induced interfacial dipole of the adatom-graphene system and the ionization potential of the isolated atom. Work presented in this chapter has been published in Ref. [75].

2.1 Introduction

Graphene and carbon nanotubes (CNTs) are among the most prominent nanoscale materials currently studied. The confinement to one or two dimensions and the high symmetry of these materials lead to interesting new physics and many potential applications, especially involving the electronic structure and transport properties. One dimensional CNTs can be metallic or semiconducting, depending on chirality, and can act as quantum wires with minimal scattering [76]. Two dimensional graphene has a rather unique sublattice symmetry and is a zero-gap semiconductor with a point-like Fermi surface and a linear dispersion at the Fermi level. These properties are responsible for the observed ballistic transport, Dirac-like quasiparticles, and anomalous Quantum Hall effects in graphene [4].

Because of the diversity of properties of the metallic elements, the variety of structures formed, and the availablity of experimental techniques at the nanolevel, the adsorption of metals on the surfaces of these systems is a promising approach to controllably modify graphene and CNTs. Adsorption of alkali atoms has been used to chemically dope CNTs [77, 78] and fabricate field effect transistors [79]. Potassium has also been used to chemically dope graphene, allowing graphene quasiparticle dynamics [80] and minimum conductivity [81] to be studied. Furthermore, K atoms have also been used to tune the electronic structure of graphene bilayers [82].

Metals adsorbed on nanoscale carbon surfaces have been shown experimentally to form a variety of structures, such as continuous coatings or discrete clusters [83], and these structures can be manipulated to give rise to interesting new phenomena. For example, experiments have demonstrated the ability to control metal adatom diffusion between metal clusters on CNT surfaces [84]. Moreover, understanding the metallic structures that form and their interface with the carbon surface is essential to fabricating electronics devices for applications and transport experiments. Significant progress has been made in recent studies to understand such metal contacts to nanotubes and graphene [85, 86].

Much previous theoretical work on this subject has focused on the adsorption properties of one or a small set of metal adatoms on carbon nanostructures, particularly the structure, bonding, and charge transfer of 2D alkali adatom layers on graphite [87]. Other calculations surveyed of a range of adatoms on single-walled CNTs and reported on trends in binding energy and bond character, as well as the possibility of magnetic adatoms [88]. While there is a close relation between CNTs and graphene, the strong curvature of small-radius CNTs leads to rehybridization of the sp^2 C-C bond and can result in adsorption behavior that is different from graphene.

In this chapter, the adsorption of 12 different metal adatoms on graphene is studied using first-principles density-functional theory (DFT). Details of our method are described in Section 2.2. The adatoms chosen are often used in experiments and span a range of valences, including s and p valence metals, transition metals, and noble metals. The adsorption energy, geometry, density of states, dipole moment, work function, and magnetic moment are calculated. To augment previous work for alkalis on graphite [87] and other surfaces [89, 90], the issue of charge transfer is discussed, and for a subset of adatoms, charge transfer is determined quantitatively using two methods, one based on the density of states and the other based on the real space charge density. The large set of data resulting from this work is obtained with a uniform set of approximations, allowing for the direct comparison of values across the range of adatoms and the derivation of general adsorption trends.

Our results, described in Section 2.3, show that many adatoms bind to graphene with an adsorption energy of $\sim$ 1 eV. From the density of states, we determine that the adatoms considered in this work from Groups I, II, and III (I-III) of the Periodic Table bond ionically to graphene, transferring close to one electron to graphene without significantly modifying the graphene electronic states; other transition, noble, and Group IV metal adatoms modify the graphene states to a large degree, indicative of covalent bonding. Several adatoms induce a large dipole moment and work function shift relative to isolated graphene. We find a strong relation between the work function shift and the ionization potential of the isolated atom.

2.2 Methods

Our calculations are performed within first-principles DFT under the generalized gradient approximation (GGA) of Perdew, Burke, and Ernzerhof (PBE) [26], including spin polarization. The Vienna Ab-initio Simulation Package (VASP) is used to perform all calculations [91–93]. Ion cores are modeled with projector augmented wave (PAW) potentials [42, 43]. The semicore $1s$ states of Li, $2p$ states of Na, $3p$ states of K and Ca, and d states of Ga, In, Sn, Pd, and Au are treated explicitly as valence. A plane-wave basis set with a maximum plane-wave energy of 500 eV is used for the valence electrons wavefunctions. All parameters in the calculation are chosen to converge the total energy to 0.01 eV.

Graphene has two C atoms arranged in a two-dimensional honeycomb lattice with a hexagonal primitive unit cell. We use our calculated graphene lattice constant of 2.47 Å, which is slightly larger than the experimental value of 2.46 Å. For notation, we let the x and y directions be parallel and the z direction perpendicular to the graphene plane.

The adatom-graphene system is modeled using one metal adatom in a 4×4 hexagonal graphene supercell (Fig. 2.1; we refer to the metal adatom arrangement as a 4×4 layer). This setup corresponds to a coverage of 1 adatom per 32 C atoms. The in-plane lattice constant is 9.88 Å, which is also the distance between neighboring adatoms. We use a supercell length of 15 Å in the z direction.

The calculation using the 4×4 coverage approximates the interaction of an isolated adatom with graphene. Although the adatom-adatom interaction is not negligible, the distance between adatoms is large enough that the overlap of the electronic states of neighboring adatoms is small. For K, the total energy of a 4×4 metal layer of K in the absence of graphene differs from that of the isolated K atom (described below) by less than 0.01 eV. Potassium has the largest atomic radius of all adatoms considered (2.20 Å; Ref. [94]).

The adatom-graphene system lacks inversion symmetry and therefore has a net electric dipole moment perpendicular to the surface. To remove spurious dipole interactions between periodic images along the z direction, we self-consistently apply corrections to the local electrostatic potential and the total energy [95, 96]. These corrections are necessary in order to get the correct vacuum energy level, which we use to determine the work function. We find corrections to the total energy to be as large a 0.2 eV.

Calculations for the isolated 4×4 graphene, isolated 4×4 adatom layer, and 4×4 adatom-graphene system are performed with the same-sized hexagonal supercell. The Brillouin zone is sampled with a $9 \times 9 \times 1$ Γ-centered k-point grid, and Gaussian smearing with a width of $\sigma = 0.05$ eV is used for the occupation of the electronic levels. We consider the binding of the adatom on three sites of high symmetry: the hollow (H) site at the center of a hexagon, the bridge (B) site at the midpoint of a carbon-carbon bond, and the top (T) site directly above a carbon atom (Fig. 2.2). For each adsorption site for the adatom-graphene system, the adatom is relaxed along the z direction and the C ions in graphene in all directions until forces on the ions are less than 0.05 eV/Å. The supercell dimensions are kept fixed for all calculations.

To calculate adsorption energies, we also require the total energy of an isolated atom, which is approximated by the calculation with a single atom in a cubic supercell of length 14 Å. Only the Γ point of the Brillouin zone is sampled in this case.

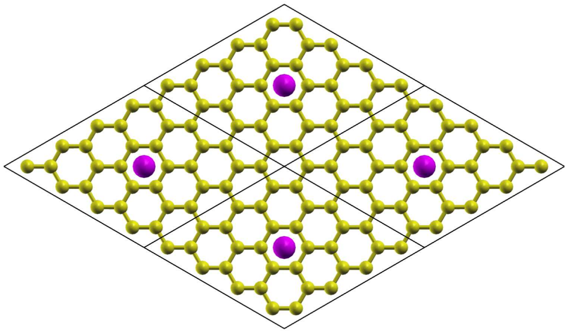

Figure 2.1: Adatom on the hollow site in a periodic 4×4 arrangement on a graphene surface.

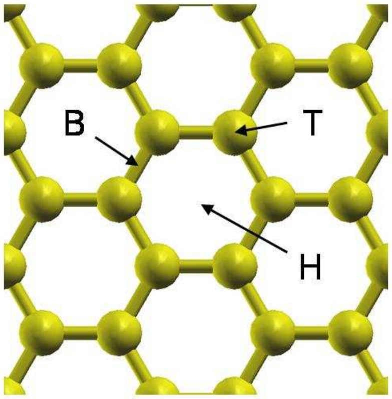

Figure 2.2: The three adsorption sites considered: hollow (H), bridge (B), and top (T).

2.3 Results

2.3.1 Adsorption energy and geometry

In this work, we define the adsorption energy as

$$\Delta E = E_{\mathrm{a}} + E_{\mathrm{g}} - E_{\mathrm{ag}}, \tag{2.1}$$

where E_{ag} is the total energy per adatom of the 4×4 adatom layer on graphene, E_{a} is the total energy of an isolated atom, and E_{g} is the total energy of the isolated graphene per 4×4 supercell (containing 32 C atoms).

The adsorption geometry is obtained from the positions of the atoms after relaxation. The adatom height (h) is defined as the difference in z coordinate of the adatom and the average of the z coordinates of the C atoms in the graphene layer. The distance (d_{AC}) between the adatom and its nearest carbon atom(s) is also calculated. In some cases, the distortion of the graphene layer is significant. We quantify the distortion by computing the maximum deviation in the z direction of the C atoms in the graphene layer from the average of their positions.

Of the three adsorption sites considered, the site with the largest adsorption energy (minimum total energy) is referred to as the favored site. We assume that the most likely diffusion pathway between favored sites is via the high-symmetry site with the next largest adsorption energy. The energy difference between these two sites is referred to as the diffusion barrier (E_{diff}). More accurate determination of the diffusion barrier would require calculating the complete potential energy surface or using, for example, the nudged elastic band method [97]. For all atoms which bind to the H or T sites (B site), the next largest adsorption energy is for the B site (T site).

Adsorption energies and structural properties for the three sites considered are summarized in Table 2.1. Metal adatoms from Groups I-III all bind most strongly to the H site. Within Group III, the adsorption energy decreases monotonically with increasing atomic number; however, this trend is not followed by the alkali metals. Our calculated adsorption site, adsorption energies, and heights are in reasonably good quantitative agreement with previous calculations for alkalis [99–102] and for In [103]. There is not complete agreement on the nature of the bonding of Al with graphite among previous experimental and theoretical works [104–108], but within our calculation, Al fits into the consistent picture that we find across the different elements.

For the alkalis, the relatively high ratios of adsorption energy to bulk cohesive energy suggest that alkalis are able to form 2D layers on the surface of graphene, as opposed to 3D clusters, in agreement with experiments observing 2D alkali layer formation on graphite [87]. On the other hand, the ratio $\Delta E/E_{\mathrm{c}}$ for Group III elements is lower than for the alkalis, which is reasonable given the experimentally observed island or 3D cluster formation for Al and In on nanotubes or graphite [83, 84, 104, 105].

The general consensus from both experiment and theory is that for dispersed alkali adatoms, the bonding to graphite is mainly ionic [87]. In Sec. 2.3.2, we provide evidence that Group I-III adatoms bond ionically to graphene. Our result indicating that these elements adsorb to the H site is consistent with previous work for alkalis on metal surfaces [90] which shows that for ionic bonding, sites of high coordination are favored.

Table 2.1: Energetic and structural properties for the hollow (H), bridge (B), and top (T) sites for the 12 adatoms considered in this work. The properties listed are the binding energy (ΔE), difference between binding energy and binding energy of lowest energy site ($E_{\mathrm{a}}^{\mathrm{max}} - \Delta E$), adatom height ($h$), adatom-carbon distance (d_{AC}), and graphene distortion (d_{GC}). For reference, we include the experimental cohesive energy per atom of the bulk metal (E_{c}) from Ref. [98] and the ratio of the adsorption energy to the bulk cohesive energy ($\Delta E/E_{\mathrm{c}}$).

Atom	Site	ΔE (eV)	E_{c} (eV)	$\Delta E/E_{\mathrm{c}}$	$E_{\mathrm{a}}^{\mathrm{max}} - \Delta E$ (eV)	h (Å)	d_{AC} (Å)	d_{GC} (10^{-1} Å)
Li	H	1.096	1.630	0.672		1.71	2.23	0.0
	B	0.773			0.322	1.88	2.09	0.2
	T	0.754			0.342	1.89	2.02	0.3
Na	H	0.462	1.113	0.415		2.28	2.70	0.1
	B	0.393			0.069	2.44	2.59	0.1
	T	0.389			0.074	2.49	2.54	0.1
K	H	0.802	0.934	0.859		2.60	2.99	0.1
	B	0.739			0.063	2.67	2.85	0.3
	T	0.733			0.069	2.67	2.77	0.2
Ca	H	0.632	1.840	0.343		2.29	2.72	0.1
	B	0.484			0.148	2.33	2.53	0.2
	T	0.478			0.154	2.34	2.46	0.2
Al	H	1.042	3.390	0.307		2.13	2.56	0.1
	B	0.927			0.115	2.22	2.33	0.1
	T	0.911			0.131	2.22	2.24	0.2
Ga	H	0.858	2.810	0.305		2.20	2.63	0.0
	B	0.762			0.096	2.30	2.41	0.0
	T	0.749			0.109	2.31	2.33	0.1
In	H	0.690	2.520	0.274		2.45	2.83	0.1
	B	0.622			0.069	2.53	2.63	0.0
	T	0.614			0.077	2.55	2.56	0.1
Sn	H	0.114			0.142	3.19	3.48	0.1
	B	0.253			0.003	2.79	2.81	0.8
	T	0.256	3.140	0.082		2.82	2.75	0.7
Ti	H	1.869	4.850	0.385		1.80	2.33	0.2
	B	1.301			0.568	2.05	2.27	0.3
	T	1.301			0.568	2.00	2.18	0.3
Fe	H	0.748	4.280	0.175		1.53	2.11	0.1
	B	0.231			0.517	2.22	2.35	0.0
	T	0.149			0.599	2.18	2.13	0.5
Pd	H	0.852			0.230	2.03	2.46	0.3
	B	1.081	3.890	0.278		2.21	2.18	1.4
	T	1.044			0.038	2.21	2.10	1.1
Au	H	0.085			0.011	3.53	3.80	0.0
	B	0.089			0.007	3.06	3.11	0.4
	T	0.096	3.810	0.025		2.69	2.55	1.4

For each element from Groups I-III, the adsorption energy and height for the B site is similar to the energy and height for the T site, while for the H site the adsorption energy is larger and the height is smaller. For an ionically-bonded adatom, the equilibrium height results from a balance of the electrostatic attraction between oppositely charged adatom and surface and the short range electron repulsion. Since the graphene electron density is lower at the H site than at the B or T sites, the adatom is stabilized closer to the surface. Thus ionic bonding appears to favor adsorption to the H site because, in addition to having a higher coordination as mentioned above, the adatom is also closer to the sheet, reducing the electrostatic energy (see also Ref. [109]).

The diffusion barriers via the B site for adatoms from Groups I-III are around 0.1 eV, with the exception of Li, which has a significantly smaller size than the other atoms. Within Group I or Group III, the trends in adsorption height or diffusion barrier are well correlated with atomic radius. For ionic bonding, as the adatom radius increases, its height increases, and the effect of the corrugation of the graphene is reduced. Elements from Groups I-III do not distort the graphene sheet by a significant amount, even on the B or T sites, where the distortion is greatest. Thus the C-C bonds near the adatom retain their sp^2 character and do not rehybridize significantly with any adatom orbitals. This result provides further support for the ionic bonding picture.

The $3d$ transition metal Ti has the largest adsorption energy of the adatoms considered, while Fe has a more modest adsorption energy. Like elements from Groups I-III, Ti and Fe favor the H site. However, the diffusion barriers are much larger than those for Groups I-III (about 0.5 eV). In addition, the H site adsorption height for Fe is small compared with the other adatoms studied. As discussed in subsequent sections, Ti and Fe bond covalently with graphene. Covalent bonds are directional, and the bond formation depends on the adatom coordination. Therefore it is reasonable that the adsorption energy is strongly dependent on the adsorption site. Our calculations for binding energy and geometry are in reasonable agreement with previous calculations for Ti and Fe on graphene [110–112]. In contrast to the strong binding we observe in our calculations, some experiments suggest that the Ti-graphene interaction is weak [113]. This difference may be due to a larger Ti surface density in experiment than in our calculations, which may reduce the Ti-surface interaction.

Though Pd has a filled d shell, it binds strongly to the B site of graphene, implying covalent bonding. The electronic structure presented in Section 2.3.2 shows that, like Ti and Fe, Pd adsorption involves hybridization of adatom d orbitals with the orbitals of graphene. However, the observation of d orbital hybridization alone is not enough to determine the favored adsorption site for a given adatom.

Although, like the alkalis, the Au atom has a single s valence electron, the Au adsorption energy is small. Sn adsorption is slightly stronger but is also weak relative to other adatoms. Adsorption of these elements to graphene likely involves van der Waals forces, which are not captured by DFT with the GGA. To the extent that our calculations accurately describe Au and Sn adsorption on graphene, the bonding is covalent; such bonding is consistent with adsorption to the T site, which allows for greater direct hybridization between the C atom and the adatom than adsorption to the H site.

In contrast to Group I-III elements, Pd, Au, and Sn adatoms all induce noticeable distortion ($\geq$ 0.07 Å) of the graphene sheet upon adsorption. The strong distortion likely changes some of the graphene sp^2-like orbital character to a more covalently reactive sp^3-like character. These three adatoms can diffuse readily along the hexagonal C bond network. For Au and Sn, the diffusion barrier is very small ($<$ 0.01 eV), and since the adsorption energies are small, the adsorption heights are correspondingly large. Our results for Au are in good agreement with previous calculations using the GGA [103, 114, 115]; previous calculations with the local density approximation (LDA) give somewhat larger adsorption energies [103, 116].

2.3.2 Electronic structure

In this section, we compute the electronic structure of the adatom-graphene system and identify general trends across the different adatoms considered. The Kohn-Sham density of states (DOS) is computed for each adatom on the favored adsorption site using a 24×24×1 Γ-centered Brillouin zone sampling, and the energy eigenvalues are smeared with Gaussians of width σ=0.1 eV. To generate the projected DOS (PDOS), the electron wavefunctions are projected onto spherical harmonics localized within a sphere centered about each atom. For the C atoms in graphene, the sphere radius is chosen to be 1.03 Å. For each adatom, the sphere radius is chosen to be the atomic radius, taken from Ref. [94].

We first consider alkali adsorption using K as an example. Of the metal adsorbates considered here, the alkalis are closest to ideal ionic bonding. Fig. 2.3 shows the DOS for K on the graphene H site and the DOS for isolated graphene, for both spin up and spin down. For each curve, the Dirac point of the graphene (where the DOS is zero) is clearly visible. In the plots, we shift the isolated graphene DOS to align its Dirac point with that of the K-graphene DOS. We denote the energy of the Dirac point by E_{D}. Near and below the Fermi level (E_{F}), the isolated graphene DOS closely matches that of the adatom-graphene system, except near clearly defined peaks at -17 eV and just above E_{F} (corresponding to $3p$ and $4s$ adatom states, respectively), showing that the graphene states are nearly unaltered by the adsorption of K adatoms.

Fig. 2.4 shows the same K-graphene DOS near the E_{F}, along with the projection of the DOS onto graphene and the K s state. The spin up $4s$ peak lies close to the Fermi level and is partially occupied, while the spin down $4s$ peak lies approximately 0.5 eV above E_{F} and is unoccupied. The position of these peaks above E_{F} are probably underestimated, since it is well known that GGA Kohn-Sham energy eigenvalues often differ from the true quasiparticle energies. There is no evidence for hybridization between the K $4s$ peaks and the graphene states; the PDOS of the graphene shows no peaks near the K $4s$ levels. Furthermore, the broadening of the K $4s$ peaks due to interaction with the graphene is small.

For K on graphene, the Fermi level is shifted higher in energy relative to E_{D}, reflecting a greater occupation of graphene states. Also, in an isolated atom, the spin up $4s$ peak is fully occupied, while in the adatom-graphene system the spin up $4s$ peak is only partially occupied. These observations suggest that the bonding is predominantly ionic and that close to one electron of charge (e) is transferred from the $4s$ state of the adatom to the graphene states.

Similar characteristics for the DOS are found for Na, including splitting of the $3s$

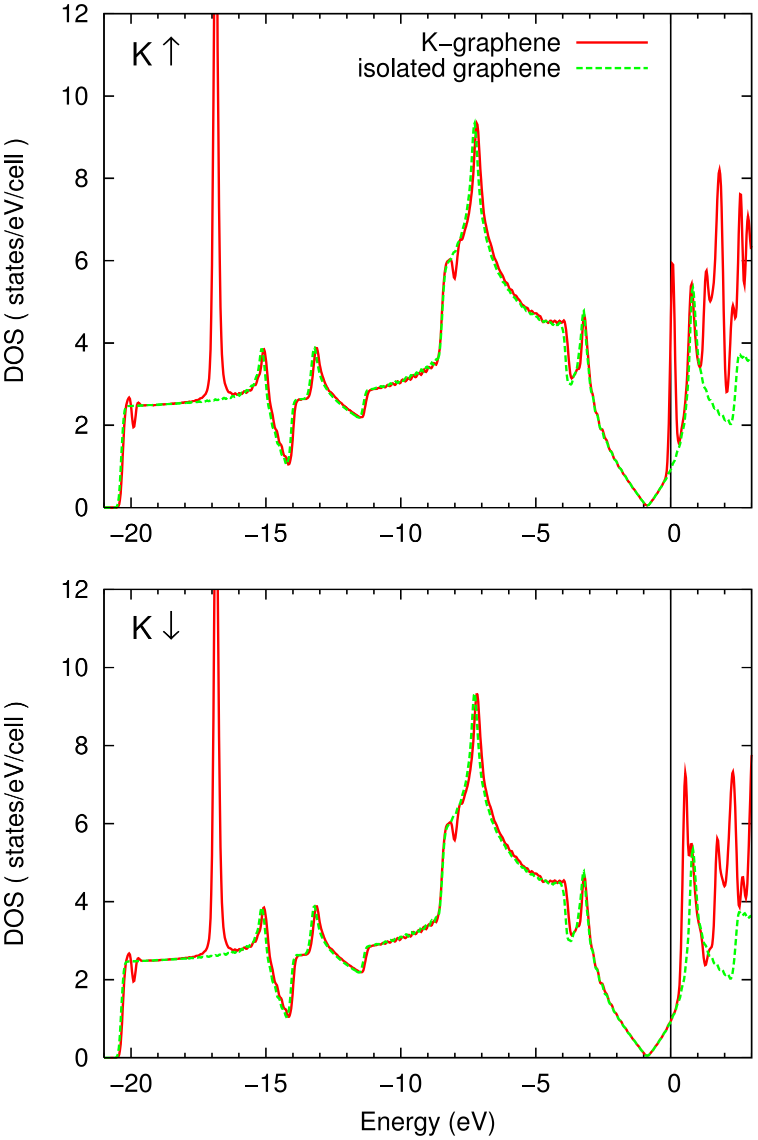

Figure 2.3: Spin up (top) and spin down (bottom) total DOS for K on the H site of graphene and for isolated graphene. The energy is relative to E_{F} of the K-graphene system. The curves are aligned at the Dirac point.

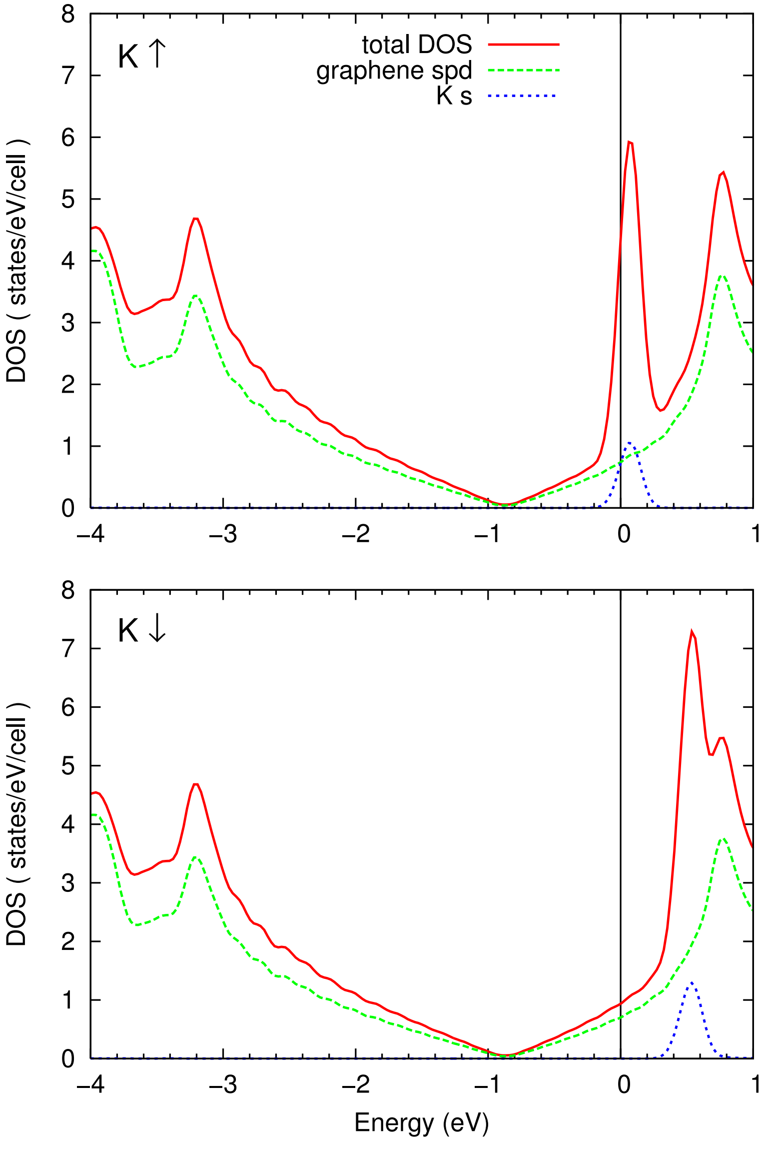

Figure 2.4: Spin up (top) and spin down (bottom) total DOS, PDOS on the graphene states, and PDOS on the K s states, for K on the H site of graphene. The energy is relative to E_{F}.

Table 2.2: Electronic properties for the favored adsorption site for the 12 adatoms considered in this work. The properties listed are the electric dipole moment per adatom (p), work function (Φ), magnetic moment per adatom of the adatom-graphene system (μ_{AG}), and magnetic moment of the isolated atom (μ_{A}). The calculated work function for isolated graphene is 4.26 eV. Also included is the experimental ionization potential of the isolated atom (IP) from Ref. [117]. The electric dipole moments are in units of debye (D), and the magnetic moments are given in Bohr magnetons (μ_B).

Atom	Site	p (D)	Φ (eV)	$\mu_{\mathrm{AG}}(\mu_B)$	$\mu_{\mathrm{A}}(\mu_B)$	IP (eV)
Li	H	3.46	1.94	0.00	1.00	5.39
Na	H	2.90	2.21	0.27	1.00	5.14
K	H	4.48	1.49	0.17	1.00	4.34
Ca	H	0.85	3.18	1.04	0.00	6.11
Al	H	0.93	3.08	0.00	1.00	5.99
Ga	H	1.83	2.66	0.00	1.00	6.00
In	H	2.57	2.34	0.00	1.00	5.79
Sn	T	0.19	3.81	1.81	2.00	7.34
Ti	H	1.39	3.16	3.41	4.00	6.83
Fe	H	1.84	3.24	2.03	4.00	7.90
Pd	B	1.23	3.61	0.00	0.00	8.34
Au	T	-1.29	4.88	0.96	1.00	9.23

valence spin up and spin down peaks, with partial occupation of the $3s$ spin up peak and an increase in E_{F} relative to E_{D}. For Li, the $2s$ spin up and spin down states are degenerate and lie about 0.9 eV above E_{F}, suggesting that more charge is transferred to graphene by Li than by Na or K. The degeneracy of the Li spin up and spin down $2s$ states and the splitting and partial occupancy of the Na $3s$ and K $4s$ states are in good agreement with previous theoretical calculations [99, 100]. The ionic bonding picture for the alkalis from the DOS agrees with our calculated energetic and structural properties and with the the consensus from previous experiment and theory [87].

The adsorption of Na or K adatoms on graphene leads to a net magnetic moment (Table 2.2) that is reduced from that of the isolated atom. This reduction results from partial charge transfer to the graphene, whose states are not spin polarized in the case of ionic bonding. One should exercise care in interpreting the magnetic moment results, which may be sensitive to adatom arrangement. The 4×4 adatom structure used for these calculations has not been observed experimentally; in addition, the GGA may not accurately describe the occupation of such localized adatom states.

In the case of Ca, the isolated atom has a filled $4s$ shell with two electrons. However, when Ca is adsorbed onto the graphene H site, its spin down $4s$ peak lies above E_{F} and is unoccupied, resulting in a magnetic moment of about 1 Bohr magneton (μ_B) per adatom. Experiments assessing the possibility of such a strong localized moment would be of interest. As with K, little hybridization of the $4s$ states with the graphene sheet is observed.

We now discuss the PDOS for Al on the H site (Fig. 2.5), which is respresentative of the Group III elements. These elements have two s valence electrons and one p valence

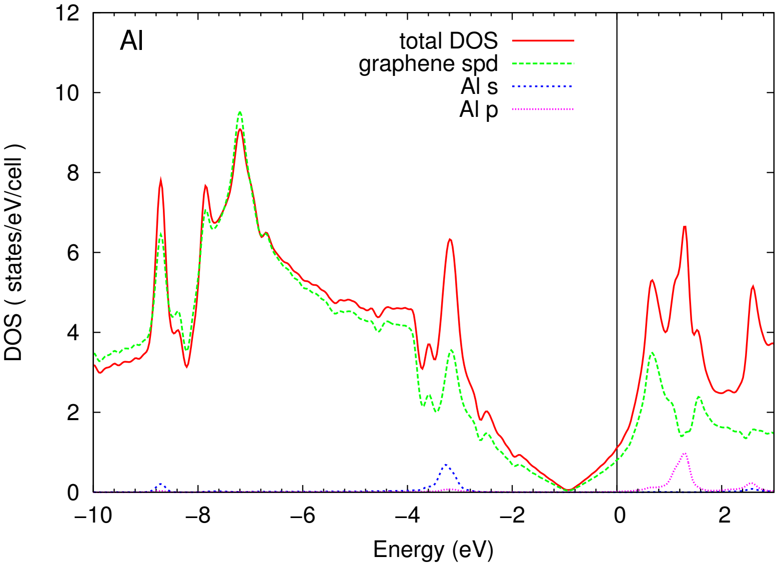

Figure 2.5: Spin up total DOS, PDOS on the graphene states, and PDOS on the Al s and p states, for Al on the H site of graphene. Spin up and spin down states are degenerate. The energy is relative to E_{F}.

electron in the outermost shell. Compared with the alkalis and Ca, Al adsorption affects the graphene electronic structure to a greater degree. The $3s$ state of Al appears to split and hybridize with the graphene states at -8.6 eV and -3.3 eV relative to E_{F}. The Al $3p$ peak lies 1.3 eV above E_{F} and is noticeably broadened due to the Al-graphene interaction. Nevertheless, the Dirac point is still clearly visible. Between E_{D} and E_{F}, the states are mostly from the graphene, and the DOS appears to be minimally altered from the isolated graphene case. Therefore, as for the alkalis, it is reasonable to characterize the bonding as ionic, involving charge transfer of nearly one electron per adatom to graphene. Although the interaction of the Al $3s$ state with graphene may contribute somewhat to the overall bonding, it may not be important for properties which depend mostly upon the states at E_{F}, such as transport.

For Al, Ga and In, the valence p peak remains above E_{F}, so that in all cases, close to one electron per adatom is transferred to graphene. Since there is little occupation of the valence p peak, the up and down spin states are degenerate, and there is no net magnetic moment for the Group III elements. Other features of the PDOS mentioned for Al are qualitatively the same for Ga and In. The ionic characteristics of the PDOS for Group III elements are consistent with the energetic and structural information discussed in Section 2.3.1. For In, the position of the $5p$ peak and the large charge transfer inferred from the PDOS are in good agreement with previous *ab initio* calculations [103].

Unlike the elements from Groups I-III, the transition metals Ti, Fe, and Pd significantly alter the graphene electronic structure. An important common feature in the DOS for these adatoms on graphene is the strong hybridization of the adatom d states with the graphene states to form covalent bonds. The PDOS for Ti on the H site of graphene is shown in Fig. 2.6. Strong hybridization of Ti $3d$ states and graphene states is evident from the prominent peaks in the PDOS. In the spin up PDOS, these hybrid Ti $3d$/graphene states lie in a broad range about E_{F}. Because the graphene states are strongly altered, the Dirac point is no longer evident. In the spin down PDOS, the Ti $3d$ states lie mostly above E_{F}. In this case, it appears that E_{D} lies below E_{F}, and one might infer electron transfer from Ti to graphene, though for covalent bonding, the concept of charge transfer is more ambiguous than for ionic bonding. Charge transfer does help to explain the reduction in magnetic moment from the isolated to the adsorbed atom (Table 2.2). Electrons which are spin-polarized in the isolated atom are transferred to less polarized graphene states when the atom is adsorbed on graphene.[1] The hybridization, charge transfer, and magnetic moment are in reasonable agreement with previous calculations [110].

As for Ti, the PDOS for Fe on the H site (Fig. 2.7) shows that there is covalent bonding and hybridization between $3d$ states and graphene states. The spin up $3d$ states of Fe are occupied and are split into two main peaks plus a broad band spanning several eV. The spin down $3d$ states of Fe also consist of two main peaks, one at E_{F}, as well as broad features. The spin up and spin down $4s$ states lie approximately 0.4 eV and 1.1 eV above E_{F}. The DOS illustrates that approximately two electrons are shifted from the $4s$ states in atomic Fe to the spin down $3d$ states in the Fe-graphene system. Consequently, the magnetic moment is reduced from 4 μ_B for the isolated Fe atom to 2.03 μ_B per adatom for Fe adsorbed on graphene. The hybridization of the spin down $3d$ states lowers their energy relative to the $4s$ states, explaining this transfer of electrons.

Since the graphene states are altered by Fe adsorption, the Dirac point can no longer be clearly identified. The DOS suggests that E_{F} does not shift much from E_{D}, indicating that little, if any, charge is transferred between the adatom and graphene. However, as for Ti, the applicability of the charge transfer concept is unclear.

Interestingly, although the Pd atom has a filled $4d$ shell, the $4d$ orbitals strongly hybridize with the graphene states when Pd is adsorbed on the B site (Fig. 2.8). These states lie below E_{F}, and there is no magnetic moment. The Pd $5s$ peak lies about 0.9 eV above E_{F}, and the Fermi level of graphene appears to remain at the Dirac point. In Pd and Fe, the bonding is almost completely covalent. For Au and Sn, near E_{F}, the $6s$ and $5p$ orbitals, respectively, hybridize with the graphene states. However, as noted above, the GGA may not be an accurate approximation for the bonding of these two elements to graphene.

2.3.3 Charge transfer

For adatoms from Groups I-III, the DOS provides evidence for ionic bonding and charge transfer between the adsorbate and substrate. Extracting a quantitative value for charge transfer from *ab initio* calculations is useful for comparing with both experiment and simple models. However, charge transfer is an ambiguous quantity and there is no unique definition. Some discussion of the concept of charge transfer in the context of adsorption to metal surfaces can be found in Ref. [89]. Charge transfer is most sensible in the context

---

[1] Note that the magnetic moment of the ground state for the isolated Ti atom given by the GGA differs from that in experiment.

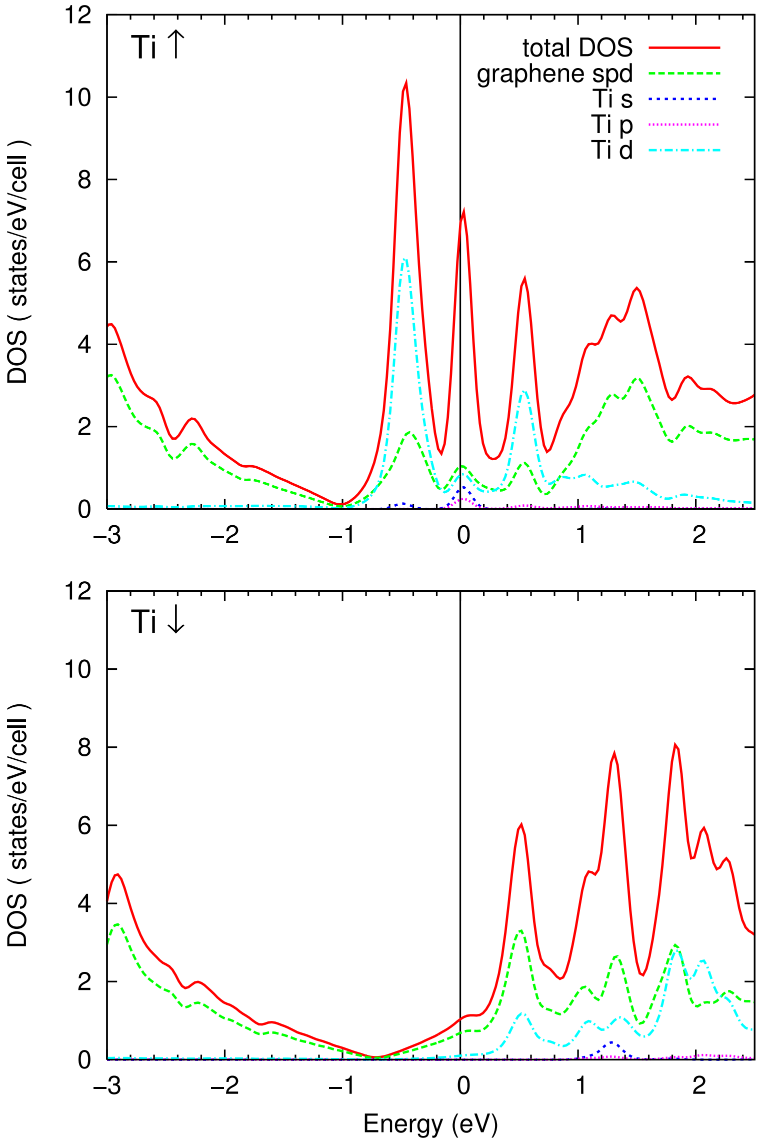

Figure 2.6: Spin up (top) and spin down (bottom) total DOS, PDOS on the graphene states, and PDOS on the Ti *s*, *p*, and *d* states, for Ti on the H site of graphene. The energy is relative to E_{F}.

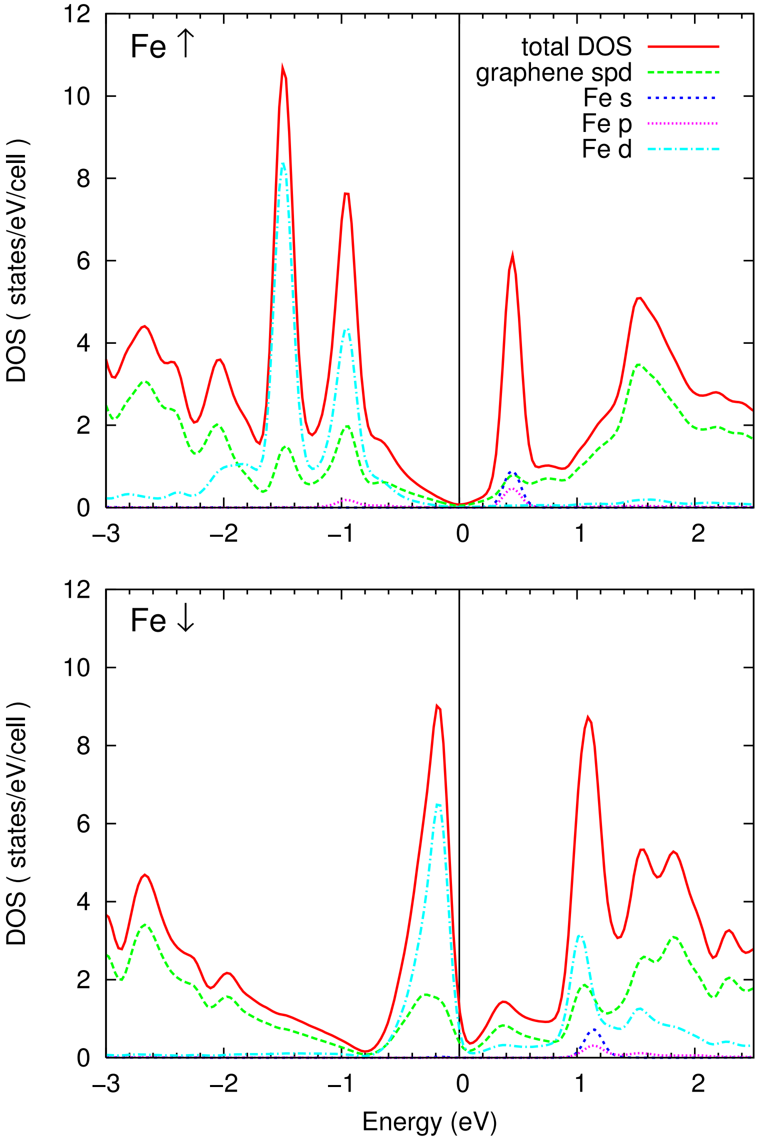

Figure 2.7: Spin up (top) and spin down (bottom) total DOS, PDOS on the graphene states, and PDOS on the Fe s, p, and d states, for Fe on the H site of graphene. The energy is relative to E_{F}.

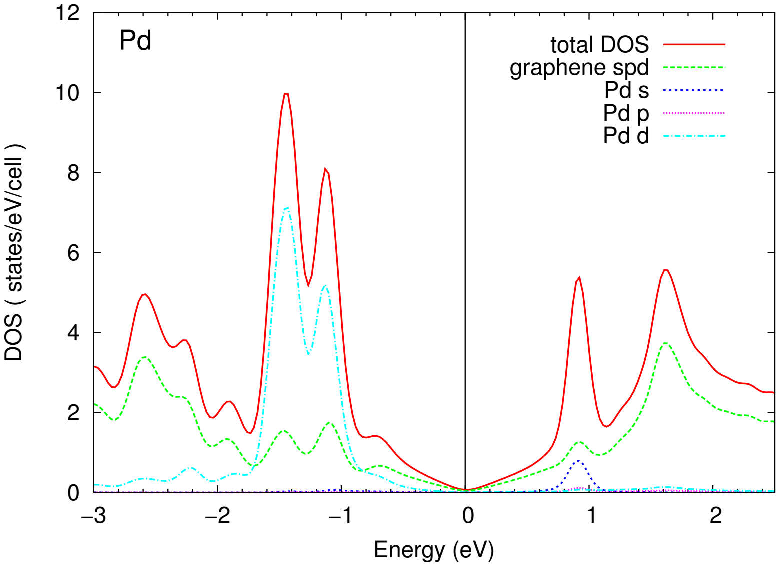

Figure 2.8: Spin up total DOS, PDOS on the graphene states, and PDOS on the Pd s, p, and d states, for Pd on the B site of graphene. Spin up and spin down states are degenerate. The energy is relative to E_F.

of ionic bonding. In the case of covalent bonding, charge is shared in the bond between adsorbate and substrate, and thus the charge transfer concept is less relevant.

For alkalis on graphite, various definitions of charge transfer are considered in several previous works [99,101,118–120]. In this work, we compare two definitions of charge transfer. One is based on the shift in E_F relative to the graphene DOS resulting from adatom adsorption. The other is based on integration of the charge density in real space. We apply these definitions to Group I-III adatoms. The other adatoms considered in this work bond with some degree of covalency to graphene and do not permit the same analysis.

Table 2.3: Fermi level shift relative to the graphene states (ΔE_F), charge transfer determined from the DOS (Δq_DOS), adsorbate-substrate cutoff distance (R_cut), and charge transfer from charge density integration (Δq_ρ), for adatoms from Groups I-III.

Atom	ΔE_F (eV)	Δq_DOS (e)	R_cut (Å)	Δq_ρ (e)
Li	0.95	0.90	1.64	0.39
Na	0.86	0.73	1.57	0.32
K	0.88	0.76	1.64	0.41
Ca	0.89	0.78	1.44	0.18
Al	0.94	0.88	1.37	0.14
Ga	0.94	0.88	1.44	0.21
In	0.92	0.84	1.51	0.27

Charge transfer from the DOS

The DOS of the adatom-graphene system can be used to determine the charge transfer, assuming that the graphene states remain unchanged due to adatom adsorption (aside from a rigid shift). As discussed in Section 2.3.2, this assumption is good for the alkalis and is reasonable for Groups II and III as well. For these systems, electrons are donated to the graphene, filling the rigid graphene states and thereby shifting the Fermi level up from the Dirac point. To calculate charge transfer from the adatom-graphene DOS, the Dirac point is identified, and the shift in Fermi level

$$\Delta E_{\mathrm{F}} = E_{\mathrm{F}} - E_{\mathrm{D}} \tag{2.2}$$

is determined. The charge transfer Δq_{DOS} is given by the integral of the isolated graphene DOS from E_{D} to $E_{\mathrm{D}}+\Delta E_{\mathrm{F}}$. The Fermi level shift ΔE_{F} and charge transfer Δq_{DOS} are given in Table 2.3 for each of the elements in Groups I-III considered in this work. A positive charge transfer indicates transfer of electrons from the adatom to graphene.

It is interesting that $\Delta E_{\mathrm{F}} \approx 0.9$ eV for all Group I-III elements we considered (although a small difference in ΔE_{F} can give a significant difference in Δq_{DOS}). The largest charge transfer is for Li, but Na, K, and Ca all transfer less charge than the Group III elements.

Similar methods have been used previously to estimate charge transfer for K on graphite at a low coverage, using Fermi level shifts determined from experiments. Charge transfer has been estimated to be around 0.7 e from electron energy loss spectroscopy [121] at a coverage of less than 0.1 monolayer (ML). For K, a coverage of 1 ML corresponds to a 2×2 hexagonal adsorbate structure. This value is in reasonable agreement with our results, although our coverage is at least 2.5 times greater than that in experiment. Using a Fermi level shift determined from photoemission, the charge transfer has been estimated to be around 0.1 e [122,123], significantly less than our and most other previous results for charge transfer [87]. Issues related to adatom coverage are discussed further in Section 2.3.4.

Charge transfer from the charge density

Partitioning the charge density in real space can be used to define charge transfer as well. (In what follows, the charge density refers to the valence electron charge density.) First, we define the charge density difference as

$$\Delta\rho(\mathbf{r}) = \rho_{\mathrm{ag}}(\mathbf{r}) - \rho_{\mathrm{a}}^{\mathrm{layer}}(\mathbf{r}) - \rho_{\mathrm{g}}^{\mathrm{relaxed}}(\mathbf{r}). \tag{2.3}$$

For all quantities in Eq. 2.3, the charge density is computed in the same hexagonal supercell. The quantity ρ_{ag} is the charge density of the adatom-graphene system. The charge density of the 4×4 adatom layer without graphene, $\rho_{\mathrm{a}}^{\mathrm{layer}}$, is calculated with the adatom in the same position in the supercell as for the adatom-graphene calculation. The quantity $\rho_{\mathrm{g}}^{\mathrm{relaxed}}$ is the charge density of an isolated 4×4 graphene layer, computed with the atoms fixed to their relaxed coordinates from the adatom-graphene calculations; these coordinates differ from those of isolated graphene. The charge density difference quantifies the redistribution of electron charge due to the adatom-graphene interaction.

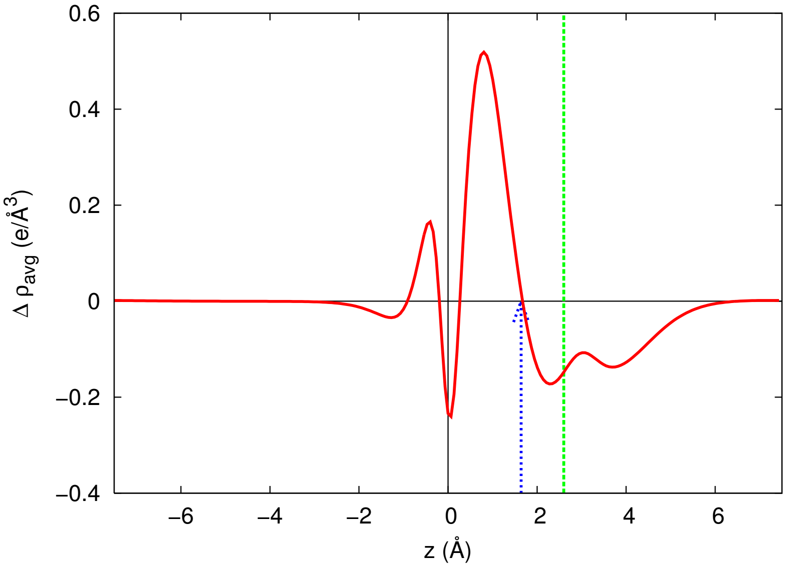

Figure 2.9: The x-y planar averaged electron charge density difference ($\Delta\rho_{\text{avg}}$) for K on graphene H site, as a function of position in the z direction. Two vertical lines indicate the position of the graphene sheet (0 Å) and the position of the adatom (2.60 Å). The arrow at 1.64 Å indicates R_{cut} used in calculating Δq_{ρ}.

As an example, Fig. 2.9 shows the x-y planar averaged charge density difference ($\Delta\rho_{\text{avg}}$) as a function of z for K on the H site. The position of the graphene sheet at $z = 0$ Å and the position of the adatom at $z = 2.60$ Å are indicated by vertical lines. The plot illustrates electron transfer from the adatom to the graphene with a large overall electron density increase near the graphene sheet and an electron density decrease near the adatom.

To determine the charge transfer using the spatial charge density, the regions of space belonging to the graphene or the adatom must be specified, introducing a degree of arbitrariness to the definition. For the purpose of comparison, we adopt the definition used in several previous works [99, 101, 118–120]. An adsorbate-substrate cutoff distance R_{cut} is defined as the distance from the graphene plane to the point between the plane and the adatom at which charge accumulation changes to charge depletion, for electron transfer from the adatom to the graphene (or vice versa, for opposite electron transfer). For example, in Fig. 2.9, the region with $z < R_{\text{cut}}$ is assigned to the substrate, and the region with $z > R_{\text{cut}}$ is assigned to the adatom. The charge transfer Δq_{ρ} is given by the integral of the charge density difference in the substrate region. The results for R_{cut} and Δq_{ρ} are given in Table 2.3 for adatoms from Groups I-III.

For the alkalis, R_{cut}, Δq_{ρ}, and plots of the planar-averaged charge density difference are consistent with previous calculations [101], with small differences likely coming from the different number of graphene layers used. Within Group I or Group III, the values for R_{cut} and Δq_{ρ} are similar. The alkalis have greater charge transfer than the other elements. For Group III, R_{cut} and Δq_{ρ} increase monotonically with atomic number. The cutoff distance R_{cut} is nearly the same for all the alkalis (as noted in Ref. [101]), but is different from

R_{cut} for the Group III elements. That the effective "thickness" of the graphene depends on the adsorbate is an indication of the arbitrariness of the charge transfer definition.

Comparison of charge transfer definitions

The charge transfer values differ significantly depending on the definition, with $\Delta q_{\mathrm{DOS}} > \Delta q_\rho$ for a given element. Also, Δq_{DOS} is larger for the Group III elements than for the alkalis (aside from Li), while the reverse is true for Δq_ρ. It is not surprising that the two definitions give different values, since the charge density associated with an electronic state with a defined energy can be spatially extended. Both definitions have reasonably simple pictures; which one is more meaningful depends on the physical properties of interest. Examining the DOS would be more useful if one were interested in the carrier concentration of graphene, while the charge density definition might be more suited for simple electrostatic models of the adatom-graphene interaction or for interpreting core level shift measurements.

2.3.4 Dipole moment and work function

The electric dipole moment perpendicular to the graphene sheet is an alternative to charge transfer for quantitatively describing the real space charge rearrangement due to adatom-graphene interaction. For ionically bonded adatoms, the dipole moment has a large contribution from charge transfer between adatom and substrate, but rearrangement of charge in covalent bonds and polarization of semicore states localized on the adatom also play a role. These contributions could also apply to covalently bonded adatoms.

Unlike charge transfer, the dipole moment is well-defined for both ionic and covalent cases considered here. We compute the dipole moment p in the z direction for the unit cell of the adatom-graphene system as

$$p = -\int \rho(z) z dz + \sum_i Z_i e z_i, \tag{2.4}$$

where $\rho(z)$ is the valence electron density integrated over the x-y plane [$\rho(z) \geq 0$ by definition], i indexes the ion, Z_i is the net atomic number of ion i, e is the electronic charge ($e > 0$), and z_i is the z coordinate of ion i. The sum and integral are over the unit cell. Since there is one adatom per unit cell, p gives the dipole moment per adatom.

In general, adatom adsorption on graphene is expected to alter the Fermi level and dipole moment of the system, and there can be a large change in work function relative to isolated graphene. We define the work function as

$$\Phi = E_{\mathrm{vac}} - E_{\mathrm{F}}, \tag{2.5}$$

where E_{vac} is the reference vacuum energy. In our calculation, E_{vac} is determined from the electrostatic potential in the vacuum region, far enough away from the adatom-graphene system in the z direction that the value is converged. Because the adsorption is only one side of the graphene sheet, the vacuum energies on the two sides of the graphene sheet differ, with the potential difference proportional to the dipole moment (to leading order in multipoles) via

$$\Delta V = -4\pi e n_a p, \tag{2.6}$$

where n_a is the number of adatoms per unit area on the graphene surface ($n_a = 1.18 \times 10^{14}$ adatoms/cm^2 for our 4×4 supercell). We use the term "dipole potential" to refer to this potential difference ΔV. In calculating the work function, E_{vac} is defined as the vacuum energy on the side of graphene that the adatoms are adsorbed to. The work function of isolated graphene is calculated to be 4.26 eV, an underestimate of the experimental value for graphite (about 4.6 eV) [124], but consistent with other DFT calculations using the PBE functional [125]. This $\sim 10\%$ underestimation is not expected to qualitatively affect the broad trends described below.

The calculated dipole moment per adatom and work function for each adatom are listed in Table 2.2. Of the adatoms considered, the alkalis generate the largest dipole moments and the largest decreases in work function. Other adatoms with ionic character (Groups II-III) and even the covalently bonded adatoms also decrease the work function of graphene noticeably. In contrast, Au adatoms increase the work function of graphene.

Fig. 2.10 shows a plot of the work function shift ($\Delta\Phi$) relative to isolated graphene versus the dipole moment for the 4×4 adatom arrangement considered here. Remarkably, the adatoms from Groups I-III lie on a straight line given by the sum of the dipole potential (Eq. 2.6) and an offset energy (E_{off}):

$$\Delta\Phi = -4\pi e n_a p - E_{\mathrm{off}}. \tag{2.7}$$

Fitting this equation to the data for Groups I-III gives $E_{\mathrm{off}} = 0.74$ eV. The observed linear relationship is consistent with the ionic bonding picture obtained from other data presented in this work. In particular, the fitted value for E_{off} is close to ΔE_{F} for these adatoms, which is about 0.9 eV (Table 2.3). Eq. 2.7 indicates that two dominant contributions to $\Delta\Phi$ for ionically bonded adatoms are (i) the dipole potential, which shifts the graphene states rigidly with respect to the vacuum, and (ii) the filling of graphene states due to electron transfer from the adatom, resulting in a shift of the Fermi level relative to the graphene states.

For alkali adatoms on bulk metal surfaces, previous work has shown that to first approximation the work function shift is simply given by the dipole potential, $\Delta\Phi = -4\pi e n_a p$ [126]. For a bulk metal surface, any charge transfer between adatom and substrate changes E_{F} by an infinitesimal amount, so there is a negligible Fermi level shift relative to the metal electronic states. On the other hand, since graphene is 2D and has a small DOS near E_{F}, charge transfer from adatom adsorption does result in a finite band filling term that contributes significantly to $\Delta\Phi$. Thus the ionic bonding picture for adsorption on graphene is consistent with that for adsorption on metals.

In Fig. 2.10, the data for adatoms not in Groups I-III lie above the plotted line and are not collinear, possibly indicating that these adatoms each have different band filling terms that are smaller than 0.74 eV, which implies smaller charge transfer than for adatoms from Groups I-III. It is also possible that, for these adatoms, $\Delta\Phi$ is not simply described as the sum of a dipole potential term and a band filling term. These observations are consistent with evidence from the binding energy, geometry, and DOS that their bonding is more covalent and less ionic in character.

Fig. 2.11 shows that $\Delta\Phi$ is well correlated with the experimental ionization potential (IP) of the isolated atom [117]. We fit the values of $\Delta\Phi$ and IP for the 12 species to

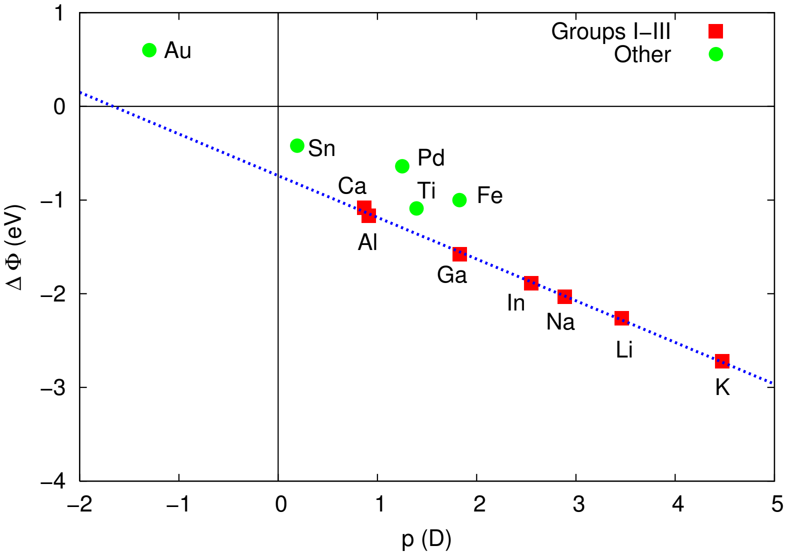

Figure 2.10: Plot of the work function shift ($\Delta\Phi$) relative to isolated graphene versus dipole moment (p) for the 4×4 adatom coverage. Red squares are elements from Groups I-III; other elements are marked by green circles. The dotted blue line is given by Eq. 2.7.

a line and obtain the following relation for the 4×4 coverage:

$$\Delta\Phi = 0.58 \text{ IP} - 5.09 \text{ eV}, \tag{2.8}$$

where $\Delta\Phi$ and IP are in units of eV. The overall trend of larger decreases in Φ for smaller IP values is reasonable, since Φ (IP) is the energy to remove an electron from the adatom-graphene system (isolated atom). Within the ionic picture of bonding, adatom species with lower IPs are more likely to transfer their outer shell electrons to the graphene sheet, thereby both creating a larger dipole layer and raising E_F relative to vacuum to a greater degree. However, it is interesting to note that adatoms with covalent character also follow the general trend relating $\Delta\Phi$ and IP.

We now remark on the possible coverage dependence of our results. Decreasing the coverage would decrease n_a and E_off in Eq. 2.7, but we would not expect p to change significantly. Therefore we would expect the line in Fig. 2.10 to shift up and its slope to decrease in magnitude. Going to a high coverage would increase n_a but would also affect p and E_off due to increased adatom-adatom interaction, and a linear relation between $\Delta\Phi$ and p might no longer hold. In Fig. 2.11, we would also expect the slope to change monotonically with the coverage if adatom-adatom interactions are small, but the linear relation between $\Delta\Phi$ and the IP also might not hold at high coverages.

The adatom coverage (θ) and arrangement are important to consider when comparing our results to experiment. Previous experiments measuring $\Delta\Phi$ for adatoms on graphite focus mainly on K. Experimentally, K is observed to form a dispersed phase at low coverages on graphite, with a large adatom-adatom spacing. As the coverage is increased, the K-K spacing decreases until a critical coverage θ_c is reached. Above θ_c, hexagonal 2×2

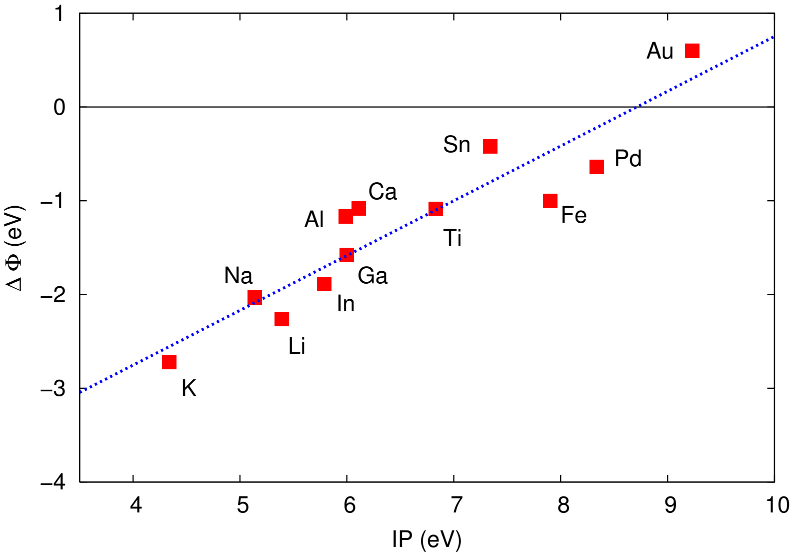

Figure 2.11: Plot of calculated work function shift ($\Delta\Phi$) for the 4×4 coverage versus ionization potential (IP) from experiment (Ref. [117]). The dotted line is given by Eq. 2.8.

K islands form, and the islands are separated by a dispersed phase with spacing corresponding to a 7×7 structure. Further increasing the coverage causes the islands to grow until a full 2×2 monolayer of K is formed ($\theta = 1$ ML for K) [127, 128].

The 4×4 structure used in this work corresponds to a coverage $\theta = 0.25$ ML, which may be above the critical coverage ($\theta_c \approx 0.1 - 0.3$ ML, Refs. [127] and [129]). Therefore, experimentally, the 0.25 ML coverage might consist of a mix of 2×2 islands and the dispersed phase, not a uniform 4×4 phase.

The work function for K on graphite as a function of coverage has been measured experimentally by the retarding potential method and by photoemission spectroscopy [129]. The work function shift relative to clean graphite at $\theta = 0.25$ ML was measured to be about -1.6 eV, while our calculation for the 4×4 structure gives $\Delta\Phi = -2.77$ eV.

The discrepancies between our results and experiment are reasonable if we consider the differences between the 2×2 islands, the dispersed phase, and the 4×4 structure. The 2×2 island structure was experimentally reported to be metallic [127], and compared with the dispersed phase there is less charge transfer and a smaller dipole moment per adatom. For the 2×2 structure, the work function approaches the value for bulk metallic K [129]. At the hypothetical 4×4 structure, it is possible to obtain a large $\Delta\Phi$ because, compared to the more dispersed phase, there is a higher density of polarized adatoms, and compared to the metallic 2×2 phase, there is greater polarization and a larger dipole potential contributing to the work function shift.

2.4 Conclusion

In this chapter, the adsorption of 12 different metal adatoms on graphene is studied using first-principles density-functional theory. Calculations of adsorption energy, geometry, density of states, charge transfer, dipole moment, and work function give a consistent picture of bonding for the adatoms considered. Adatoms from Groups I-III exhibit characteristics of ionic bonding, including adsorption to the H site, small distortion of the graphene sheet, little change in the graphene electronic states, and significant charge transfer and work function shifts. For these adatoms, charge transfer is calculated quantitatively using two methods, one based on the DOS and the other based on the integration of the real space charge density. The observed trends differ for these two definitions, demonstrating their different physical meanings. The work function can be understood to have two main contributions coming from the dipole potential and from the Fermi level shift due to graphene band filling. Transition metal atoms with d valence electrons, noble metals, and Group IV elements exhibit covalent bonding characteristics with strong hybridization of adatom and graphene electronic states. The utility of the charge transfer concept is less clear than in the ionic case, but both ionic and covalent adatoms follow a linear relationship between $\Delta\Phi$ and the IP. Our work can serve as a basis for future experimental and theoretical studies of adsorption on graphene. In the next chapter, we go on to study the gating of adatoms on graphene.

Chapter 3

Gated adatoms on graphene

In this chapter, a first-principles pseudopotential density-functional method for studying the gating of adatoms on graphene is presented. A variation in gate voltage is assumed to vary the number of electrons in the adatom-graphene system. The method is applied to the cases of Li and Co on graphene. The projected density of states, charge density, and local electrostatic potential are computed as a function of gate voltage. In the case of Li, the calculations show that the Li adatom can be ionized by changing the gate voltage, and that the ionization is accompanied by a sharp change in the electrotstatic potential of the adatom. In the case of Co, correlation in the $3d$ shell is treated using the LDA+U method, with several values of the U parameter considered. For $U = 2$ eV or greater, an ionization effect analogous to the case of Li is found for the Co adatom. This result is consistent with recent scanning tunneling spectroscopy experiments for Co on graphene. Work presented in this chapter has been published in Ref. [130].

3.1 Introduction

In Chapters 1 and 2, some of the remarkable properties of graphene were discussed. The modification of pristine graphene is crucial for the study and elucidation of its properties, as well as for tailoring it for practical applications. Modifications that have received attention recently include growing or placing graphene on a variety of substrates [131–135], applying mechanical strain [136, 137], patterning graphene into nanoribbons or dots [138–140], and forming bi- or multi-layer graphene [82, 141].

Two important modifications are the variation of the carrier concentration of graphene via an applied gate voltage and the adsorption of adatoms or molecules on the graphene surface. It has been shown that gate voltages applied to graphene on a SiO_2 substrate can induce both electron and hole carriers up to a concentration of $n \sim 10^{13}$ cm^{-2} via the field effect [3]. With electrochemical gating, carrier concentrations of $n \gtrsim 10^{14}$ have been reported for graphene [142, 143]. The field effect is possible because of the semimetallic nature of graphene, with linear DOS that vanishes at the charge neutrality point (NP) or Dirac point, and the 2D nature of graphene makes for a straightforward experimental geometry. The field effect was important in early measurements on graphene confirming high mobility and Dirac quasiparticles in graphene [3, 131, 144, 145].

In Chapter 2, studies of metal adatom adsorption on graphene were presented. As a 2D material, graphene is naturally amenable to the addition of adsorbates. Experimentally, adsorbates on graphene have been used as dopants that change the number of charge carriers [80, 146, 147], as sources of scattering in transport measurements [81], or as a method of band gap opening or otherwise altering the electronic structure of graphene [82,148,149]. In addition to considering the above phenomena, theoretical work on adsorbates on graphene has explored other possibilities, such as the formation of regular arrays of adsorbates, the existence of local moments, Kondo physics, and magnetically ordered arrays, and exotic phenomena such as atomic collapse [150].

In graphene, variation of the gate voltage and adatom or molecule adsorption can be combined in the same system. In this way, the chemical potential of the adsorbate-graphene system can be precisely controlled. In some cases, such control can be used to explore the electronic structure of an adatom-graphene system over a range of energies [81]; in other cases, it can be used to carefully tune the properties of the adsorbate-graphene system, such as in the optimization of a graphene chemical sensor [147] or in the possible tuning of the Kondo effect [151, 152].

A recent scanning tunneling spectroscopy (STS) experiment demonstrated the ability to controllably ionize a Co adatom on graphene using either a back gate voltage or the STS tip bias voltage [17]. The charging of a localized state on a surface has been demonstrated using STS on other systems [153–156], but those experiments lacked the precise control of ionization via backgate voltage that is possible on graphene. Given that STS is a natural tool for studying single adatoms on graphene, the amount of experimental data for STS on such systems should grow in the near future.

The unique opportunity that graphene presents to control the chemical potential of adsorbates on graphene using a gate voltage motivates the theoretical study of the gating of adatoms on graphene. In this chapter, we present a first-principles method for studying gated adatom-graphene systems. The method is applied to a prototype system, a Li adatom on graphene, as well as a more experimentally relevant case, Co on graphene. The electronic structure, including the density of states, charge density, and local electrostatic potential, is computed as a function of gate voltage. For both Li and Co on graphene, we find the presence of atomic-like states that remain localized on the adatom. Our results show that such states can be ionized by variation of the gate voltage, and that such ionization induces a sharp change in the local electrostatic potential, in agreement with the recent STS experiment. This method has the potential to be applied to a wide variety of other adatoms and molecular adsorbates.

The chapter is organized as follows. In section 3.2 we present the model and details of the calculation. Sections 3.3 and 3.4 present the results for Li and Co adatoms on graphene, respectively. In section 3.5 we discuss our results in relation to experiment, as well as some implications of our results. Section 3.6 concludes the chapter.

3.2 Method

3.2.1 Computational Framework

Our calculations are performed using the first-principles plane-wave pseudopotential method [27] and density-functional theory (DFT) [20, 21] using the spin-polarized generalized gradient approximation functional of Perdew, Burke, and Ernzerhof (PBE) [26]. The Quantum-ESPRESSO package [157] is used to perform the calculations. Ion cores are modeled using ultrasoft pseudopotentials [41]. [1] For C and Li, the $n = 1$ shell is treated as core and $n = 2$ as valence; for Co, $3s$ and $3p$ electrons are treated as core, while $4s$ and $3d$ are treated as valence. A nonlinear core correction is included for Li [40]. The electronic valence states are modeled using plane-waves with an energy cutoff of 45 Ry for the wavefunctions and 180 Ry for the charge density for Co on graphene, and 30 Ry and 120 Ry respectively for Li.

In the case of Co, we consider the possible strong correlations in the $3d$ shell using the so called LDA+U method [59] (or GGA+U in this work). In this approach, a Hubbard U term is added to the functional to model the Coulomb repulsion between $3d$ electrons localized on the Co atom. We use the rotationally-invariant formulation within a plane-wave psuedopotential framework, as described in Ref. [55]. Note that a single Coulomb parameter U is used (the exchange parameter $J = 0$ eV). We consider three values for U: 0, 2 and 4 eV.

The calculations are performed for an adatom on graphene in a supercell with periodic boundary conditions. For the graphene in-plane (x-y) directions, a 6×6 supercell containing 72 C atoms and 1 adatom is used (Fig. 3.1). We use the lattice constant of 2.463 Å that we calculated for clean graphene; thus the distance between adatoms in our supercell arrangement is 14.78 Å. In the out-of-plane z direction perpendicular to the graphene plane, the unit cell length is 15 Å. The Brillouin zone is sampled using a $3 \times 3 \times 1$ Γ-centered k-point grid, and a Gaussian smearing of 0.05 eV is used for the electronic occupations.

The electronic density of states (DOS) is computed using a $21 \times 21 \times 1$ Γ-centered k-point grid (a 0.1 eV Gaussian smearing is used in the plots). The projected DOS (PDOS) is computed by projecting the electronic wavefunctions onto orthogonalized pseudoatomic orbitals; orbital occupations are obtained from the Löwdin analysis.

We consider three adsorption sites of high symmetry (as in Chapter 2): hollow (H), at the center of a hexagon; bridge (B), at the midpoint of a C-C bond; and top (T), on top of a C atom. The adsorption height h of the adatom, defined as the perpendicular distance between the adatom and the graphene plane (Fig. 3.2), is optimized such that the force on the adatom is less than 0.001 Ry/a.u. The C atoms in graphene are kept fixed at their coordinates for a perfect graphene sheet. For calculations of the same adatom at different levels of doping (discusssed in Section 3.2.2), the adatom height is optimized at zero doping (neutral charge) and then kept constant across all doping values. The effects of the approximation of fixed adatom height and C positions are discussed in Section 3.5.

---

[1] We used the pseudopotentials C.pbe-rrkjus.UPF, Li.pbe-n-van.UPF, and Co.pbe-nd-rrkjus.UPF from http://www.quantum-espresso.org.

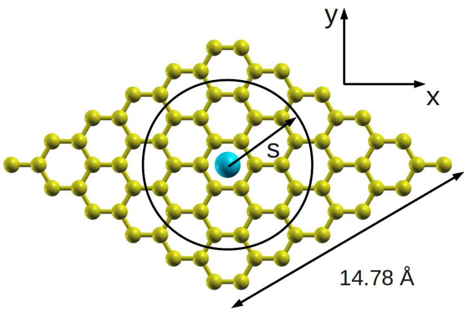

Figure 3.1: Adatom on hollow site in 6 × 6 unit cell. The view is along the $-z$ direction, perpendicular to the graphene plane. A circle of radius s centered around the adatom in the x-y plane is indicated.

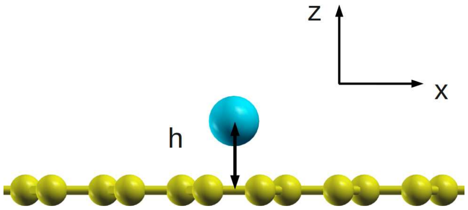

Figure 3.2: View of an adatom on graphene along the $+y$ direction of the unit cell. The height h is defined as the perpendicular distance above the graphene plane.

3.2.2 Modeling of the applied gate voltage

In experimental studies, the application of a gate voltage to the adatom-graphene system changes the total charge of the sample by adding or removing electrons and changing the chemical potential. We model this effect in our calculation by varying the total charge of the system from the neutral value by adding or removing electrons (doping the system). We consider several values of the total charge that range below and above neutral. For each given value of total charge considered, we fix the corresponding number of electrons per unit cell and perform a full self-consistent calculation of the electronic structure. Thus the Kohn-Sham electronic orbitals are allowed to relax according to the doping level. This method can be contrasted with a rigid-band model in which addition or removal of electrons changes the occupation of the electronic orbitals, but the orbitals themselves remain unchanged.

For a doping level away from neutral, the calculation involves a charged supercell. We employ a standard method for cancelling the divergence of the total energy for charged supercells, which is to add a compensating uniform (constant in space) background charge of opposite sign and with total magnitude equal to the net charge of the electrons plus ions in the system. (See, for example, Ref. [95].)

3.2.3 Supercell interactions

We briefly discuss the supercell interacations present in our calculations. In the z-direction perpendicular to the plane, the 15 Å separating periodic images is sufficient to make overlap of wavefunctions on neighboring images negligible. However, monopole (for charged systems), dipole, and higher order electrostatic interactions between periodic images are present. It is possible to correct for such interactions [158,159]; such corrections are not included in the work described in this chapter.

For the graphene in-plane directions, we take the 6 × 6 supercell containing one adatom and 72 C atoms to approximate a single adatom on an infinite graphene sheet. The choice of supercell size minimizes the bandwidth of localized atom-derived states while maintaining a reasonable computational cost. Due to their long range nature, electrostatic interactions between periodic images are not negligible. Therefore, we do not expect the long-range effects of gating adatoms on graphene to be captured accurately by our calculations. Note also that in order to model effects such as ionization of the adatom, one must dope the system on the order of 1 electron (e) per adatom, which corresponds to a charge density of 1 e/72 C, while in experiments for graphene on SiO_2, the doping range is approximately ± 1 e/1000 C. Despite the presence of long range electrostatic interactions between periodic images and the discrepancy with experimental doping level, we believe the 6 × 6 supercell is a reasonable approximation for the local behavior (within several Å) of the adatom on graphene under applied gate voltage.

Alternatively, for a system consisting of an adatom layer at a concentration of $\sim$ 1 adatom/72 C (as opposed to a single adatom) on graphene, the supercell interactions are physical and the 6 × 6 supercell is a reasonable approximation. However, in this case the large doping of $\sim 1e/72$ C may not be experimentally achievable.

3.3 Lithium adatom on graphene

We consider the adsorption and gating of Li adatoms on graphene as a prototype. Li and other alkali atoms are often used in carbon nanotube and graphitic systems as a dopant, for example in graphite intercalation compounds [160]. Possessing one valence electron, an alkali adatom binds to graphene at the hollow site, transferring close to one electron to the graphene sheet, according to the calculations of Chapter 2. In the present calculation, the Li atom is modeled with a pseudopotential with one valence electron in the $2s$ state.

We reconfirm that the lowest energy binding site for Li on graphene is the hollow site. Our calculated adsorption height of 1.89 Å is somewhat larger than previous DFT-PBE calculations that treat Li $1s$ semicore states as valence (Table 2.1 and Refs. [99,100]) but is in good agreement with calculations for which Li $1s$ semicore states are treated as core [101]. Figure 3.3a shows the PDOS for the neutral Li-graphene system. The spin-up and spin-down states are degenerate. There is an atomic-like state A deriving from the Li $2s$ and $2p$ orbitals 1 eV above the Fermi level (E_F), while the Dirac point of the graphene DOS lies 0.7 eV below E_F. We interpret this result as a complete transfer of the single valence electron of the Li atom to the graphene sheet.

In Fig. 3.3, the PDOS for several levels of doping are plotted. The primary feature that we focus on is the ionization of the Li adatom as the doping is changed from 0 e to +3 e, or vice versa (unless otherwise noted, doping levels are quoted in number of electrons per unit cell, relative to neutral). Let us consider the progression from 0 e to +3 e doping. At

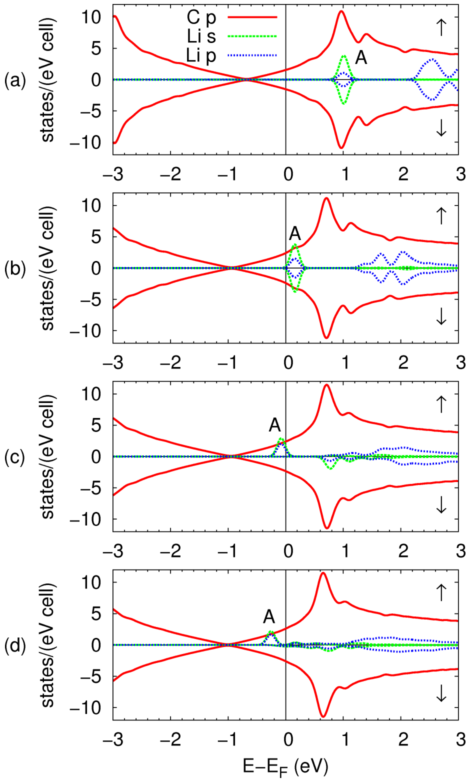

Figure 3.3: PDOS for Li adatom on graphene for various dopings: (a) 0 e (b) +1 e (c) +2 e (d) +3 e. Projections onto C 2p (solid red), Li 2s (dashed green), and Li 2p (dotted blue) are shown. Arrows indicate majority (up) and minority (down) spin channels. A state localized on the Li adatom is labeled A. Energies are relative to the Fermi energy E_F.

a doping of +1 e, as in the 0 e case, a localized state A deriving from the Li atom is clearly distinguishable and remains unoccupied. At +2 e doping, the A state becomes partially occupied in the spin-up (majority) channel. Note also the splitting between up and down spins for the localized state, which is the same in origin as the splitting between occupied spin-up and unoccupied spin-down 2s states in an isolated Li atom. At +3 e doping, the Li spin-up peak A is completely occupied, with the Li spin-down states remaining unoccupied. We interpret this result as the increase in ionization state of the Li adatom by 1 e. Importantly, the A peak does not appear to hybridize with the graphene states at any level of doping, which suggests that the state is localized on the Li atom. Therefore, orbitals for the Li-graphene system can be assigned relatively unambigously to either the graphene or to the Li adatom.

When a free atom is ionized, the electrostatic potential due to the atom changes, since the contribution to screening of the potential from the added or removed electron changes. We find a similar effect for the ionization of the Li adatom on graphene. From our self-consistent field calculations, we extract the local electrostatic potential (bare ionic pseudopotential plus electronic Hartree potential), $V_{BH}(\vec{r})$, for the system. (In this work, "potential" refers to the potential energy for an electron.) To compare V_{BH} for several different dopings, we consider the difference

$$\Delta V_{BH}(\vec{r}) = V^{n}_{BH}(\vec{r}) - V^{\mathrm{gr}}_{BH}(\vec{r}), \tag{3.1}$$

where V^{n}_{BH} is the potential for the adatom-graphene system with doping level n, and V^{gr}_{BH} is the potential for a clean graphene sheet with zero doping.

We consider the quantity

$$\Delta V_{BH}(s,z) = \frac{1}{2\pi s}\int_0^{2\pi} \Delta V_{BH}(s,\theta,z)d\theta, \tag{3.2}$$

the average of ΔV_{BH} over a a ring of radius s, centered around the adatom x-y position, at a height z above the graphene plane, and parallel to the plane (see Figs. 3.1 and 3.2); the position $\vec{r} = (s,\theta,z)$ is expressed in cylindrical coordinates. In Fig. 3.4 we plot $\Delta V_{BH}(s,z)$ for several different heights. The plots are aligned so that the potentials are zero at a distance from the adatom of $s = 7.39$ Å, equal to one-half the lattice constant of the 6 × 6 unit cell.[2] For comparison, we also plot $V^{\mathrm{Li}}_{B}(s,z)$, the local bare ionic pseudopotential for Li.

Compared with the potential at zero doping, the potential with +1 e has almost the same shape for all the heights plotted. However, the addition of another electron brings about a sharp change in the V_{BH}; the potential becomes significantly shallower. The addition of a further 1 e does not change the potential signifcantly, aside from a constant.

Comparing the potentials at different heights, we see that near the graphene sheet (h = 0.0 and 0.7 Å), the adatom potential is already screened strongly by the graphene electrons at 0 e doping, resulting in a V_{BH} that is much shallower than the bare ionic Li potential. The change in potential at $s = 0$ from +1 e to +2 e is about 0.3 eV. In contrast,

---

[2] A more natural way to align the potentials would be to set them to zero at a distance far from the adatom, where the potential is close to that of a clean graphene sheet, but due to the limited supercell size in the calculation, the potential at the edge of the unit cell is not converged to the clean graphene limit.

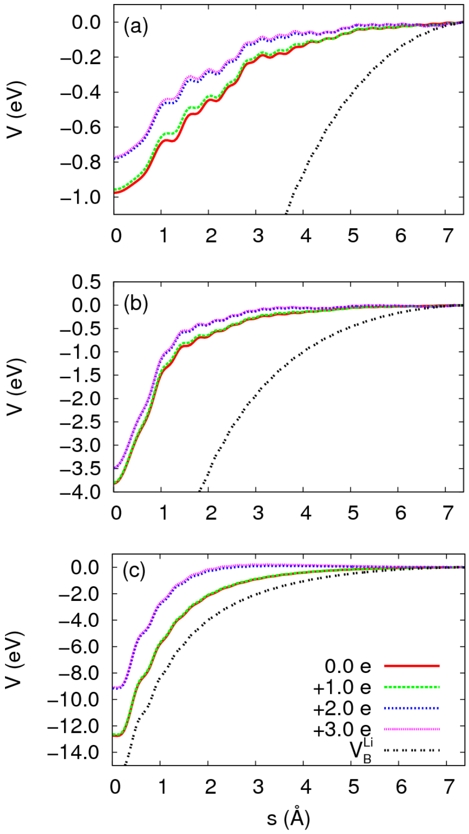

Figure 3.4: Plots of $\Delta V_{BH}(s,z)$ for a Li adatom on graphene for several doping values and at heights $z =$ (a) 0 Å, (b) 0.7 Å, and (c) 2.7 Å above the graphene plane. The local ionic potential for Li, $V_B^{\mathrm{Li}}(s,z)$, is also plotted.

the potential at $h = 2.7$ Å is weakly screened up to $+1$ e doping but becomes more strongly screened at $+2$ e doping, with a change in V_{BH} of approximately 4 eV at $s = 0$.

Comparison of the plots of the potential to the PDOS plots shows that filling of graphene-like states when going from 0 e to $+1$ e doping does not change the potential significantly (except by a constant), while the ionization of the Li adatom when increasing the doping from $+1$ e to $+2$ e corresponds to a sharp change in the shape of the potential. These changes in the potential can be understood by considering how the charge density changes as the doping level is increased. Define the charge density difference

$$\Delta\rho(\vec{r}) = \rho_n(\vec{r}) - \rho_0(\vec{r}), \tag{3.3}$$

where $\rho_n(\vec{r})$ is the charge density of the adatom-graphene system with doping level n, and $\rho_0(\vec{r})$ is the charge density at a reference doping level. For Li we take 0 e as the reference doping level. As we did for ΔV_{BH}, we take the circular average

$$\Delta\rho(s, z) = \frac{1}{2\pi s} \int_0^{2\pi} \Delta\rho(s, \theta, z) d\theta \tag{3.4}$$

for radius s and height z.

Figure 3.5 shows $\Delta\rho(s, z)$ for various heights. Upon filling the graphene-like states when going from 0 e to $+1$ e doping, the charge density near the graphene changes fairly uniformly across the 2D graphene plane, increasing at $h = 0.7$ Å and decreasing slightly at $h = 0$ Å. At $h = 2.7$ Å the charge density changes little. This result is consistent with the additional electrons occupying graphene π^* orbitals which lie above and below the graphene plane and are delocalized across the graphene sheet. The local Hartree potential due to such a uniform (in the x-y plane) charge density is also uniform. Therefore the difference in V_{BH} between 0 e and $+1$ e should be nearly constant, as is found in our calculations.

On the other hand, when the doping is increased from $+1$ e to $+2$ e, the charge density at $h = 2.7$ Å shows a much larger increase near the adatom than away from it, while nearer to the graphene plane, the charge density change is small. (At $h = 0.7$ Å the charge density actually decreases near the adatom and increases away from it, but the magnitude of charge density change is small compared with that calculated at $h = 2.7$ Å.) This charge density change corresponds to occupation of an orbital localized on the Li adatom, above the graphene plane (i.e., ionization of the Li adatom). Since the local Hartree potential is greater at points of greater charge density, the large increase in charge density near the Li adatom increases V_{BH} near the adatom relative to points further from the adatom, consistent with our calculations. Furthermore, the change in V_{BH} is sharp because the charge density is concentrated on the adatom, rather than spread out over a plane.

A notable feature of the PDOS is the change in orbital character of the A peak. At 0 e doping, the A peak has mostly Li $2s$ character, but has some $2p$ character, since the spherical symmetry of the potential near the Li adatom is broken by the graphene. As the doping is increased, the $2s$ character of the peak decreases and the $2p$ character increases. A possible explanation is that the orbital becomes more extended into the vacuum and less localized on the Li adatom. The orbital becomes more extended because the increase

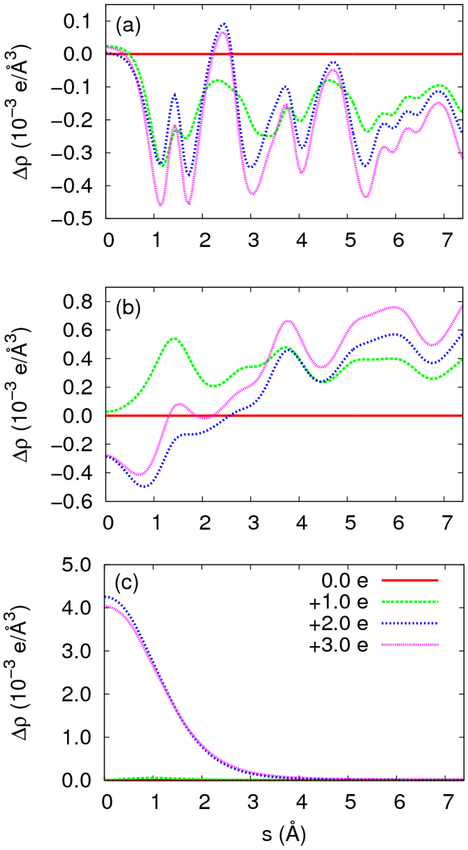

Figure 3.5: Plots of $\Delta\rho(s, z)$ for a Li adatom on graphene for several doping values and at heights $z =$ (a) 0 Å, (b) 0.7 Å, and (c) 2.7 Å above the graphene plane.

in charge on the graphene increases the Hartree potential, pushing the wavefunction away from the graphene.

To summarize the results for Li on graphene, the PDOS calculations show that the Li adatom is ionized when the doping is increased or decreased between 0 e and +3 e. The ionization corresponds to a large change in charge density localized on the Li adatom and a sharp change in V_{BH}, in analogy with the ionization of a free atom.

3.4 Cobalt adatom on graphene

Our study of Co adatoms on graphene is motivated by recent STS experiments on this system, in which it was found that the Co adatom could be controllably ionized by gate or tip bias voltage [17]. In addition, the Co atom has a partially occupied 3d shell and therefore has the possibility of forming a local moment on graphene. Several theoretical works have studied the Kondo physics of Co on graphene [161–163] and of adatoms on graphene in general [151, 164–167], but we do not consider the Kondo effect in this work.

Following the example of Li on graphene presented in Section 3.3, we start with the undoped case. For plain GGA ($U = 0$ eV) we find that the lowest energy binding site is the H site with a binding height of 1.56 Å above graphene, in reasonable agreement with other works [112, 161–163, 168, 169]. For $U = 2$ and 4 eV, we also find the H site to be lowest in energy, with heights of 1.75 and 1.88 Å, respectively.[3]

Figures 3.6c, 3.7c, and 3.8c show the PDOS for the neutral Co-graphene system for the three values of U considered in this work. Due to symmetry, the five 3d orbitals (for a given spin) split into a singly degenerate A_1 orbital, deriving from the d_{z^2} atomic orbital, a doubly degenerate E_1 orbital, derving from d_{zx} and d_{zy} orbitals, and a doubly degenerate E_2 orbital, deriving from $d_{x^2-y^2}$ and d_{xy} orbitals. The E_1 and E_2 orbitals hybridize strongly with the graphene sheet, while the A_1 and 4s orbitals hybridize weakly or not at all with graphene, although they can hybridize with each other.

For $U = 0$ eV, the spin-up Co 3d states are almost completely occupied (occupancy 4.7), while the spin-down 3d states are partially occupied (occupancy 3.6), with the E_1 orbital lying at E_F. The spin-up and spin-down Co 4s states have occupancies close to zero (0.1). Thus the Co atom orbital occupation is $3d^{8.3}4s^{0.2}$. The Dirac point E_D of the graphene lies slightly below E_F, indicating a small amount of charge transfer from Co to graphene, consistent with the reduction in occupation on the Co atom from 9 for the free atom to 8.5 on graphene.

The addition of a U of 2 eV changes the PDOS significantly. In comparison to the $U = 0$ eV case, the 3d levels are shifted away from E_F, and the occupations of the 3d levels are pushed to near-integer values. These effects are typical for the LDA+U method [59]. The spin-up 3d states remain near-fully occupied (occupancy 4.9), while the spin-down 3d state occupancy is 3.0; the E_1 orbitals have been pushed ∼1.0 eV above E_F by the addition of the U, and their occupation is reduced to zero. On the other hand, the spin-up Co 4s state is partially occupied (occupancy 0.7) and lies at E_F. In this case, the Co atom orbital

---

[3] If the C atoms in graphene are allowed to relax, the H site remains the lowest in energy for $U = 0$ and 2 eV, but the T site is lowest in energy for $U = 4$ eV. This result is consistent with Ref. [162].

occupation is $3d^{7.9}4s^{0.7}$. The effect of the additional $U = 2$ eV is to transfer approximately 0.5 e from the $3d$ orbital to the $4s$ orbital of Co.

The $U = 4$ eV case is similar to the $U = 2$ eV case. The Co $4s$ states and E_D have approximately the same position relative to E_F, and the occupancies of the Co $3d$ states are the same. However, the Co $3d$ states are shifted further from E_F by the larger U value.

Our PDOS calculations for $U = 0$ eV (plain GGA) are in good agreement with previous works [163,168,169]. In addition, our PDOS for $U = 0$ and $U = 2$ eV correspond well to two configurations found in another work (Figs. 1(a) and 1(b) in Ref. [162]).

We now consider the doping dependence of the PDOS for Co on graphene. Figure 3.6 shows the PDOS for $U = 0$ eV for various levels of doping. At a doping of -2 e, the spin-down E_1 orbital is unoccupied, as are some graphene π states, with E_D lying above E_F. As the doping is increased, the occupation of the spin-down E_1 orbital increases, as does the occupation of both spin-up and spin-down graphene states. We find that as the occupation of the spin-down E_1 orbital changes, the orbital stays pinned to E_F, in contrast to the graphene-derived states. Comparing the energy of the E_1 peak to the Dirac point of graphene, we find that at low doping, when E_1 is unoccupied, it lies below E_D, but at high doping, E_1 becomes mostly occupied and its energy is above E_D. The increase in occupation of the $3d$ shell coincides with a shift towards higher energy of the occupied $3d$ levels as well. Increasing the doping from $+1$ e to $+2$ e, The occupations of both the spin-down E_1 and spin-up $4s$ orbitals increase simultaneously.

The PDOS for U= 2 eV and $U = 4$ eV (Figs. 3.7 and 3.8) show similar trends with respect to gating that differ from the $U = 0$ eV case. We focus the discussion on the results for the $U = 2$ eV calculations. As for the case of Li, we focus on the ionization of the Co adatom by gating. Just as for the zero doping case, for doping levels between -2 e and $+2$ e, the effect of the U is to shift the $3d$ levels away from E_F. As a result, the effect of gating is to ionize the Co adatom by occupying or unoccupying the $4s$ level, which is localized on Co and hybridizes only weakly with graphene.

The ionization of Co by changing the occupation of the $4s$ level is analogous to the ionization of Li by changing the occupation of the $2s$ level. In Figs. 3.9 and 3.10, we plot $\Delta V_{BH}(s,z)$ and $\Delta\rho_{BH}(s,z)$ for Co on graphene with $U = 2$ eV at selected heights for several doping values. The quantities $\Delta V_{BH}(s,z)$ and $\Delta\rho_{BH}(s,z)$ are defined in Eqs. 3.1-3.4, in the same way as for Li. The bare ionic pseudopotential for Co, $V_B^{\mathrm{Co}}(s,z)$, is also plotted. Note that the Co ion core has charge $+9$ e, so that even at -2 e doping of the Co-graphene system, the ionic potential is screened by $\sim$ 8 electrons localized on the Co adatom, unlike in the Li case. For Co, we take -2 e as the reference doping level for $\rho_0(\vec{r})$ in the definition of $\Delta\rho(\vec{r})$ (Eq. 3.3). Just as in the Li case, V_{BH} for the graphene case shows a sharp change upon ionization of the Co adatom, and the added charge density that ionizes Co is localized close to the adatom (within a few Å in the x-y plane). Furthermore, the change in the charge density near the graphene plane for Co (Figs. 3.10(a) and (b)) is simlar to the case of Li (Figs. 3.5(a) and (b)).

Interestingly, in the $U = 4$ eV case, when the doping changes from $+1$ e to $+2$ e, the configuration of the $3d$ shell changes abruptly. The A_1 state becomes unoccupied, while the E_1 state becomes occupied. Apparently, at a large enough doping, increasing the occupation of the $3d$ shell becomes favorable, but in order to satisfy near-integer occupations of

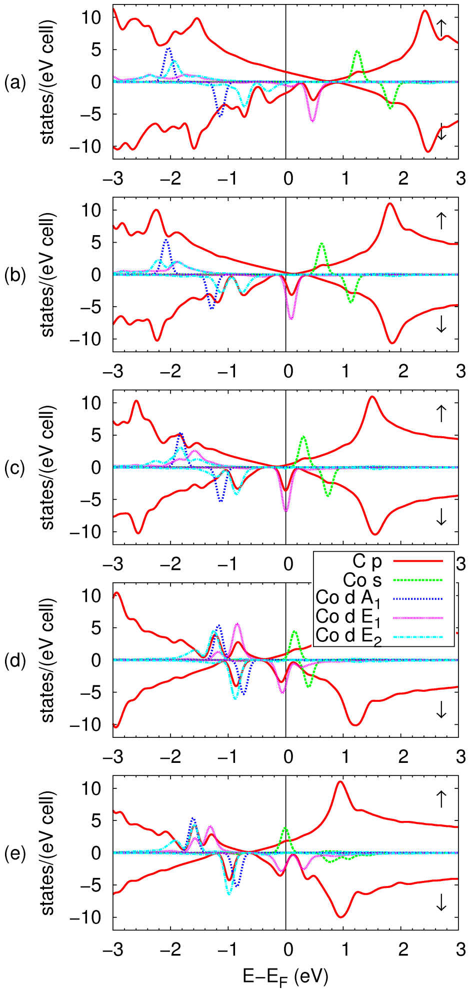

Figure 3.6: PDOS for Co adatom on graphene with $U = 0$ eV for various dopings: (a) $-2\ e$ (b) $-1\ e$ (c) $0\ e$ (d) $+1\ e$ (e) $+2\ e$. Projections onto C $2p$ (solid red), Co $4s$ (dashed green), Co $3d$ A_1 (dotted blue), Co $3d$ E_1 (small-dotted magenta), and Co $3d$ E_2 (dash-dotted cyan) are shown. Arrows indicate majority (up) and minority (down) spin channels. Energies are relative to the Fermi energy E_F.

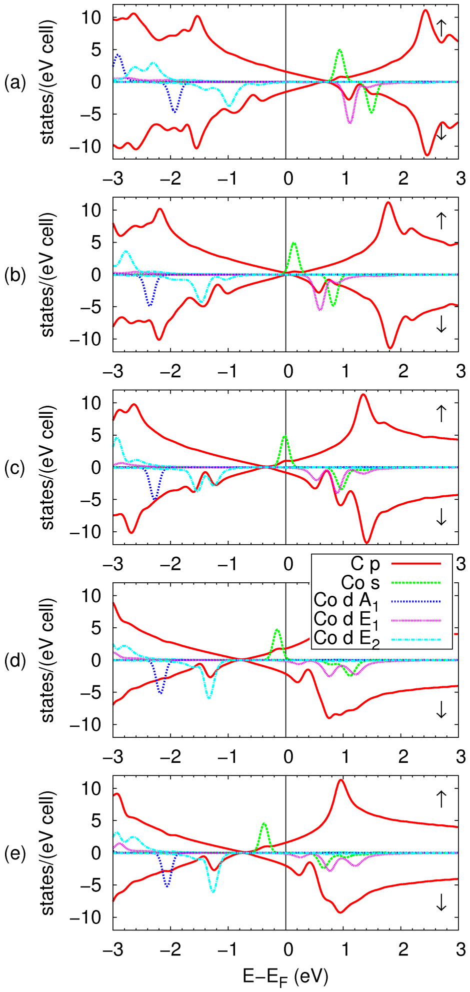

Figure 3.7: PDOS for Co adatom on graphene with $U = 2$ eV for various dopings: (a) $-2\ e$ (b) $-1\ e$ (c) $0\ e$ (d) $+1\ e$ (e) $+2\ e$. Projections onto C $2p$ (solid red), Co $4s$ (dashed green), Co $3d$ A_1 (dotted blue), Co $3d$ E_1 (small-dotted magenta), and Co $3d$ E_2 (dash-dotted cyan) are shown. Arrows indicate majority (up) and minority (down) spin channels. Energies are relative to the Fermi energy E_F.

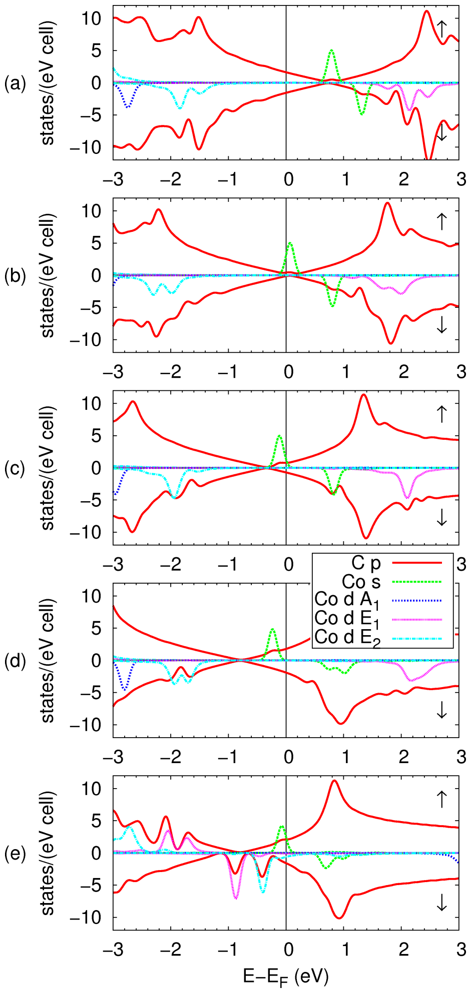

Figure 3.8: PDOS for Co adatom on graphene with $U = 4$ eV at various dopings: (a) -2 e (b) -1 e (c) 0 e (d) $+1$ e (e) $+2$ e. Projections onto C $2p$ (solid red), Co $4s$ (dashed green), Co $3d$ A_1 (dotted blue), Co $3d$ E_1 (small-dotted magenta), and Co $3d$ E_2 (dash-dotted cyan) are shown. Arrows indicate majority (up) and minority (down) spin channels. Energies are relative to the Fermi energy E_F.

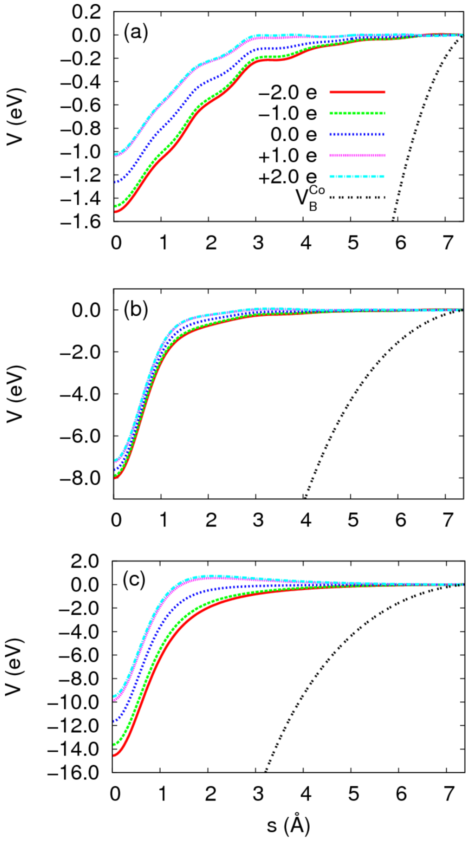

Figure 3.9: Plots of $\Delta V_{BH}(s,z)$ for a Co adatom on graphene with $U = 2$ eV for several doping values and at heights $z =$ (a) 0 Å, (b) 0.7 Å, and (c) 2.7 Å above the graphene plane. The local ionic potential for Co, $V_B^{\mathrm{Co}}(s,z)$, is also plotted.

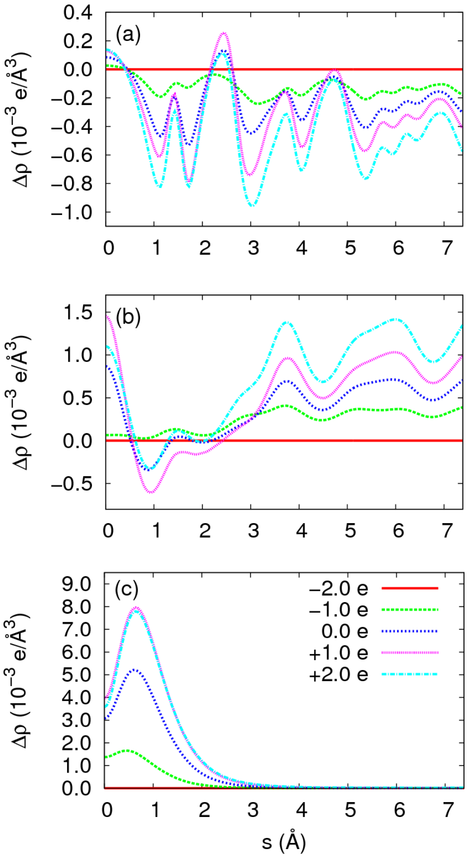

Figure 3.10: Plots of $\Delta\rho(s, z)$ for a Co adatom on graphene with $U = 2$ eV for several doping values and at heights $z =$ (a) 0 Å, (b) 0.7 Å, and (c) 2.7 Å above the graphene plane.

the orbitals (favored by the LDA+U), the doubly degenerate E_1 orbital becomes (approximately) fully occupied, rather than occupying the A_1 orbital and partially occupying the E_1 orbital.

To summarize the results for Co on graphene, we find that the choice of the U parameter has significant effects on the PDOS. For $U = 0$ eV, the gate voltage can change the occupation of both $3d$ and $4s$ orbitals. For $U = 2$ or 4 eV, the gate voltage can ionize the $4s$ orbital in a manner analogous to the Li adatom case.

3.5 Discussion

In this section, we discuss some implications of this work. In Ref. [17], Co atoms on a graphene surface with a controllable gate voltage were studied using scanning tunneling spectroscopy. Our calculations for Co on graphene are in agreement with the experimental results in several respects. In our calculations of the PDOS, we find resonances near E_F that derive from Co adatom states, and these resonances are localized around the adatom. Similarly, the experimentally measured differential conductance (dI/dV) on top of the Co atom shows resonances near E_F. Although experimentally these resonances cannot be identified unambiguously as coming from Co atomic-like states, their behavior with respect to a change in gate voltage was measured and is in agreement with the behavior of the peaks in our calculation. In both cases, the position of the resonances relative to E_F can be shifted by application of the gate voltage. In particular, the peaks can be shifted above or below E_F, changing the occupation of the atomic-like state and the ionization state of the adatom.

Furthermore, our calculation shows that the change in ionization of the Co adatom is accompanied by a sharp change in the electrostatic potential at and around the adatom. This sharp change in the potential is induced whenever the adatom is ionized, whether by the gate voltage or by the STS tip. The sharp change in the potential upon ionization is consistent with a large response in the dI/dV signal seen in experiment, both when varying the tip-sample bias with the STS tip above the adatom, and when varying the tip position at fixed gate and bias voltages.

In these respects, our calculation is in good qualitative agreement with several features in experiment. Due to several approximations in our calculation, the agreement with experiment cannot be considered quantitative, but by treating these approximations more exactly, the calculations might be brought in better quantitative agreement. In our calculation, we neglect the SiO_2 substrate upon which the graphene sits in experiment. It is known that graphene on SiO_2 has corrugations [170] and "charge puddles" [16] that can affect the electronic structure of graphene. However, the charge puddles cause fluctuations in E_D of only 30 meV and have spatial width of 20 nm, so on the scale of an atom, the charge puddles only shift the reference doping level for zero applied gate voltage. The corrugations could have some effect on the binding site and geometry of the Co adatom on graphene.

Our calculations also assume that the C and adatom positions remain fixed as the doping level is changed. In Chapter 2, it was found that adatom adsorption on the H site induced little distortion in the graphene lattice. Therefore, for the undoped adatom-graphene system, a rigid graphene lattice approximation is reasonable. Upon doping, we might expect the adatom height to change somewhat. This could affect the hybridization between the adatom and graphene in the case of Co. We do not expect doping to distort the graphene lattice much because the change in charge density is mostly either delocalized across the graphene plane or, when localized, centered on the adatom, not on the C atoms. The exception might be Co for $U = 0$ eV, in which case some distortion and shifting of energy levels is possible.

Another approximation is the use of Kohn-Sham eigenvalues for the electronic spectra. While this approximation often gives reasonable results, the spectra may be modified by many-body effects. The use of three values for U in our calculations reflects some uncertainty in the treatment of correlation in the Co-graphene system. Our results show that the value of U affects the binding height and the character of the Co resonances near E_F in the electronic DOS. Other works in the literature have considered other approximations to correlation in this system [161–163], and further work on this topic would be worthwhile.

The effects of the supercell approximation have been considered in Section 3.2.3. We also note that the experimental results include the effects of the scanning tunneling microscopy tip, but our calculation does not include such effects.

Despite these approximations, our calculations capture well the experimental observation of gate-induced ionization, and there is the possibility of further quantitative improvement of these calculations.

In the case of Li on graphene, we found that the Li adatom can be controllably ionized by the gate voltage in a manner similar to the Co case. Such ionization may not be experimentally realizable due to the large energy difference between the Li atomic-like state and E_D. Nevertheless, Li on graphene serves as a model system to understand the gating of adatoms on graphene theoretically.

The gating of adatoms on graphene opens the possibility of controllably tuning the chemistry of adatoms or molecules on a graphene surface by the application of a gate voltage, which would have many exciting possibilites for catalysis, hydrogen storage [171], and other applications which may yet be discovered. The periodic table offers a wide variety of atoms for experimental and theoretical study, not to mention molecules. While not all atoms or molecules will be gateable experimentally, the method described in this work can be used to search for and predict specific adsorbates for which tuning the electronic structure by gating is experimentally realizable.

3.6 Conclusion

In conclusion, this chapter presents a method for studying the gating of atoms on graphene using first principles calculations. A Li adatom on graphene serves as a useful model for understanding the gating of adatoms on graphene. By calculating the electronic structure, including the PDOS, potential, and charge density, we demonstrate the ionization of a Li adatom by doping and a concomitant sharp change in the electrostatic potential. Calculations for Co on graphene demonstrate an ionization effect, analogous to the Li case, which is in good agreement with experimental results. We discuss the various approximations used in this work, and consider ways to improve upon them. Using this method to study other adatoms or molecules may yield interesting new results that can be verified in experiment and may lead to practical applications. In Chapter 4, we present an application of this method to study the idea of adatom "alchemy."

Chapter 4

Possibility of transforming the electronic structure of one species of graphene adatoms into that of another by application of gate voltage

As discussed in Chapter 3, graphene provides many advantages for controlling the electronic structure of adatoms and other adsorbates via gating. In this chapter, using the projected density of states and charge density obtained from first-principles density functional periodic supercell calculations, we investigate the possibility of performing “alchemy” of adatoms on graphene, i.e., transforming the electronic structure of one species of adatom into that of another species by application of a gate voltage. Gating is modeled as a change in the number of electrons in the unit cell, with the inclusion of a compensating uniform background charge. Within this model and the generalized gradient approximation to the exchange-correlation functional, we find that such transformations are possible for K, Ca, and several transition metal adatoms. Gate control of the occupation of the p states of In on graphene is also investigated. The validity of the supercell approxmation with uniform compensating charge and the model for exchange and correlation is also discussed. Work presented in this chapter has been published in Ref. [172].

4.1 Introduction

Much scientific effort is directed towards finding ways to control the electronic properties of materials, thereby opening greater possbilities for understanding fundamental physics and developing practical applications. The application of an electric field via gate voltage is a widely used method for controlling electronic properties of a variety of materials. The most well-known example is the field-effect transistor, a fundamental unit of many modern electronic devices.

Over the past several decades, it has become possible to fabricate smaller and smaller systems with electronic properties that can be controlled by a gate voltage. Because a quantum dot or nanoparticle of size $\sim$100 nm exhibits quantum confinement effects, its total charge, and transport through it, can be controlled electron by electron [173]. The study of quantum dots has led to the observation of fascinating phenomena such as Coulomb blockade and the Kondo effect [174, 175].

Even smaller than such "artificial atoms", single atoms or small molecules would be the ultimate limit of systems whose electronic properties could be controlled. Recent experiments have reported attaining this limit in molecules [176, 177], atoms bonded to organic ligands [178], or dopant atoms in Si [179, 180], by observing Coulomb blockade and Kondo effects. In such systems, engineering wavefunctions [179] and constructing qubits [181] are now a possibility.

Recently, the controllable ionization of a Co atom adsorbed on graphene using a back gate voltage was shown [17]. This experiment demonstrates that gated adsorbates on graphene have great potential as atomic-scale systems with controllable electronic properties. Furthermore, recent theoretical studies have suggested that oxygen diffusion on graphene [182] and fluorine chemical bonding [183] can be controlled with gate voltage. As discussed in Sec. 3.1 of this thesis, graphene has many beneficial properties for control of the electronic structure of adsorbates [4]. Its two-dimensional lattice of carbon atoms offers a clean, structurally robust surface for the adsorption of a wide variety of atoms or molecules. Its surface is amenable to imaging techniques and applications in surface chemistry, unlike atoms embedded in bulk materials. Importantly, neutral graphene has a small, linear density of states (DOS) near the Fermi level (E_F), which enables a large shift of E_F when a gate voltage is applied.

Guided by the idea that a singly-ionized isolated atom is isoelectronic to one of its neighbors in the Periodic Table, we suggest that it is possible to transform, electronically, an adatom on graphene into another adatom by gate-controlled ionization. We use the term "alchemy" to refer to such a transformation. In Chapter 3 of this thesis, we investigated the ionization of adatoms on graphene using first-principles calculations, finding reasonable qualitative agreement with essential features of experiment [130]. In this chapter, we use a similar approach to explore the possiblity of alchemy of adatoms on graphene via gating. Using plane-wave pseudopotential (PWPP) density functional calculations with the generalized gradient approximation (GGA) and periodic supercells, we find that alchemy-like transformations are possible for both s and d valence adatoms, as demonstrated for K, Ca, Co, Ni and Cu adatoms. In addition, the calculations show that the occupation of localized p states of an In adatom on graphene can also be controlled by gate voltage. We discuss some limitations of comparing our model to experimental results, with particular focus on the approximation for exchange and correlation, supercell size, and electrostatic effects of periodic supercell calculations.

4.2 Method

4.2.1 Details of calculation

We perform our calculations using the first-principles PWPP method [27] within the framework of spin-polarized density-functional theory (DFT) [20, 21], as implemented in the Quantum-ESPRESSO package [157]. The GGA exchange-correlation functional of Perdew, Burke, and Ernzerhof is used [26]. Ultrasoft pseudopotentials [41] are employed to model the ion cores for C, Co, Ni, Cu, and In; norm-conserving pseudopotentials [38] are employed for K and Ca. [1] The $4s$ and $4p$ states for K and Ca, $4d$, $5s$, and $5p$ states for In, and $4s$ and $3d$ states for Co, Ni, and Cu are treated as valence states. Nonlinear core corrections [40] are included for K, Ca, Co, Ni, and In. The plane wave energy cutoff for the electronic valence states is 30 Ry for the wavefunctions and 240 Ry for the charge density for K and Ca on graphene, and 40 Ry and 240 Ry, respectively, for Co, Ni, Cu, and In.

For calculations involving transition metals (TM), the LDA+U method [59] is often applied to treat correlations among d electrons. Our main results, given in Section 4.3.1, are restricted to the plain GGA case (U=0). In Chapter 3, the LDA+U method was considered for Co on graphene, and it was found that for U=0 eV, a Co $3d$ state is present at E_F, while for a U of 2 eV or 4 eV, a Co $3s$ state is at E_F. In the present chapter, we further assess the importance of the approximation for exchange and correlation on the PDOS for gated Co, Ni, and Cu adatoms on graphene by performing LDA+U calculations using the implementation of Ref. [55]. We use a U of 4 eV and pseudoatomic orbitals for the projections. The effects of the additional U are discussed in Section 4.3.3.

The calculational geometry consists of an adatom on graphene in a 6×6 supercell [30] with 72 C atoms and 1 adatom. The x and y directions are defined to be parallel to the graphene plane, while the z direction is perpendicular to the plane. The calculated lattice constant for graphene is $a = 2.463$ Å, and the unit cell height perpendicular to the graphene plane is $L_z = 15$ Å. The unit cell dimensions are kept fixed for all calculations. A $3 \times 3 \times 1$ Γ-centered grid is used to sample the Brillouin zone, and a 0.05 eV Gaussian smearing is used for the electronic occupations.

In all cases, the adatom is placed on the hollow (H) site, above the center of a hexagon formed by six C atoms. In Chapter 2 and other previous studies using the GGA, the adatom on the H site was found to have lower energy than on the bridge (B, midpoint of C-C bond) or top (T, above C atom) sites for all adatoms except for Cu [112, 169, 184].

As in Chapter 3, we assume that the main effect of applying a gate voltage to adatoms on graphene is to change the total number of electrons in the system. We therefore model gating by adding electrons to or removing electrons from the unit cell. A compensating uniform background charge is added to cancel the divergence of the total energy for charged supercells [95, 185]. The electric field of the applied gate voltage is not included, but its effects are estimated in Section 4.3.4.

The method used in this work is similar to that of Chapter 3. The main difference is that in the present chapter, for each doping level, all atomic positions are fully relaxed

---

[1] We used the pseudopotentials C.pbe-rrkjus.UPF, Co.pbe-nd-rrkjus.UPF, Ni.pbe-nd-rrkjus.UPF, Cu.pbe-d-rrkjus.UPF, and In.pbe-d-rrkjus.UPF from http://www.quantum-espresso.org. Pseudopotentials for K and Ca were generated using the Quantum-ESPRESSO package.

such that the force on each atom is less than 0.002 Ry/a.u.

4.2.2 Relation of model to experiments

We now discuss the relation of our model to experiments, expanding on several points made in Sec. 3.2. The experiment of Ref. [17] studied Co adatoms on graphene at low coverage ($\sim$ 1 Co/2000 C). At such coverages, the doping level required to ionize an adatom is within the experimentally accessible range for graphene on an SiO_2 substrate with back gate; the doping range for this setup is $\sim \pm 10^{13}$ e/cm^2. However, achieving such a low adatom coverage in supercell calculations would require a prohibitively large supercell for the graphene in-plane direction. A 6×6 supercell is computationally accessible, but calculations with such a supercell can be expected to differ in some ways from experimental studies in the low coverage limit. In the calculation, adatom-adatom interactions are not negligible, especially for charged cells. In addition, because of the high coverage, a large doping level of $\pm$ 2 e/cell, or $\sim \pm 10^{14}$ e/cm^2, is required to occupy/unoccupy adatom levels. Since there is charge transfer and doping, there are band filling errors in the supercell calculation as compared to the low coverage limit. Despite these issues, we believe that qualitative features of our calculation can give insight into experiments conducted at the low adatom coverage limit.

On the other hand, for experiments involving adatoms on graphene at higher coverages, the adatom-adatom interactions and large doping levels of the supercell calculation are physically relevant. Such large doping levels are not achievable for current experiments on graphene on SiO_2. However, doping levels as high as 4×10^{14} e/cm^2 have been achieved using an electrolytic gate [143]. Therefore, experimental observation of the DOS for the doping levels considered in this work are within the realm of possibility. However, in modeling large doping levels using supercell calculations with a uniform neutralizing background charge, electrostatic errors can be significant. Corrections for such errors are not included in the results of Section 4.3.1, but are estimated in Section 4.3.4. In summary, a quantitative comparison of supercell calculations with experiments with low adatom coverage would likely require very large supercells, but low doping levels. For comparison to experments at high adatom coverage, supercell sizes and doping levels close to that of the present calculation are appropriate, but electrostatic corrections are more important than in the low coverage case. We believe that the present computationally feasible model provides qualitative results that are relevant to experiment and useful for future theoretical studies with improved computational methods.

4.3 Results

4.3.1 Adatom alchemy within the GGA

K and Ca adatoms

We begin with the results for s valence adatoms. We find that K and Ca bind with heights of 2.57 Å and 2.34 Å above the graphene plane, respectively, in agreement with the results in Chapter 2 (Table 2.1) using slightly different ionic pseudopotentials. The adatom height is defined to be the difference in z coordinate of the adatom (z_a) and the average z coordinate of the C atoms in graphene (z_g). Figure 4.1(a) shows the PDOS for K on graphene for zero doping. A distinct peak with predominantly K 4s character lies 0.8 eV above E_F and is unoccupied. This state exhibits little hybridization with the graphene p states, and may thus be considered an atomic-like state localized on the K adatom. The graphene p PDOS is nearly unmodified below and up to 1 eV above E_F. The Dirac point E_D of graphene is clearly seen and lies 0.7 eV below E_F. This result is consistent with ionic bonding with charge transfer of the 4s valence electron of K to the graphene sheet. The net magnetization of the adatom-graphene system is zero.

Figure 4.1(f) shows the PDOS for Ca on graphene for zero doping. As in the case of K, there are distinct peaks corresponding to Ca 4s atomic-like states that do not hybridize with graphene. However, for the Ca adatom, the spin-up and spin-down Ca 4s states are split by about 1.0 eV, with the spin-up state occupied and spin-down state unoccupied. In the graphene PDOS, E_D lies 0.6 eV below E_F; above E_F the graphene states are modified by hybridization with Ca 3d states. As in the K case, the Ca adatom transfers one electron to graphene, but it retains its other 4s valence electron.

We now consider the effect of doping on the PDOS of the adatom-graphene system. Figures 4.1(b) and 4.1(c) show the PDOS for K on graphene with dopings of +1 e and +2 e, respectively (all quoted doping levels are per unit cell). At +1 e doping, the atomic-like K 4s spin-up state becomes partially occupied, and the up and down states become split in energy. At +2 e doping, the spin-up state is completely occupied, with a splitting of 0.7 eV between up and down states. The result is the ionization of the K adatom. The ionization of adatoms on graphene was studied previously in calculations for Li and Co adatoms in Chapter 3. The PDOS plots in Figs. 4.1(d) and 4.1(e) show that the Ca adatom can be similarly ionized by removal of electrons. At −1 e doping, the Ca adatom 4s state is partially unoccupied; at −2 e doping, it is completely unoccupied, with degenerate spin-up and spin-down states.

The corresponding PDOS plots in the left- and right-hand sides of Fig. 4.1 show qualitatively similar adatom levels and occupations. The K adatom with +2 e doping (Fig. 4.1(c)) has a single valence electron in the spin-up state, with the spin-down state unoccupied, just as in the case of the Ca adatom with 0 e doping (Fig. 4.1(f)). The two cases differ somewhat in the level splittings and position of peaks relative to the graphene p states. In addition, the occupied adatom state for K with +2 e doping acquires somewhat more p character than the corresponding Ca state for 0 e doping. Nevertheless, we can consider a K adatom doped with electrons to be transformed into a “quasi-Ca” adatom. Similarly, according to the calculated PDOS, the hole doped Ca adatom is transformed into “quasi-K” (Figs. 4.1(a) and 4.1(d)).

We also look at similarities in the charge densities for K and Ca adatoms with corresponding doping levels. Figure 4.2 shows total valence charge density isosurfaces for K and Ca adatoms at different doping levels. In all cases, the planar isosurface for the charge density of graphene is clearly visible, while signifcant changes are seen in the charge density near the adatom as the doping is changed. For undoped K on graphene (Fig. 4.1(a) and 4.2(a)), the localized atomic-like 4s state is unoccupied, and thus there is no valence charge density on the adatom. However, doping to +2 e occupies the spin-up K adatom state

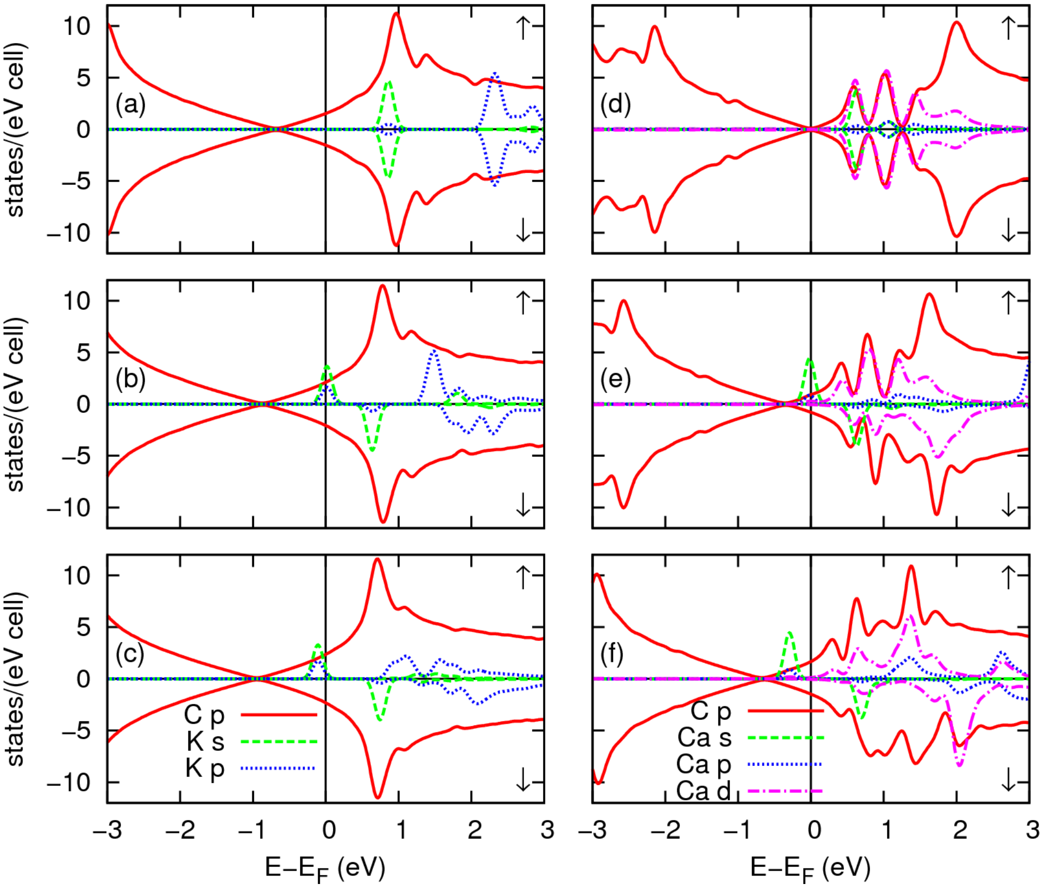

Figure 4.1: PDOS for K and Ca adatoms on graphene. Figures on the left are for K with doping levels (a) 0 e (b) +1 e (c) +2 e. Figures on the right are for Ca with doping levels (d) −2 e (e) −1 e (f) 0 e. Projections onto C $2p$ (solid red) and adatom $4s$ (dashed green), $4p$ (dotted blue), and $3d$ (dash-dotted magenta, Ca only) states are shown. Arrows indicate majority (up) and minority (down) spin channels. Energies are relative to the Fermi energy E_F.

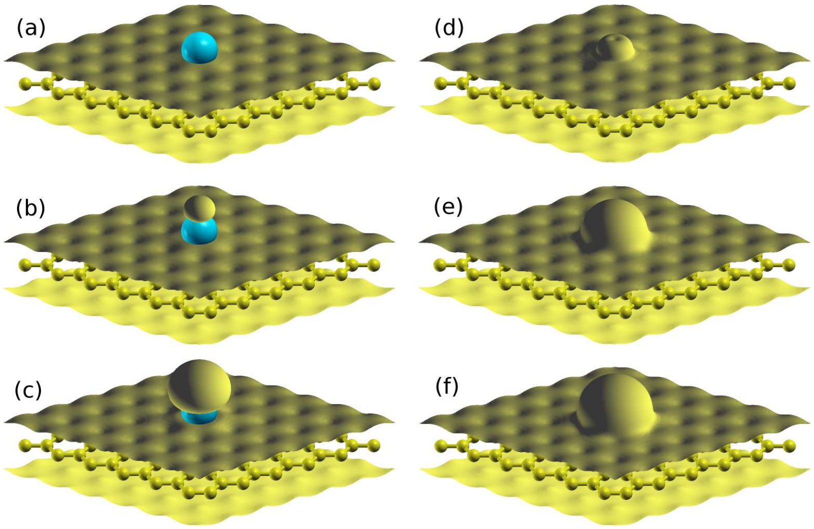

Figure 4.2: Isosurfaces of valence charge density for K and Ca adatoms on graphene. Figures on the left are for K with doping levels (a) 0 e (b) +1 e (c) +2 e. Figures on the right are for Ca with doping levels (d) −2 e (e) −1 e (f) 0 e. The isovalue is 0.001 e/a.u.^{3} for each plot.

(Fig. 4.1(c)), with corresponding increase in charge density on the adatom (Fig. 4.2(c)). This charge density isosurface plot resembles that of the Ca adatom on graphene for zero doping (Fig. 4.2(f)); in the latter case, the Ca adatom also has its spin-up atomic-like state occupied. Similarly, doping Ca on graphene to −2 e unoccupies the spin-up localized atomic-like state, reducing the charge density on the adatom (Fig. 4.2(d)) and making it similar to that of K on graphene with zero doping (Fig. 4.2(a)).

Transition metal adatoms

We now consider whether TM adatoms, possessing both d and s valence electrons, can be transformed electronically into other adatom species via gating. For 0 e doping, the calculated adsorption heights for Co, Ni, and Cu on the H site are 1.54, 1.55, and 1.94 Å, respectively, in reasonable agreement with previous results [112,169,184]. Although previous calculations report that Cu adsorption energies for the T or B sites are lower than for the H site [169,184], for comparison we find it useful to model adsorption on the H site for all three adatoms.

Figures 4.3(a) and (f) show the PDOS at zero doping for Co and Ni on graphene, repsectively. In both cases, the $3d$ states of the adatom strongly hybridize with the graphene p states, while the adatom $4s$ states hybridize weakly with graphene. For Co, the $4s$ states are unoccupied, while there is approximately one hole in the $3d$ spin-down shell, and the system is spin-polarized. For Ni, the $3d$ shell is completely occupied, the $4s$ states are unoccupied, and the system is not spin-polarized.

In order to transform Co into Ni, the ionization of Co would have to fill the $3d$ shell, while transforming Ni to Co would require partially unoccupying the $3d$ shell. According

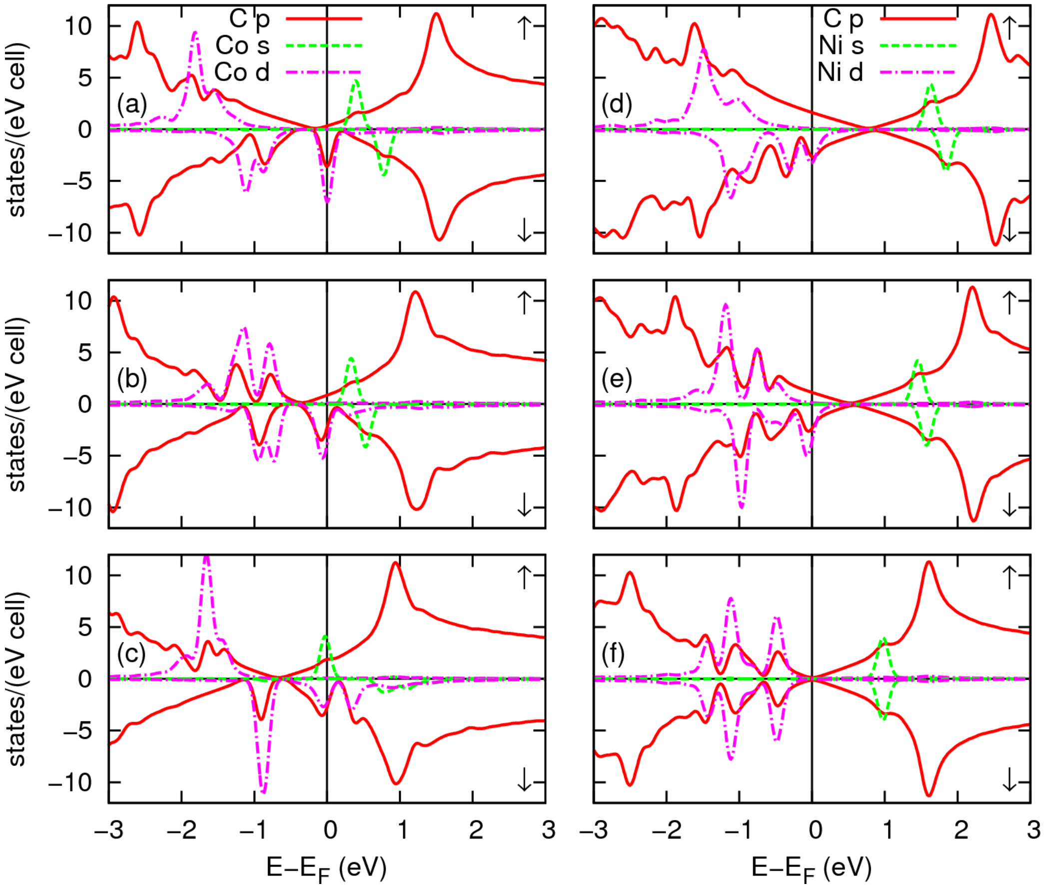

Figure 4.3: PDOS for Co and Ni adatoms on graphene. Figures on the left are for Co with doping levels (a) 0 e (b) $+1$ e (c) $+2$ e. Figures on the right are for Ni with doping levels (d) -2 e (e) -1 e (f) 0 e. Projections onto C $2p$ (solid red) and adatom $4s$ (dashed green) and $3d$ (dash-dotted magenta) states are shown. Arrows indicate majority (up) and minority (down) spin channels. Energies are relative to the Fermi energy E_F.

to our calculations, the former does not occur, but the latter does. For Ni on graphene at -2 e doping (Fig. 4.3(d)), the occupation of the $3d$ state is in fact decreased, such that its electronic structure resembles that of undoped Co. As in the case of K and Ca, the relative positions of the atomic d and s states and graphene differ between neutral Co on graphene and doped Ni on graphene, but the ordering and occupations of the s- and d-derived adatom states are qualitatively similar. On the other hand, the Co $4s$ states lie close to E_F for the undoped system, so that when electrons are added, the occupations of both the Co $4s$ and $3d$ states are increased. At $+2e$ doping, the Co $4s$ and $3d$ states are partially occupied and lie at E_F, which is different from the case of the undoped Ni adatom.

While the transformation of Co to quasi-Ni upon doping does not occur in our calculations, we find that it is possible to transform Ni to quasi-Cu, and vice versa. Figure 4.4 shows the PDOS for various dopings for Ni and Cu. The $3d$ states lie far enough below

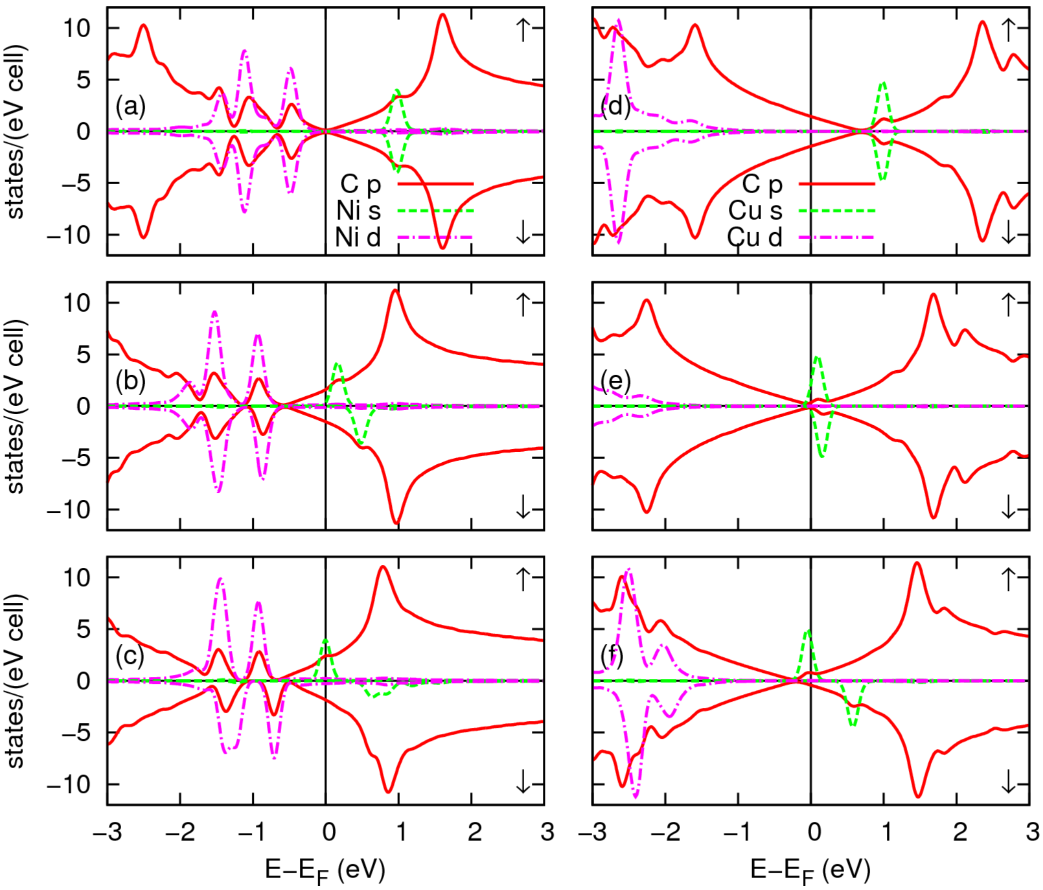

Figure 4.4: PDOS for Ni and Cu adatoms on graphene. Figures on the left are for Ni with doping levels (a) 0 e (b) +1 e (c) +2 e. Figures on the right are for Cu with doping levels (d) −2 e (e) −1 e (f) 0 e. Projections onto C $2p$ (solid red) and adatom $4s$ (dashed green) and $3d$ (dash-dotted magenta) states are shown. Arrows indicate majority (up) and minority (down) spin channels. Energies are relative to the Fermi energy E_F.

E_F that their occupation is unchanged by doping. Instead, the occupation of the $4s$ spin-up states is varied by doping. In fact, tranformations between Ni and Cu are analogous to those between K and Ca, a main difference being that the $3d$ states are completely occupied in the TM case and completely unoccupied for the alkali/alkaline case.

In adatom

In addition to changing the occupation of s- and d-like adatom states by gating, it is also possible to change the occupation of p-like adatom states. For an In adatom on graphene at zero doping, the In $5p$ states hybridize with graphene and are somewhat broadened (Fig. 4.5(a)). The main peak lies 0.4 eV above E_F; these atomic-like states are spin-degnerate and unoccupied. Upon increasing the doping to +2 e (Fig. 4.5(c)), the spin-up $5p$ states become partially occupied, and the up and down states split in energy

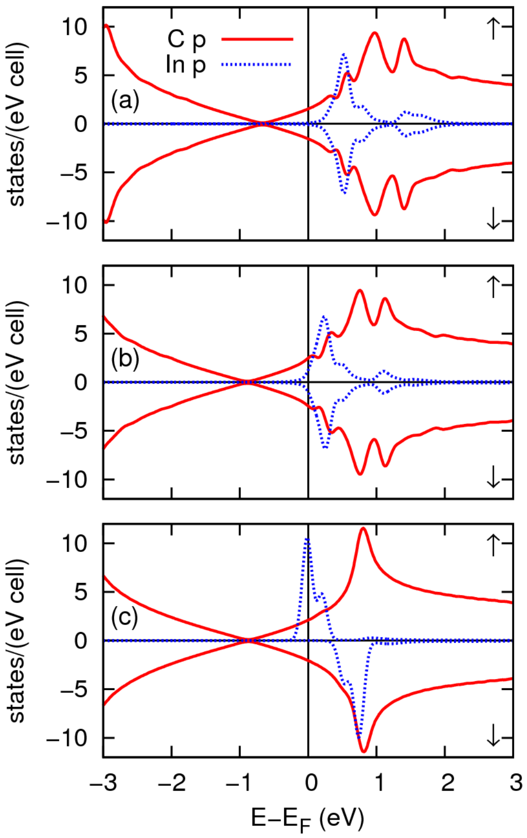

Figure 4.5: PDOS for an In adatom on graphene with doping levels (a) 0 e (b) +1 e (c) +2 e. Projections onto C $2p$ (solid red) and adatom $5p$ (dotted blue) states are shown (adatom $5s$ and $4d$ states lie outside the energy window). Arrows indicate majority (up) and minority (down) spin channels. Energies are relative to the Fermi energy E_F.

in a manner similar to that of the s states of a doped K adatom. However, one should take note of the large change in In adatom height for +2 e doping, as discussed in Section 4.3.2. Because of this large change in height, the adatom and graphene states are almost completely decoupled (Fig. 4.5(c)).

4.3.2 Effect of gating on atomic positions

In this section we discuss the effect that gating has on the positions of the graphene C atoms and the adatom. To quantify the displacement of C atoms from their position in pristine graphene, we define (as in Sec. 2.3.1) the distortion to be the maximum absolute difference between any C atom z coordinate and the average z coordinate of all the C atoms in the graphene. For the undoped case, we find that the distortion is less than 0.01 Å for all the adatoms considered, consistent with the results of Chapter 2 for adatoms on the H site of graphene. With doping, the maximum distortion is less than 0.025 Å.

We do find changes in the position of the adatom relative to graphene as a function

Table 4.1: Heights of adatoms above graphene sheet for different doping levels considered in this work. The +/− signs in the adatom species headings denote addition/removal of electrons, with the doping amount indicated by the corresponding column under the "doping" heading.

Doping (e)		Height (Å)						
+	−	K (+)	Ca (−)	Co (+)	Ni (−)	Ni (+)	Cu (−)	In (+)
0	−2	2.57	2.19	1.54	1.61	1.55	1.82	2.51
+1	−1	2.58	2.27	1.48	1.58	1.57	1.81	2.50
+2	0	2.68	2.34	1.60	1.55	1.63	1.94	3.60

of doping. The adatom heights for the different doping levels considered in this work are presented in Table 4.1. For most adatoms, the changes in height are about 0.1-0.2 Å; In is an exception.

An explanation for the trends in adatom height is suggested by the changes in occupation of adatom electronic levels as seen in the PDOS. For both K and Ca, an increase in adatom height correlates with an increase in the occupation of the adatom s orbital. A similar correlation holds for Ni when the doping is increased from 0 to +2 e and for Cu when the doping of is increased from −2 to 0 e. On the other hand, for Ni, an increase in adatom height is correlated with a decrease in occupation of adatom d states when going from 0 to −2 e doping. The case of Co is at first glance unusual, but it also follows the same trends. When the doping level is increased from 0 to +1 e, the occupation of Co d states is increased, and the adatom height decreases. Increasing the doping level from +1 to +2 e increases the occupation of the Co s state, and the adatom height increases.

We explain the correlation between adatom heights and occupancies of s or d states as follows. Adatom s states do not hybridize strongly with the C p states of graphene. When the occupation of the adatom s state is increased, the radius of the electronic cloud of the adatom is increased, pushing the adatom away from the graphene. On the other hand, adatom d states do hybridize strongly with C p states, forming covalent bonds. Increasing the occupation of adatom d states strengthens the bond between the adatom and graphene and decreases the adatom height.

For In, the adatom height is increased by more than 1 Å when the doping is increased from +1 to +2 e. This result indicates that the binding of In is signifcantly weakened by this increase in doping. For In on graphene with zero doping, the binding has large ionic character, as indicated by the charge transfer from In to graphene, which leaves the In adatom positively charged. When the doping is increased to +2 e, In p states become filled, and the In adatom is no longer positively charged but rather close to neutral. Therefore the ionic bonding is significantly weakened.

A similar effect may happen for K. From 0 to +2 e doping, the K height is only increased by 0.11 Å, but for larger dopings the adatom height could increase and the binding could weaken even more. A more complete analysis of possible desorption of adatoms due to gating would be interesting but would need to take into account electrostatic errors in the potential and total energy for the supercell calculation with uniform neutralizing background.

We remark on the importance of relaxation of the atomic coordinates in the PDOS for gated adatoms. As a test, we calculate the PDOS for gated adatoms on graphene in which the C atoms are fixed to their positions in ideal, flat, two-dimensional graphene and the adatom height fixed to the optimized height for the undoped system, as in Chapter 3. We then compare these calculations to the calculations presented in Section 4.3.1 for fully relaxed structures. Little qualitative difference is seen in most cases; the few noticeable differences can be explained by the change in adatom height. For example, in the calculation for the In adatom at $+2\ e$ doping with adatom height fixed to the optimized height for zero doping, there is adatom-graphene hybridization, but in the fully relaxed calculation, the hybridization is greatly reduced due to the increased adatom height. For all adatoms, the effect of the C lattice distortion on the PDOS is small, which is reasonable given the small amount of distortion. We conclude that the main effect of the atomic relaxation is the change in adatom height. It is noted that the C lattice distortion may be more important for adatoms bound to the B or T sites.

4.3.3 Effect of Hubbard U

In this section, the effect of correlation in the $3d$ shell of TM adatoms, as modeled by the LDA+U method, is discussed. For Co on graphene, we find that for U=4 eV and a doping of 0 e, the T site is favored over the H site when all atoms are fully relaxed, in agreement with previous studies [162]. Furthermore, in Chapter 3, it was shown that for Co on the H site and U=2 or 4 eV, the DOS is changed qualitatively; a $4s$ rather than a $3d$ Co adatom state lies at E_F. Doping changes the occupation of the $4s$ state, in contrast to the U=0 eV case, for which the doping changes the $3d$ occupations. Since the results depend on the value of U, some doubt is cast on the U=0 eV result that Ni can be transformed into quasi-Co. It would be useful but beyond the scope of this study to determine whether a U of several eV or close to 0 eV is more appropriate to describe Co on graphene.

For Ni and Cu on graphene, we performed calculations for a doping of 0 e and U=4 eV. In both cases, the favored adsorption site was unchanged from the U=0 eV case (H for Ni and B for Cu). Furthermore, the DOS was qualitatively unchanged; the adatom $3d$ shell is completely filled (closed), and the $4s$ state is above (for Ni) or at (for Cu) E_F. We therefore expect that the results for doping of Ni or Cu on graphene will not be affected signifcantly by a U parameter that lies within this range.

4.3.4 Estimate of electrostatic errors in supercell calculations with uniform background charge

The use of periodic supercells to model charged systems can lead to unphysical effects that should be accounted for in calculations. In this section, we describe our method of estimating these effects and discuss the implication of these effects on our results for the PDOS and atomic positions.

Method of estimation

An infinite lattice of periodically repeated charged supercells has a divergent total energy per unit cell. To get a finite total energy, a compensating charge must be added to the cell to make it neutral. For the calculations in this chapter, a uniform compensating charge is employed [95,185]. Such an approach is commonly used as it is automatically implemented in many plane-wave pseudopotential approaches [27]. However, the compensating charge is unphysical and can affect the electrostatic potential and total energy. Furthermore, the unphysical interaction between neutral periodic supercell images can also be significant.

In this section, we determine a correction to the electrostatic potential and use this correction to estimate the effects on our results for the PDOS and atomic positions. We build upon the approach of Ref. [186] for charged slabs and additionally include dipole corrections.

As in Ref. [186], let ρ denote the charge density of the slab (in the present case, a graphene plane with adatoms) and $\tilde{\rho}$ denote the slab plus background charge density ρ_b:

$$\tilde{\rho}(\vec{r}) = \rho(\vec{r}) + \rho_b(\vec{r}), \tag{4.1}$$

where in the present case $\rho_b(\vec{r}) = -\langle\rho(\vec{r})\rangle$ is uniform (the angled brackets denote the average over the unit cell). Similarly, let V denote the electrostatic potential of the slab, $\widetilde{V}$ denote the electrostatic potential of the slab plus background charge density in periodic boundary conditions, and V_b denote the potential of the background charge:

$$\widetilde{V}(\vec{r}) = V(\vec{r}) + V_b(\vec{r}). \tag{4.2}$$

In analogy with the method of Ref. [187], let us define the corrective potential as

$$V_{\text{corr}}(\vec{r}) = V(\vec{r}) - \widetilde{V}(\vec{r}), \tag{4.3}$$

so that $V_{\text{corr}}(\vec{r}) = -V_b(\vec{r})$. Then Poisson's equation for the corrective potential is

$$\nabla^2 V_{\text{corr}}(\vec{r}) = 4\pi\rho_b(\vec{r}). \tag{4.4}$$

We obtain the corrective potential by solving this equation with appropriate boundary conditions.

The potential $\widetilde{V}$ and charge density $\tilde{\rho}$ are solved for self-consistently using standard PWPP DFT methods. The corrective potential V_{corr} is added *a posteriori* to $\widetilde{V}$ to get the potential V of the slab in vacuum without any background charge. Therefore, the charge density $\tilde{\rho}$ and potential V are not consistent with each other. Some change in the charge density is expected if it is solved for self-consistently in the corrected potential V; the effects of this change in charge density on the PDOS and forces are expected to be small and are neglected.

In order to solve Poisson's equation for the corrective potential, we make a planar-average approximation [188] in which we assume that the corrective potential is uniform in the x-y plane and only varies in the z direction perpendicular to the graphene plane. Under this approximation, Poisson's equation is one-dimensional and can be solved if the boundary conditions are specified.

For a charged system with two-dimensional periodicity, such as a charged slab, the boundary conditions require some consideration. The potential of a uniformly charged infinite 2D plane relative to a point infinitely far away from it is infinite, so the zero of the potential energy cannot be defined as the vacuum level, as is often done for zero-dimensional charged systems. This issue can be dealt with by specifying a reference electrode [186], a plane at a specified distance from the slab whose potential is defined to be zero. This distance should be large enough to ensure that the plane lies in a region of vacuum where the potential as a function of z is linear.

In addition to choosing the position of the reference electrode, the slope of the potential at the reference electrode must also be specified. In the present work, we consider two possible boundary conditions. Boundary condition 1 (BC1) is specified such that the electric fields far in the vacuum region on either side of the slab are equal in magnitude but opposite in sign. Such a boundary condition could be obtained in experiment with both back and top gates and appropriately tuned potential differences. For boundary condition 2 (BC2), the electric field is zero far in the vacuum region on the adatom side of the slab. The BC2 is relevant for experiments with a single back gate. The back gate electrode contains an equal and opposite sign charge per unit area as the charged slab. For BC2, as for a parallel plate capacitor, a finite electric field exists in the region between the back gate electrode and the charged slab, and zero electric field exists in the vacuum region on the side of the slab facing away from the back gate.

With the boundary conditions specified, we solve for the corrective potential V_{corr}. Following Ref. [186], let q denote the net charge of the unit cell ($q > 0$ for excess electrons), A_0 the unit cell area in the graphene plane, z_0 a chosen origin, Λ the distance between the reference electrode and the origin ($\Lambda > 0$), L_z the length of the unit cell in the z direction, and p the dipole moment per unit cell in the z direction:

$$p = \int_{\text{cell}} \rho(\vec{r}) z d\vec{r}. \tag{4.5}$$

For an origin chosen such that the dipole moment is zero, the corrective potential for BC1 was given in Ref. [186]. We use V_{mon} to denote this “monopole” potential:

$$V_{\text{mon}}(z) = \frac{2\pi q}{A_0} \left[\frac{(z - z_0)^2 - L_z \Lambda + (L_z/2)^2}{L_z} \right]. \tag{4.6}$$

If the dipole moment is not zero, we add to V_{mon} a dipole potential [96, 158]:

$$V_{\text{dip}}(z) = -\frac{4\pi p}{A_0} \frac{z - z_0}{L_z}, \tag{4.7}$$

so the corrective potential is given by

$$V_{\text{corr}} = V_{\text{mon}} + V_{\text{dip}}. \tag{4.8}$$

The origin should be chosen such that $z_0 \pm L_z$ lies in the vacuum region, but aside from this criterion the precise choice does not affect the corrective potential. For any shift in the origin, the change in V_{mon} will be compensated for, aside from an overall constant, by a change in V_{dip} via a change in p. The overall constant is not important for the estimates given in the present work, but would be important if one needed to determine total energy differences for charged slabs. Likewise, the choice of reference electrode position is not particularly important in this work, so long as it lies in the vacuum region where the potential is linear.

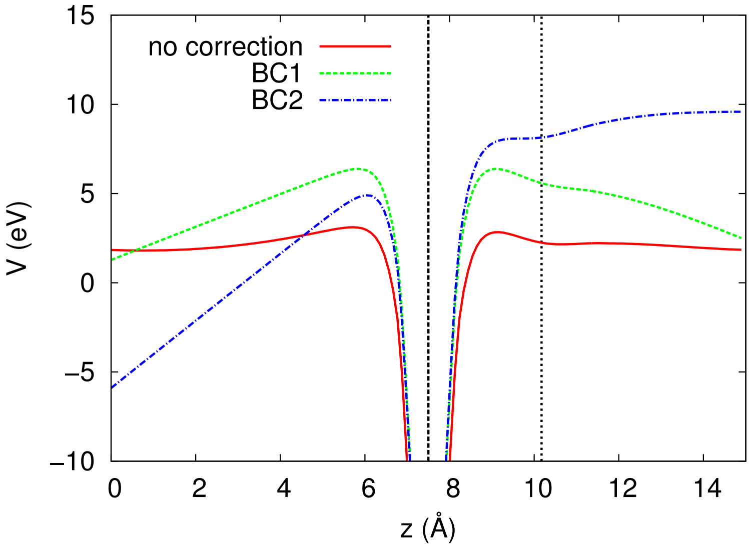

Figure 4.6: Planar-averaged uncorrected electrostatic potential (solid red) and corrected potentials for boundary condition 1 (dashed green) and boundary condition 2 (dash-dotted blue) for K on graphene with doping level of $+2\ e/\text{cell}$. The vertical dashed and dotted black lines denote the graphene and adatom z positions, respectively.

The potential for BC2 can be obtained from the potential for BC1 by adding a linear potential, equivalent to adding a constant electric field perpendicular to the graphene plane:

$$V_{\text{corr}} = V_{\text{mon}} + V_{\text{dip}} + V_{\text{efield}}, \tag{4.9}$$

with

$$V_{\text{efield}} = \frac{2\pi q}{A_0}(z - z_0). \tag{4.10}$$

As an example, the planar-averaged uncorrected electrostatic potential and corrected potentials for BC1 and BC2 for K on graphene with a doping level of $q = +2e$ are plotted in Fig. 4.6. The origin is chosen to be at 7.5 Å, near the position of the graphene plane. The reference electrode is chosen to be at 0 Å, so that $\Lambda = 7.5$ Å. For the 6×6 unit cell, $A_0 = 189.09$ Å^2, and $L_z = 15$ Å. The dipole moment is calculated to be $p = 3.45$ eÅ. As expected, the potential becomes linear at the edges of the unit cell for the corrected potentials; for BC1, the magnitudes of the slopes on either side of the graphene plane are equal, while for BC2, the slope is zero on the adatom side of the graphene plane.

After computing the corrective potential V_{corr}, we can estimate the effect of this potential on the PDOS and atomic positions. For the PDOS, we might expect the potential to shift the positions of the adatom states relative to the graphene states. For a rough estimate of this shift, we assume that the graphene states lie at the position of the graphene plane z_g, while the adatom states lie at the position of the adatom z_a. In reality these states have some z distribution, but our simple assumption gives a reasonable estimate. The estimate for the relative energy shift is given by $\Delta\epsilon = V_{\text{corr}}(z_a) - V_{\text{corr}}(z_g)$.

For the atomic positions, we estimate the force on the adatom, $F^a_{\rm corr}$, and the graphene plane, $F^g_{\rm corr}$, due to $V_{\rm corr}$. We have

$$F^a_{\rm corr} = -Q_a \frac{d}{dz} V_{\rm corr}(z)|_{z=z_a}, \tag{4.11}$$

and similarly for $F^g_{\rm corr}$. To estimate the net charge Q_a of the adatom we take the difference of the Löwdin electron charge [189] and the ion core charge. The same is done for the C atoms and then averaged over all the atoms in graphene to get the net charge Q_g. The force on the graphene plane turns out to be small in comparison to the force on the adatom, so $F^g_{\rm corr}$ can be neglected in our estimates. The force can be translated into a change in the adatom height above the graphene sheet by assuming a harmonic potential of a given curvature between the adatom and graphene. We neglect the additional change in PDOS that this change in adatom position would cause.

Estimation results

For BC1, we find that $|\Delta\epsilon| < 0.1$ eV for most adatoms and doping levels. One exception is K, for which $\Delta\epsilon \sim -0.3$ eV. Also, in the case of In, $\Delta\epsilon \sim -0.5$ eV for $q = +2e$; the large shift is related to the large adatom height of 3.60 Å. Although these shifts in the PDOS might change the precise values of the doping levels at which states are occupied or unoccupied, they do not appear large enough to change qualitatively our main results concerning adatom alchemy.

As for the forces under BC1, in all cases, $|F^a_{\rm corr}| < 0.2$ eV/Å. As a rough estimate, assuming an out-of-plane adatom vibration mode energy of ~ 10 meV (Ref. [17]) and using an atomic mass of ~ 40 (for K), a force of 0.2 eV/Å gives a displacement of ~ 0.2 Å.

From these estimates, we can conclude that our model consisting of a charged adatom on graphene in a periodic supercell with neutralizing background gives qualitatively reasonable results for the physical system with BC1. Electrostatic corrections at least to dipole order should be included to get quantitative results to ~ 0.1 Å precision in adatom position and ~ 0.1 eV precision in the PDOS.

The applied electric field which provides the difference in potential between BC1 and BC2 is close to 1 eV/Å for a doping level of $\pm$ 2 e. Such a large electric field leads to estimates of $|\Delta\epsilon| \sim 1$ eV for DOS energy shifts and $|F^a_{\rm corr}| \sim 1$ eV/Å for force corrections. Therefore, the model used in the present calculations is not adequate for a system with BC2 at these doping levels; explicit inclusion of the electric field is important and has a signifcantly larger effect than the inclusion of potentials $V_{\rm mon}$ and $V_{\rm dip}$.

Despite this difference, our results still have relevance for experiments for gated adatoms on graphene in which both the adatom coverage and the doping level are significantly reduced (by an order of magnitude). In such cases, the electric field due to the back gate is reduced in proportion to the doping level, and the corrections are smaller. As noted in Section 4.2.2, the different adatom coverage between our calculation and such experiments should be taken into account when comparing the two.

We mention several references that have addressed aspects of charged supercell calculations relevant to the present work. A monopole and dipole potential correction similar to the one given here and implemented self-consistently is described in Ref. [159].

A more general scheme to compute the full corrective potential for a charged system in uniform neutralizing background is given in Ref. [187]. A Green's function approach for charged slabs that can include an "effective screening medium" is detailed in Ref. [190]. A somewhat different approach to dealing with charged supercells is to explicitly model a countercharge of computationally advantageous shape [191–193]. Several studies have applied this approach to charged slab geometries [194–201].

4.4 Conclusion

The controlled "alchemy" of adatoms, as explored in this work, could have significant applications. Many chemical reactions rely on TM catalysts, which may be difficult to control. One could imagine transforming, via gating, adatoms which are easier to deal with experimentally but less useful chemically into other adatoms that can catalyze important reactions. We have investigated this tranformation for certain adatoms, but it may be possible for other species as well; this possibility warrants future study. Graphene coated with Ca or TM adatoms is also a possible material for hydrogen storage [202]. Gating such adatom-graphene materials might allow for controlled adsorption/desorption of hydrogen.

In summary, the gate-controlled alchemy of adatoms on graphene is explored using first-principles density-functional supercell calculations with the GGA. Transformations between K and Ca, between Ni and Cu, and of Ni to Co are demonstrated. The gating of In adatoms is also studied. Changes in adatom height with gating are explained by comparison with the PDOS. The inclusion of a Hubbard U to model correlation in $3d$ states of adatoms can have a significant effect on the results. Also, electrostatic corrections to the supercell approximation with uniform background charge are important for obtaining quantitative results for large amounts of doping. We therefore caution against interpreting our results as definitive predictions of adatom alchemy. Nevertheless, we hope that this work will stimulate further theoretical and experimental study of the phenomenon of adatom alchemy on graphene via application of gate voltage.

Chapter 5

Ab initio calculations of phonon splitting in antiferromagnetic $ZnCr_2O_4$

The full zone-center optical phonon spectrum and the exchange coupling constant J of the uniform collinear antiferromagnetic (AFM) ordered phase of $ZnCr_2O_4$ are calculated within density-functional theory using the local spin density approximation (LSDA), the LSDA plus Hubbard U (LSDA+U), and the spin-polarized generalized gradient approximation (σ-GGA). The AFM ordering is found to induce splittings in the infrared active phonon modes, confirming the importance of spin-phonon coupling in $ZnCr_2O_4$. The σ-GGA and the LSDA+U give magnitudes of phonon frequencies close to experiment, while the LSDA frequencies are slightly softer. However, only the LSDA+U exchange constant and phonon splittings are consistent with experiment and previous calculations. A correspondence between the exchange constant and the splittings for the infrared active phonon modes is found. The work presented in this chapter has been published in Ref. [203].

5.1 Introduction

Spin-lattice coupling has implications for phase transitions and phonon spectra for a wide variety of correlated electron materials, including magnetic insulators [204] and metals [205], frustrated magnetic systems [206], and multiferroics [207]. Zinc chromite ($ZnCr_2O_4$) provides an experimentally realizable correlated electron system for studying this coupling. It forms a normal cubic spinel crystal structure [208] in which the Cr^{3+} ions form a sublattice of vertex sharing tetrahedra, the pyrochlore lattice.

The cubic crystal field splits the d orbitals of Cr^{3+} into three occupied t_{2g} orbitals and two unoccupied e_g orbitals. The three electrons occupying the t_{2g} orbitals have parallel spins, giving the Cr^{3+} ions a total spin of $S = 3/2$. Between neighboring Cr^{3+} ions, both antiferromagnetic (AFM) direct exchange, from the overlap of the t_{2g} orbitals which are directed towards the nearest neigbors, and ferromagnetic (FM) superexchange, via Cr-O-Cr bonds, are present [209, 210]. The overlap of orbitals of nearest neighbor Cr^{3+} ions is such that direct exchange is much stronger than superexchange, and the overall interaction is antiferromagnetic. Further neighbor interactions between Cr^{3+} ions are much smaller and can be neglected. Hence we can model the magnetic interactions using a Heisenberg hamiltonian,

$$H = J \sum_{i,j} \vec{S}_i \cdot \vec{S}_j, \tag{5.1}$$

where J is the exchange coupling constant, and the sum is over all nearest neighbor pairs. From paramagnetic susceptibility measurements, the Curie-Weiss temperature $\Theta_{CW} = -390$ K, which gives $J = 4.5$ meV [211]. Thus $ZnCr_2O_4$ is a physical example of a pyrochlore antiferromagnet.

The ideal pyrochlore AFM is a well known frustrated system, with the classical Heisenberg system failing to order down to zero temperature [212]. Indeed, $ZnCr_2O_4$ achieves AFM order only at a Néel temperature $T_N = 12.5$ K; such a low T_N relative to $|\Theta_{CW}|$ is a signature of frustration. Inelastic magnetic neutron scattering experiments have shown that spin-lattice coupling can play a crucial role in the relief of frustration and a transition to an AFM ground state with a Jahn-Teller like distortion of the lattice [211].

Furthermore, the recent observation of a phonon splitting below T_N in an infrared (IR) active zone-center phonon mode has been attributed to spin-phonon coupling [213]. Phonon frequencies have been calculated for many materials using total energy approaches and density functional theory (DFT) with great success [28]. Within DFT, the local (Spin) density approximation [L(S)DA] has been widely used. In $ZnCr_2O_4$, the presence of d electrons localized on the magnetic Cr^{3+} ions suggest that electron correlation effects are important in this material. By the addition of a Hubbard-like U term to the LSDA, the LSDA+U method [59] attempts to capture effects of correlation. However, it is not immediately clear how important electron correlation is in determining the properties of zinc chromite, and in particular the phonon frequencies and the magnetic-induced phonon splitting. A recent first principles LSDA+U calculation used a value of $U = 3.0$ eV [214], which is relatively small compared to other correlated electron systems [54]. Additionally, in CrO_2, Toropova et al [215]. found that the LSDA accounts for experimental data better than the LSDA+U. We explore these approaches, and we also consider the (spin-polarized) Generalized Gradient Approximation [(σ-)GGA], which has been shown to give better agreement with experiment than the L(S)DA for some systems [216, 217].

In this chapter we present results of LSDA, LSDA+U, and σ-GGA calculations of zone-center phonon frequencies for the uniform (zero-wavevector) ordered collinear AFM phase of $ZnCr_2O_4$. Our LSDA+U results are in agreement with the previous *ab initio* calculation [214]. Calculations of the exchange constant J and insulating band gap provide additional insight into the origin of the phonon splitting of $ZnCr_2O_4$. We find that phonon frequency magnitudes can be described reasonably well using the σ-GGA and are slightly softer for the LSDA. However, only with the LSDA+U method are the exchange constant and phonon splittings in agreement with experiment.

5.2 Computational Details

Our LSDA [23, 24], σ-GGA [26], and LSDA+U [60] calculations are performed using the plane-wave pseudopotential method, as implemented in the Parallel Total Energy

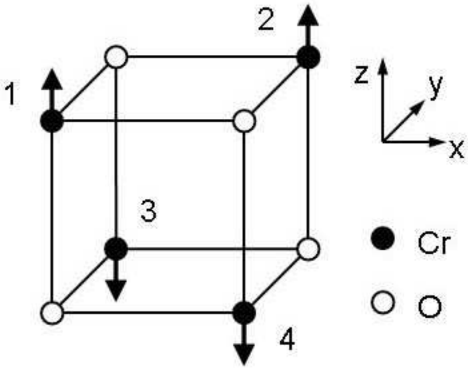

Figure 5.1: Collinear AFM order for a Cr^{3+} tetrahedron in $ZnCr_2O_4$. The full unit cell is not shown. Arrows indicate spins.

Code (PARATEC) [218,219], with Troullier-Martins norm-conserving pseudopotentials [38] and a plane-wave cutoff of 250 Ry. For the Brillouin zone sampling, a $3 \times 3 \times 3$ Monkhorst-Pack k-point grid [220] with an offset of $0.5 \times 0.5 \times 0.5$ is used. For the Cr^{3+} d electrons in LSDA+U, $U = 3.0$ eV and $j = 0.60$ eV are used for the Coulomb and exchange parameters, respectively. The same value of U was used in previous LSDA+U calculations for $ZnCr_2O_4$ (Ref. [214]) and CrO_2 (Refs. [215, 221]) and reproduced features in photoemission data in other Cr^{3+} spinels [222].

5.2.1 Structure

The cubic spinel structure is characterized by two parameters: the lattice constant a and the anion parameter u, which governs oxygen ion positions within the Zn-Cr lattice. For the calculation of the exchange constant J, we use the experimental paramagnetic (PM) cubic structure $a = 8.327$ Å and $u = 0.386$ [223].

The bandstructure and phonon calculations are performed for uniform AFM ordering with collinear spins (Fig. 5.1). We fully relax the forces on the atoms but keep the PM lattice constant. The Zn^{2+} and Cr^{3+} ions remain in their ideal positions in cubic spinel, while the relaxed oxygen ions reduce the structural symmetry from cubic to tetragonal, consistent with the AFM ordering. Note that experimentally the tetragonal distortion is of the whole lattice, not just the oxygen atoms. Our relaxed oxygen coordinates deviate only a small amount from cubic symmetry and are close to the coordinates of the experimental PM phase and previous calculations.

5.2.2 Phonons

We calculate the full set of 39 optical and 3 acoustic zone-center phonons by diagonalizing a 42×42 dynamical matrix, which is obtained using the frozen phonon approach. From group theory, the zone-center phonons of cubic $ZnCr_2O_4$ (point group O_h) transform according to the following irreducible representations (irreps) [224]:

$$\Gamma = A_{1g} + E_g + T_{1g} + 3T_{2g} + 2A_{2u} + 2E_u + 4T_{1u} + 2T_{2u}.$$

In a symmetry coordinate basis, the dynamical matrix can be put into block diagonal form. For each irrep, the number of degenerate irreducible subblocks equals the dimension of the irrep, and these subblocks do not mix. We use the symmetry coordinates and notation given in Ref. [224].

When collinear AFM ordering is introduced, the symmetry of the system is reduced to tetragonal (point group D_{4h}), and each triply degenerate T mode splits into a doublet and a singlet, while each doubly degenerate E mode also splits. The mixing of subblocks belonging to different irreps of cubic $\mathrm{ZnCr_2O_4}$ symmetry is small and can be neglected, as explained in the following.

Although the system has tetragonal symmetry, the frequencies we obtain by diagonalizing the full dynamical matrix show all degeneracies split, due to the use of finite displacements in the frozen phonon approach for calculating forces. A second set of frequencies is obtained by diagonalizing only within the irreducible subblocks according to the cubic irreps, setting to zero any off-block-diagonal elements that give mixing between irreps. The resulting frequencies give the expected twofold degeneracies in the T phonon modes. Compared with diagonalization of the full dynamical matrix, the subblock diagonalization changes the frequencies by only a small amount. The results presented in this work are those obtained from the subblock diagonalization.

5.3 Results

5.3.1 Ground State Properties

Each of the LSDA, LSDA+U, and σ-GGA methods gives an insulating ground state. The bands near the band gap are predominantly of Cr d orbital character. The band gaps are of the same order; however, the gap increases from the LSDA (1.0 eV), to the σ-GGA (1.5 eV), to the LSDA+U (2.2 eV). The LSDA+U gap is larger than that of the LSDA, as expected [54], since the Hubbard U term pushes occupied and unoccupied d bands farther apart in energy.

We also calculate the exchange constant J. Let E_0 be the total energy per unit cell excluding the magnetic contribution; the unit cell contains four Cr^{3+} ions (two formula units), and each Cr^{3+} ion has six nearest neighbors. From the Heisenberg hamiltonian, the total energy per unit cell of the collinear AFM phase is $E_{\mathrm{AFM}} = E_0 - 4JS^2$, and that of the collinear uniform FM phase for the same structure is $E_{\mathrm{FM}} = E_0 + 12JS^2$. The difference in energy is $16JS^2$, from which we calculate J. The values are listed in Table 5.1. Only the LSDA+U result compares well with the previous first principles LSDA+U calculation (4.2 meV, Ref. [214]) and experiment (4.5 meV, Ref. [211]), while the LSDA and σ-GGA results are not in agreement. The exchange constant J is somewhat sensitive to the U parameter, and the agreement of our calculation of J with experiment helps to justify the choice of U.

5.3.2 Phonons

The experimentally accessible modes are the five Raman active modes, A_{1g}, E_g, and $3T_{2g}$, and the four IR active modes, $4T_{1u}$. Our calculated Raman and IR phonon frequencies are listed in Tables 5.2 and 5.3, along with previous LSDA+U results. Also

Table 5.1: Calculated and experimental exchange constant J and spin-phonon coupling constant λ_3 of the $T_{1u}(3)$ mode.

	J (meV)	λ_3 (cm^{-1})
LSDA	9.1	20
σ-GGA	7.1	15
LSDA+U	4.3	12
Experiment (Ref. [213])	4.5	6-10

given are experimental results for Raman modes in the paramagnetic phase [224], and IR modes both above and below T_N [213]. The remaining optical modes are given in Table 5.4. Under the reduction to tetragonal symmetry induced by the collinear AFM ordering, let the $\hat{z}$ direction be the tetragonal axis. The T modes split into a doublet and a singlet; the doublet modes transform as vectors perpendicular to the tetragonal axis, which we may take as $\hat{x}$ and $\hat{y}$, while the singlet transforms as the vector $\hat{z}$. In our notation, the doublet is labeled by $\hat{x}$, and the singlet by $\hat{z}$. The split E modes are labeled by a and b. The splitting for any mode is labeled by Δ. The splittings are not directly comparable to experiment, since our calculations are done for the uniform collinear AFM phase, while the experimental sample in the AFM phase shows nonuniform ordering.

We now compare the magnitudes of the calculated phonon frequencies. The LSDA calculation gives softer phonons than the σ-GGA and LSDA+U calculations by $\sim 5\%$ [the $T_{1u}(4)\hat{x}$ mode is an exception]. These relative magnitudes of the LSDA and σ-GGA results are consistent with previous results for other materials, both non-spin- [217] and spin-polarized [216, 225]. We emphasize that our calculations for all methods use the same value of the lattice constant. In the case of silicon, harder phonons in the GGA are consistent with reduced electron screening [226]. The increased band gap for the σ-GGA and the LSDA+U relative to the LSDA suggests that a similar effect occurs in $ZnCr_2O_4$.

Our LSDA+U calculations are consistent with those of Fennie and Rabe [214]. For the most part, our phonon frequencies are slightly softer, as might be expected for our use of a slightly larger lattice constant (8.33 Å versus 8.26 Å).

The fact that the LSDA frequencies are not far from the LSDA+U frequencies is perhaps surprising. For example, we compare $ZnCr_2O_4$ to the magnetic oxide MnO in the AFM ordered phase, for which the LSDA gives transverse optical phonon frequencies of 101 and ~ 0 cm^{-1} [204], while the LSDA+U gives frequencies close to the experimental values of 268 and 293 cm^{-1} [227]. The failure of the LSDA to give reasonable phonons and the relatively large value of $U = 6.9$ eV necessary for the LSDA+U calculations to reproduce the experimental phonon frequencies are evidence for this strong correlation. In $ZnCr_2O_4$, the LSDA reproduces the insulating AFM phase and gives reasonable values for the phonon frequencies; this result and the smaller value of $U = 3.0$ eV reflects the reduced importance of electron correlation in $ZnCr_2O_4$, as compared with some other magnetic oxides.

Furthermore, our calculations show that the σ-GGA gives phonon frequencies very close in magnitude to the LSDA+U frequencies. The phonon and band gap calculations demonstrate that the σ-GGA, more so than the LSDA, accounts for many of the properties of $ZnCr_2O_4$ without explicit inclusion of a U correlation term in the exchange-correlation functional.

Table 5.2: Calculated and experimental frequencies for Raman active modes, in cm^{-1}.

	A_{1g}	E_g			$T_{2g}(1)$			$T_{2g}(2)$			$T_{2g}(3)$		
		a	b	Δ	$\hat{x}$	$\hat{z}$	Δ	$\hat{x}$	$\hat{z}$	Δ	$\hat{x}$	$\hat{z}$	Δ
LSDA	656	429	430	1	566	579	13	489	480	9	187	184	3
σ-GGA	691	441	441	0	602	611	9	510	502	8	192	190	2
LSDA+U (this work)	677	449	453	4	596	601	5	516	512	4	193	191	2
LSDA+U (Ref. [214])	687	466			608			521			185		
Experiment (Ref. [224])	692	457			610			515			186		

Table 5.3: Calculated and experimental frequencies for IR active T_{1u} modes, in cm^{-1}.

	1			2			3			4		
	$\hat{x}$	$\hat{z}$	Δ	$\hat{x}$	$\hat{z}$	Δ	$\hat{x}$	$\hat{z}$	Δ	$\hat{x}$	$\hat{z}$	Δ
LSDA	578	602	24	452	476	24	295	386	91	131	201	70
σ-GGA	617	633	16	469	483	14	333	400	67	158	203	45
LSDA+U (this work)	602	614	12	468	480	12	339	391	52	182	206	24
LSDA+U (Ref. [214])	620	630	10	510	526	16	342	392	50	174	198	24
Experiment 9 K (Ref. [213])	619			501			368	379	11	186		
Experiment 13 K (Ref. [213])	619			501			371			186		

Table 5.4: Calculated frequencies for silent modes, in cm^{-1}.

	$A_{2u}(1)$	$A_{2u}(2)$	$E_u(1)$			$E_u(2)$			T_{1g}			$T_{2u}(1)$			$T_{2u}(2)$		
			a	b	Δ	a	b	Δ	$\hat{x}$	$\hat{z}$	Δ	$\hat{x}$	$\hat{z}$	Δ	$\hat{x}$	$\hat{z}$	Δ
LSDA	620	374	451	447	4	263	284	21	410	410	0	415	439	24	204	211	7
σ-GGA	660	414	473	469	4	279	296	17	420	422	2	436	456	20	199	203	4
LSDA+U (this work)	640	431	477	476	1	300	309	9	433	433	0	440	453	13	220	225	5

5.3.3 Phonon Splittings

The inclusion of a U correlation term does make a significant difference in the phonon splittings. Our calculated splittings for the T_{1u} modes are in close agreement with the results of Fennie and Rabe [214]. Among the three methods, there is a definite ordering of the magnitude of the T_{1u} splittings (from largest to smallest): LSDA, σ-GGA, LSDA+U. The Raman mode splittings are smaller than the IR mode splittings, but appear to follow a similar ordering.

The spin-phonon coupling is described by the equation [228]

$$\omega = \omega_0 + \lambda\langle \vec{S}_i \cdot \vec{S}_j \rangle, \tag{5.2}$$

where ω_0 is the phonon frequency in absence of spin correlations, λ is a spin-phonon coupling constant, and the spin correlation is both a thermal average and an average over the crystal, with appropriate weights for each phonon. (Note: In this section, λ is not the electron-phonon coupling constant discussed in Chapters 1 and 6.) We analyze the $T_{1u}(3)$ mode, which has an experimentally measured phonon splitting and a large modulation of the Cr-Cr distance (see Fig. 1 of Ref. [213]). We extract the coupling constant λ_3, using our calculated splitting and the spin-Peierls order parameter [206], $\langle \vec{S}_1 \cdot \vec{S}_2 - \vec{S}_2 \cdot \vec{S}_4 \rangle$ (see Fig. 5.1):

$$\lambda_3 = \frac{\omega_z - \omega_x}{\langle \vec{S}_1 \cdot \vec{S}_2 - \vec{S}_2 \cdot \vec{S}_4 \rangle}. \tag{5.3}$$

For the collinear AFM phase, $S_1 = S_2 = -S_4 = 3/2$, so $\langle \vec{S}_1 \cdot \vec{S}_2 - \vec{S}_2 \cdot \vec{S}_4 \rangle = 4.5$. The calculated and experimental λ_3 are listed in Table 5.1. The ordering of the LSDA, the σ-GGA, and the LSDA+U with respect to both the magnitude of J and the coupling constant is the same.

This ordering can be explained by a direct exchange model of the Cr^{3+} magnetic interactions. Because of the large modulation of Cr-Cr distance in the $T_{1u}(3)$ mode, direct exchange dominates the spin-phonon coupling. For direct exchange,

$$J(r + \delta r) = J(r) e^{-\alpha \delta r}, \tag{5.4}$$

where δr is the displacement from the equilibrium separation distance r of the Cr^{3+} ions, and α is a constant. From a simplified model of a lattice of Cr^{3+} ions connected by springs [213], we have

$$\lambda_3 \propto \frac{d^2 J(r)}{dr^2} = \alpha^2 J(r). \tag{5.5}$$

While not quantitatively correct, the proportionality of λ_3 and J in this model explains the trend in phonon splittings. As J increases, both λ_3 and the magnitude of the phonon splittings increase. While Cr-Cr modulation is not as strong in other modes as in the $T_{1u}(3)$ mode, our calculations suggests that direct exchange plays a role in all the IR modes.

We consider the reason for the ordering of J values. The additional U term of the LSDA+U compared with the LSDA acts as an explicit penalty term for electrons from neighboring ions overlapping or “hopping” from one ion to another. Thus in the LSDA+U the direct exchange interaction is less, and therefore the exchange constant J is smaller in magnitude.

The σ-GGA also tends to describe the localization of electrons better than the LSDA, but not as well as the LSDA+U. This reasoning is supported by the result that the value of the σ-GGA band gap size is in between the LSDA and LSDA+U values. This result suggests that the d orbital overlap between neighboring Cr^{3+} ions, and hence the J, given by σ-GGA should also be in between that given by the LSDA or the LSDA+U.

For both J and λ_3, the LSDA+U results give good agreement with experiment, while the LSDA and σ-GGA results do not agree as well. Our calculations thus demonstrate the importance of including correlation in DFT calculations of phonon splittings and magnetic moments for $ZnCr_2O_4$. Using the LSDA+U value of λ_3 and the experimentally measured splitting for the $T_{1u}(3)$ mode, we obtain

$$\langle \vec{S}_1 \cdot \vec{S}_2 - \vec{S}_2 \cdot \vec{S}_4 \rangle = \frac{\omega_z - \omega_x}{\lambda_3} = 0.92 \tag{5.6}$$

as our value of the spin-Peierls order parameter in real $ZnCr_2O_4$.

5.4 Conclusion

We have calculated ground state properties and the full zone-center optical phonon spectrum for $ZnCr_2O_4$ in the collinear AFM phase using the LSDA, σ-GGA, and LSDA+U methods. All three methods give the proper insulating ground state, with the overall magnitude of phonons close to experiment for the σ-GGA and the LSDA+U and slightly softer for the LSDA, implying that U is not required to calculate some properties of $ZnCr_2O_4$. This result is in contrast to other AFM insulating oxides, such as MnO. However, an explicit U term is necessary to get an exchange constant J and spin-phonon coupling parameter λ in agreement with experiment. The J dependence of the splittings is consistent with a picture in which direct exchange dominates the magnetic interactions between Cr^{3+} ions in $ZnCr_2O_4$. We have confirmed previous results that show that magnetic ordering has a significant effect on the lattice degrees of freedom of $ZnCr_2O_4$. We conclude that correlation effects are important in $ZnCr_2O_4$. Further application of the LSDA+U and σ-GGA+U methods to spin-phonon coupling, spinels, and magnetic oxides can give a more complete picture of electron correlation in these materials.

Chapter 6

Electron-phonon coupling and superconductivity in arsenic under pressure

In the previous chapter, we studied spin-phonon coupling in an insulating magnetic material. In this chapter, we study electron-phonon coupling in metallic arsenic. We perform first-principles calculations of the electronic structure, phonon dispersion, and electron-phonon coupling in elemental As at various pressures above and below the rhombohedral $A7$ to simple cubic (sc) structural transition. We find that the electron-phonon coupling constant λ, and hence the superconducting transition temperature T_c, is largest near the structural transition and decreases away from it. Changes in λ as a function of pressure are primarily explained by changes in the density of states at the Fermi level for pressures below the transition, and by changes in phonon frequency for pressures above the transition. Although the couplings to the Γ_1 optical phonon mode (for $A7$) and the R phonon mode (for sc) are large, the contribution of these modes to λ for their respective structures is modest. Work presented in this chapter has been published in Ref. [229].

6.1 Introduction

For many materials, applying pressure is known to cause structural phase transitions and changes in superconducting transition temperature (T_c) [230]. A striking example is elemental Li, which undergoes several structural phase transitions with increasing pressure and reaches a T_c as high as 20 K [13–15]. Crystalline elemental As is known experimentally to undergo a transition from the rhombohedral $A7$ structure at ambient pressure to the simple cubic (sc) structure at around 25-32 GPa as pressure is increased [231, 232]. The stability of the $A7$ structure at ambient pressure and the transition to sc with increasing pressure can be explained by a Peierls distortion mechanism. In such a mechanism, strong coupling of electrons to the sc R and $A7$ Γ_1 optical phonon modes, Fermi surface nesting, a Kohn anomaly are all involved [233–237].

In addition, As under pressure is superconducting [238, 239], with the most recent study measuring a peak in T_c around the pressure of the phase transition [18]. In this study, this peak in T_c was explained qualitatively by changes in the electronic density of states at the Fermi level (ϵ_F) and the phonon frequencies of the $A7$ Γ_1 optical mode and the *sc* R mode.

While these phenomena demonstrate that electron-phonon (e-p) coupling is important in As, it would be interesting to understand the role of e-p coupling in more detail. In particular, a precise understanding of the relative importance of changes in the density of states at ϵ_F [$N(\epsilon_F)$], phonon frequency, and e-p matrix elements to changes in T_c would be useful. In addition, the importance of particular phonon wavevectors in superconductivity has been demonstrated in Li and other materials [240–242]. Given that the *sc* R mode has particular importance in the structural transition in As, its role in superconductivity would also be interesting to understand. Such physical insight might also be applicable to our understanding of other materials that undergo changes in structure and T_c with pressure, such as the other Group V elements.

Detailed studies of e-p coupling are now possible with recent methodological developments and increasing computational power. In particular, a recently developed method based on Wannier functions allows the study of e-p coupling on fine grids in the Brillouin zone (BZ) for electron and phonon states [243, 244].

In the present study, we perform first-principles calculations of the electronic structure, phonon dispersion, and e-p coupling in As as a function of pressure around the $A7$ to *sc* transition. Our results for T_c are in good agreement with experiment. We verify that the peak in T_c is directly related to the structural transition, and we study the changes as a function of pressure of the phonons, $N(\epsilon_F)$, e-p matrix elements, the e-p coupling constant λ, and T_c. We find that the softening of the $A7$ optical mode/*sc* R mode does not have a large direct effect on T_c. The main importance of this mode is its role in the $A7$ to *sc* structural transition, which leads to a large change in $N(\epsilon_F)$ and thus a large change in T_c. Furthermore, we find that the change in T_c above the structural transition pressure is primarily due to changes in average phonon frequency across all modes.

In Sec. 6.2, we briefly describe the $A7$ structure and its relation to the *sc* structure. The method and computational details for the present study are given in Sec. 6.3. In Sec. 6.4 we present our results, divided into the following subsections: the structure of As as a function of pressure (Sec. 6.4.1) and the e-p properties of the *sc* structure (Sec. 6.4.2) and the $A7$ structure (Sec. 6.4.3). General trends for e-p coupling as a function of pressure and a comparison of our results to experiment are presented in Sec. 6.5. In Sec. 6.6 we conclude this chapter.

6.2 $A7$ and *sc* structures in arsenic

The rhombohedral $A7$ structure contains two atoms per unit cell and can be specified by three parameters: the lattice constant a_{rhom}, the rhombohedral angle α between two direct lattice vectors, and the internal parameter u, which determines the distance between the two atoms in the cell. An $A7$ structure having the same species for its two basis atoms and with $\alpha = 60°$ and $u = 0.25$ is equivalent to the *sc* structure.[1]

---

[1] For a more detailed description of the $A7$ structure, see Ref. [234] or other references cited in this chapter.

Elemental As at ambient pressure exists in the $A7$ structure with experimentally measured lattice parameters of $a_{\text{rhom}} = 4.1018$ Å, $\alpha = 54.554°$, and $u = 0.2276$ (at 4.2 K) [245]. The structure is layered, with each As atom forming strong p-like bonds to each of its three nearest intralayer neighbors, while interlayer bonding is weaker. The stability of the $A7$ structure with respect to sc at ambient pressure can be understood in terms of a Peierls mechanism. The rhombohedral distortion and the displacement of atoms away from the sc positions, as indicated by the decreased u parameter, allow the formation of covalent p-like bonds, open a gap at ϵ_F, and lower the overall energy of the crystal.

As pressure is increased, the energy gain from the Peierls-like distortion with respect to the sc structure decreases, and the degree of distortion decreases until the sc structure becomes stable at the transition pressure. The transition from $A7$ to sc with increasing pressure has been observed experimentally [231, 232] and has been the subject of many theoretical studies [18, 234–237, 246–253].

The displacement of atoms involved in the transition between the $A7$ and sc structures corresponds to the $A7$ Γ_1 optical mode. In the sc structure, the wavevector of this mode is at the R point in the BZ.

6.3 Method and Computational Details

Our general procedure is as follows. We first determine the structural parameters of As as a function of pressure and the $A7$ to sc transition pressure by performing variable-cell relaxation calculations for various target pressures. Then, for selected pressures below and above the transition, we calculate the electronic structure, phonon modes, and e-p coupling. These quantities are then used to study the pressure dependence of T_c.

6.3.1 Electron-Phonon Coupling Formalism

We study the e-p coupling within a many-body formalism [66–68], as outlined in Sec. 1.2.5. The e-p matrix element for the scattering of an electron in band n at wavevector $\mathbf{k}$ to a state in band m with wavevector $\mathbf{k}+\mathbf{q}$ by a phonon with mode index ν at wavevector $\mathbf{q}$ is given by Eq. 1.71; we repeat it here for convenience:

$$g_{mn}^{\nu}(\mathbf{k},\mathbf{q}) = \left(\frac{\hbar}{2M\omega_{\mathbf{q}\nu}}\right)^{1/2} \langle m, \mathbf{k}+\mathbf{q}|\delta_{\mathbf{q}\nu}V_{SCF}|n, \mathbf{k}\rangle. \tag{6.1}$$

In this expression, $|n, \mathbf{k}\rangle$ is the bare electronic Bloch state, $\omega_{\mathbf{q}\nu}$ is the screened phonon frequency, M is the ionic mass, and $\delta_{\mathbf{q}\nu}V_{SCF}$ is the derivative of the self-consistent potential with respect to a collective ionic displacement corresponding to phonon wavevector $\mathbf{q}$ and mode ν. The quantities entering into Eq. 6.1 are obtained from first-principles band structure and phonon calculations, as described in Sec. 6.3.2.

The main quantities to be calculated are the phonon linewidth $\gamma_{\mathbf{q}\nu}$, the phonon-mode-dependent coupling constant $\lambda_{\mathbf{q}\nu}$, the Eliashberg spectral function $\alpha^2F(\omega)$, and the average e-p coupling constant (or mass enhancement parameter) λ. In the Migdal approximation [70], the phonon linewidth is given by Eq. 1.77; converting the integral over the BZ to a sum, we have

$$\gamma_{\mathbf{q}\nu} = \pi\omega_{\mathbf{q}\nu}\sum_{mn}\sum_{\mathbf{k}} w_{\mathbf{k}}|g^{\nu}_{mn}(\mathbf{k},\mathbf{q})|^2\delta(\epsilon_{m,\mathbf{k}+\mathbf{q}}-\epsilon_F)\delta(\epsilon_{n,\mathbf{k}}-\epsilon_F), \tag{6.2}$$

where $w_{\mathbf{k}}$ is the k-point weight (normalized such that $\sum_{\mathbf{k}} w_{\mathbf{k}} = 2$). The sum over electron wavevectors $\mathbf{k}$ can be performed on a uniform grid over the whole BZ, or over the irreducible BZ (IBZ), with appropriate weights. The phonon-mode-dependent coupling constant is given by

$$\lambda_{\mathbf{q}\nu} = \frac{\gamma_{\mathbf{q}\nu}}{\pi N(\epsilon_F)\omega^2_{\mathbf{q}\nu}}. \tag{6.3}$$

In terms of the phonon linewidths, $\alpha^2F(\omega)$ is given by Eq. 1.78 [71]. Converting the integral to a sum, we get

$$\alpha^2F(\omega) = \frac{1}{2\pi N(\epsilon_F)}\sum_{\mathbf{q}\nu} w_{\mathbf{q}}\frac{\gamma_{\mathbf{q}\nu}}{\omega_{\mathbf{q}\nu}}\delta(\omega-\omega_{\mathbf{q}\nu}). \tag{6.4}$$

The sum over phonon wavevector $\mathbf{q}$ is performed either on a uniform grid over whole the BZ, or over the IBZ, with appropriate weights $w_{\mathbf{q}}$, where $\sum_{\mathbf{q}} w_{\mathbf{q}} = 1$. In Eqs. 6.3 and 6.4, $N(\epsilon_F)$ is the density of states at ϵ_F per unit cell and per spin. As in Eq. 1.79, the coupling constant λ is given by the integral

$$\lambda = 2\int_0^\infty \frac{\alpha^2F(\omega)}{\omega}d\omega. \tag{6.5}$$

Other important frequency moments of $\alpha^2F(\omega)$ are defined as follows:

$$\langle\omega^2\rangle = \frac{2}{\lambda}\int_0^\infty \omega\alpha^2F(\omega)d\omega \tag{6.6}$$

and

$$\omega_{\log} = \exp\left(\frac{2}{\lambda}\int_0^\infty \log\omega\frac{\alpha^2F(\omega)}{\omega}d\omega\right). \tag{6.7}$$

Conventional electron-phonon superconductors are well-described by the Eliashberg theory of superconductivity [65], which is based on the BCS theory [11]. Within the isotropic approximation to the Eliashberg theory, we can determine the superconducting transition temperature T_c using the Allen-Dynes-modified McMillan equation, Eq. 1.90 [72,73]:

$$T_c = \frac{\omega_{\log}}{1.2}\exp\left(-\frac{1.04(1+\lambda)}{\lambda-\mu^*(1+0.62\lambda)}\right), \tag{6.8}$$

where μ^* is the Coulomb psuedopotential [74].

6.3.2 Computational Details

All of our electronic structure, phonon, and e-p calculations are performed from first-principles using the QUANTUM-ESPRESSO (QE) code [157] within the framework of density-functional theory [20,21] and with the local-density approximation (LDA) [23,24]. The As ions are modeled using norm-conserving pseudopotentials [37], while the valence electron states (five valence electrons per atom) are calculated using a plane-wave basis set [27] with an energy cutoff of 50 Ry.

Following previous studies [248, 250–252], we calculate the structure of As as a function of pressure by performing a variable-cell relaxation at constant pressure until the components of the forces on the atoms are less than 10^{-4} Ry/a.u. and the pressure is within 0.05 GPa of the target pressure. For all such relaxations, the starting structure is that of the experimental $A7$ structure [245] (see Sec. 6.2).

Close to the transition pressure, the structure is sensitive to the k-point sampling of the BZ and the smearing used to occupy the electronic states. We found that using a Methfessel-Paxton (MP) smearing [254] of 0.3 eV and a $40 \times 40 \times 40$ shifted k-grid [220] allowed us to converge a_{rhom}, α, and u to within 0.01 Å, 0.1°, and 0.001, respectively, for the pressures we considered. These parameters are comparable to those used in Ref. [252], in which convergence was studied in detail.

For selected pressures, we calculate the elecronic structure, phonons, and e-p coupling. Convergence of $\gamma_{\mathbf{q}\nu}$ and $\alpha^2F(\omega)$ (Eqs. 6.2 and 6.4) requires the calculation of e-p matrix elements on a fine grid for both electrons and phonons. With the electron-phonon-Wannier method [243, 244], such a calculation can be performed with relatively low computational cost. The e-p matrix elements are computed from first principles on coarse electron and phonon grids and then interpolated onto arbitrarily fine k- and q-grids by Wannier-Fourier interpolation. The accuracy of this interpolation is checked by examining the real space localization of the electronic Wannier states and the phonon perturbation (related to the range of the interatomic force constants). Maximally localized Wannier functions [255, 256] are obtained with the WANNIER90 code [257].

The computational parameters for the e-p calculations are as follows. For pressures below the structural transition, we use the unit cell of the $A7$ structure. The self-consistent charge density is computed using a $20 \times 20 \times 20$ shifted k-grid and a 0.3 eV MP smearing for the occupation of the electronic states. Wannier functions are computed for the lowest eight bands, including all bands crossing ϵ_F. For the e-p matrix elements, electronic states are computed on a uniform $6 \times 6 \times 6$ Γ-centered coarse k-grid, while phonons are computed using a $6 \times 6 \times 6$ Γ-centered coarse q-grid. The matrix elements are interpolated onto uniform Γ-centered fine k- and q-grids of $80 \times 80 \times 80$ and $14 \times 14 \times 14$, respectively.

For pressures above the structural transition, we use the unit cell for the sc structure. The density is computed using a $32 \times 32 \times 32$ shifted k-grid with a 0.3 eV MP smearing for the occupations. Wannier functions are computed for the lowest four bands. Grids centered at Γ of $6 \times 6 \times 6$ (coarse) and $100 \times 100 \times 100$ (fine) for electrons and $6 \times 6 \times 6$ (coarse) and $16 \times 16 \times 16$ (fine) for phonons were used.

In Eq. 6.2, the δ-functions are approximated by Gaussian functions of width 0.01 Ry for all pressures.

The phonon calculations are performed using density-functional perturbation theory (DFPT) [47], as implemented in QE. No anharmonic contribution is included. Near the structural phase transition, the $A7$ Γ_1 optical and sc R phonon modes soften considerably, and the anharmonic contributions are significant [18, 235]. Since the pressures at which we perform our e-p calculations are not too close to the transition, the harmonic approximation is satisfactory: Although there is some error in the phonon frequencies for these particular modes, it does not effect the main results. Anharmonic effects are discussed further in Sec. 6.4.

6.4 Results

6.4.1 Determination of As structure as a function of pressure

We performed variable-cell relaxation calculations for target pressures at 5 GPa intervals in the range 0-50 GPa. The $A7$ lattice parameters, as well as the nearest neighbor (d_1) and next-nearest neighbor (d_2) distances between As atom positions, are plotted in Fig. 6.1. The lattice constants at 0 GPa agree well with previous LDA calculations [234, 236, 246–248, 252].

The $A7$ and *sc* structures are most easily distinguished by comparing d_1 and d_2 (Fig. 6.1(d)). When $d_1 \neq d_2$, the crystal is in the $A7$ structure, while $d_1 = d_2$ in the *sc* structure. Our calculated transition pressure is between 20 and 25 GPa, consistent with the most detailed previous theoretical work [252].

A fit of the calculated energy versus volume values from 0 to 50 GPa to a Murnaghan equation of state [258] (EOS) gives $B_0 = 57.2$ GPa and $B' = 4.21$ for the bulk modulus and its derivative, respectively, in reasonable agreement with the experimental values of 55.6 GPa and 4.4 (Ref. [231]) and 58.4 GPa and 3.34 (Ref. [232]). It is known that, compared to experiment, the LDA tends to underestimate the volume at a given pressure. To convert our calculated pressure to an experimental one, we input the calculated volume into a Murnaghan EOS with experimental B_0 and B' and use the resulting pressure. With this conversion procedure, the theoretical pressures of 20 and 25 GPa correspond to experimental pressures of 28 and 35 GPa, respectively, using parameters from Ref. [231], and 25 and 30 GPa, respectively, using parameters from Ref. [232]. The respective experimental transition pressures of 32 and 25 GPa from the two experiments are consistent with our calculations, although the pressure resolution in our calculation is not very fine, and the method of relating calculated to experimental pressures is not rigorously justified.

We study the electronic structure, phonons, and e-p coupling at three (theoretical) pressures (0, 10, and 20 GPa) for which As is in the $A7$ structure below the transition, and three pressures (30, 40, and 50 GPa) for which As is in the *sc* structure above the transition.

6.4.2 As in the sc structure

Before discussing properties of As in the more complicated $A7$ structure, we present our results for *sc* As.

The band structure along high-symmetry directions and the density of states $N(\epsilon)$ for *sc* As at 30, 40, and 50 GPa are given in Figs. 6.2 and 6.3. (Here we have normalized $N(\epsilon)$ to be per atom, with contributions from both spins summed.) At all pressures, three bands cross ϵ_F. The bands broaden but otherwise do not change significantly as pressure is increased. The most significant change in the electronic structure is the decrease in $N(\epsilon_F)$ as pressure is increased (Fig. 6.3). This trend is in agreement with the calculations of Ref. [18], although there are quantitative differences. Values for $N(\epsilon_F)$ are presented in Table 6.1.

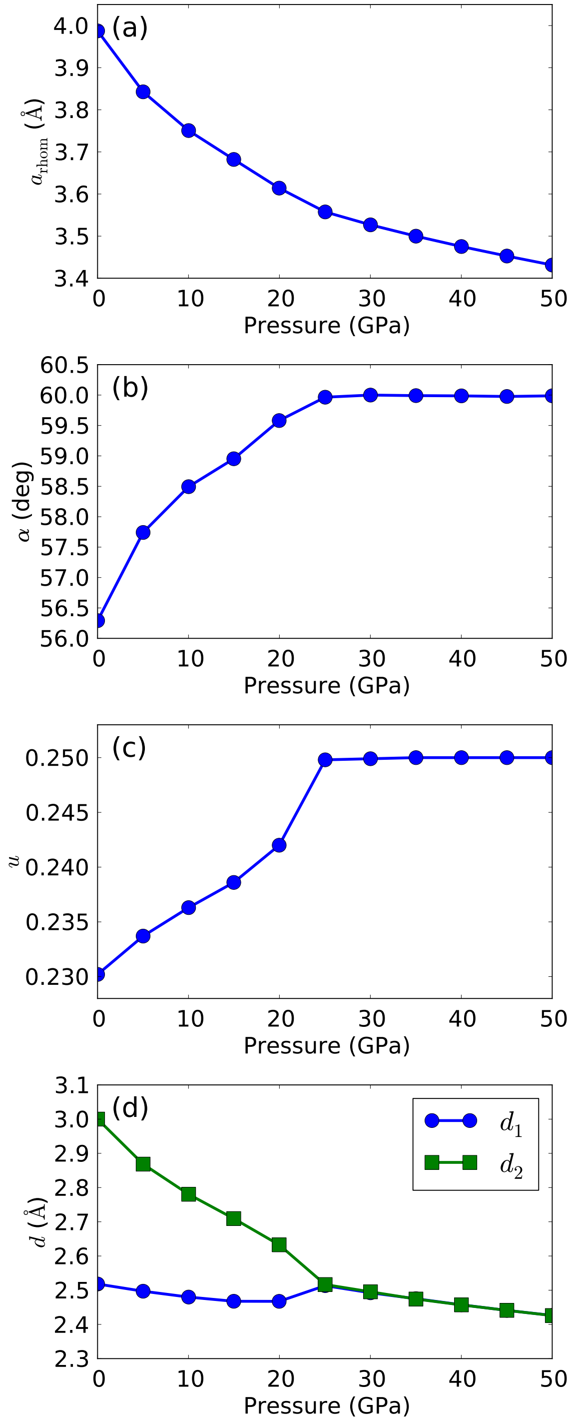

Figure 6.1: Lattice parameters (a) a_{rhom}, (b) α, and (c) u, and (d) nearest neighbor d_1 and next-nearest neighbor d_2 distances for variable-cell relaxation calculations of As in the $A7$ structure with target pressures between 0 and 50 GPa. The transition pressure from $A7$ to sc is found to be between 20 and 25 GPa.

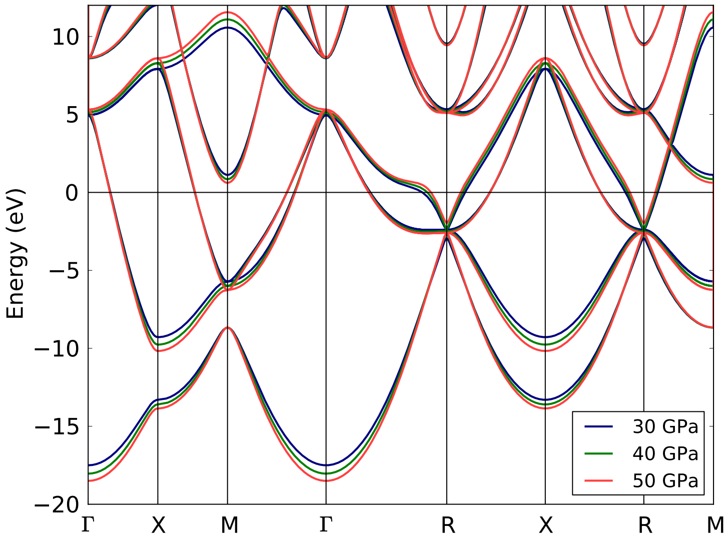

Figure 6.2: Electronic band structure for *sc* As at 30, 40, and 50 GPa. Energies are relative to ϵ_F.

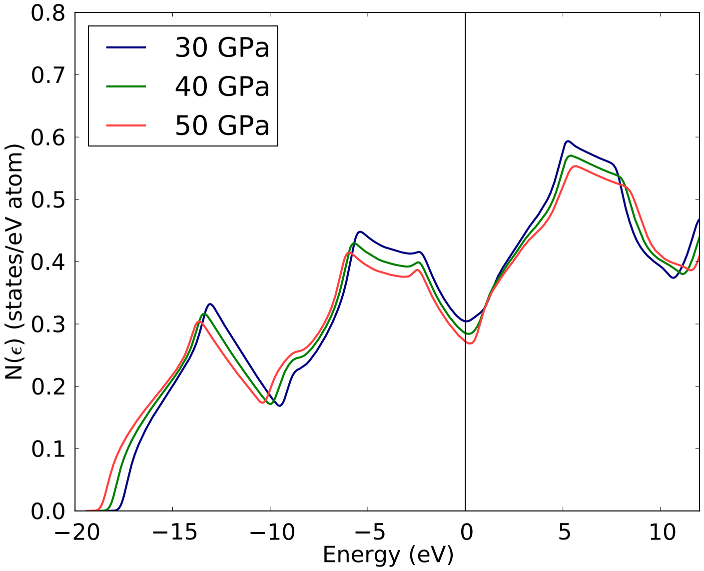

Figure 6.3: Electronic density of states $N(\epsilon)$ for *sc* As at 30, 40, and 50 GPa. Energies are relative to ϵ_F.

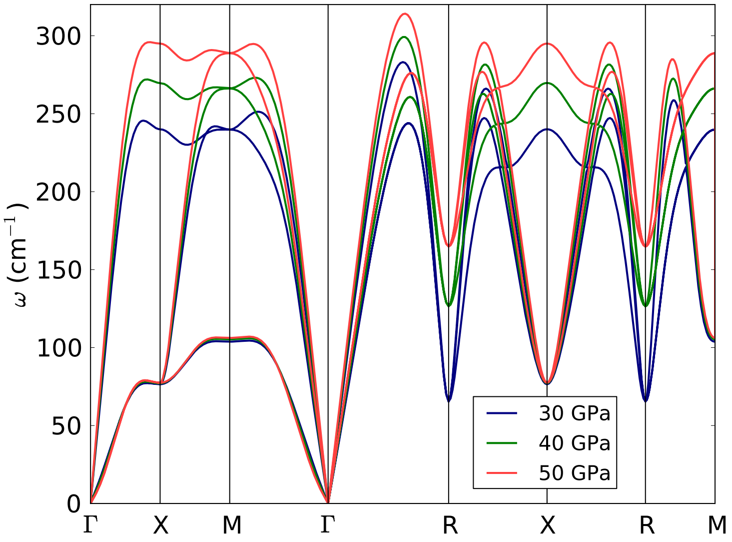

Figure 6.4: Phonon dispersion for *sc* As at 30, 40, and 50 GPa.

Figure 6.4 shows the phonon dispersions for *sc* As at 30, 40, and 50 GPa. Overall, as pressure increases, the phonon frequencies increase, as expected. A significant change in phonon frequency occurs for wavevectors near the R point in the BZ. Approaching the transition pressure from above, the R phonon softens significantly. Previous studies have indicated that Fermi surface nesting plays an important role in this phonon softening [236, 237].

The frequency of the R mode has been computed previously using the frozen phonon method [18, 235]. In comparison to our calculations, the frequencies from Ref. [235] are softer at corresponding volumes. This discrepancy may be due to differences in k-point sampling or plane-wave energy cutoff. Our calculated frequencies are lower than those of Ref. [18] by approximately 50% at 30 GPa and 25% at 50 GPa. This difference indicates the degree of anharmonicity of the R mode, since anharmonic effects were included in Ref. [18] but not in the present study.

The e-p coupling parameter $\lambda_{\mathbf{q}} = \sum_{\nu} \lambda_{\mathbf{q}\nu}$ is plotted along high-symmetry directions in the BZ in Fig. 6.5. The coupling at R, reaching values of 35, 9.8, and 6.1 for 30, 40, and 50 GPa, respectively, is much larger than at other points in the BZ. The change in $\lambda_{\mathbf{q}}$ at R with pressure can mainly be attributed to the change in $\omega_{\mathbf{q}\nu}$, as the change in $\gamma_{\mathbf{q}\nu}$ is small, and the change in $N(\epsilon_F)$ is modest.

The calculated $F(\omega)$ and $\alpha^2F(\omega)$ for *sc* As are plotted in Fig. 6.6 (a Gaussian smearing of width 0.5 meV $\approx$ 4 cm^{-1} is used). The shape of $\alpha^2F(\omega)$ is very similar to that of $F(\omega)$. The main difference is the enhanced weight for higher frequencies for $\alpha^2F(\omega)$ compared to $F(\omega)$.

The enhanced coupling to higher frequencies can be explained qualitatively as follows. Higher frequency modes correspond to compression or stretching of bonds, while

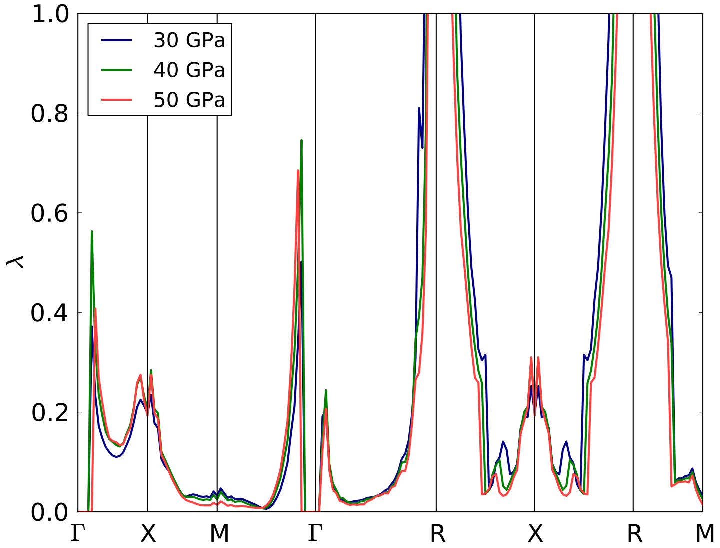

Figure 6.5: Electron-phonon coupling parameter $\lambda_{\mathbf{q}}$ for *sc* As at 30, 40, and 50 GPa. The values of the peak at R are 35, 9.8, and 6.1 for 30, 40, and 50 GPa, respectively.

lower frequency modes correspond to bond bending. Modes which change bond length modify the overlap of the half-filled p-like orbitals and thus change the electronic structure near ϵ_F, in a manner similar to a Peierls distortion. Such modes therefore couple strongly to electrons at ϵ_F. On the other hand, bond-bending modes do not affect the overlap of p-like orbitals as much, and therefore couple less strongly.

The integrated λ as a function of frequency is also plotted in Fig. 6.6 (bottom) for the three pressures considered. As $\alpha^2F(\omega)$ shifts to higher frequencies with higher pressure, λ decreases.

The calculated $\omega_{\log}$, $\langle\omega^2\rangle^{1/2}$, λ, and T_c (for two values of μ^*) are given in Table 6.1. For *sc* As, as pressure increases, the average phonon frequency increases, $N(\epsilon_F)$ decreases, and λ decreases, leading to a decrease in T_c. Similar values for $N(\epsilon_F)$ and λ were obtained in a previous study [259], although those calculations were not from first principles.

As pressure is decreased towards the transition from above, the increase in coupling $\lambda_{\mathbf{q}}$ is much greater at points near R than at other regions of the BZ. As noted previously, this increase in coupling is mainly due to phonon softening. An interesting question is how much this particular coupling to phonons near R directly contributes to the increase in total λ. To answer this question, we estimate what the increase in λ from 50 to 30 GPa would be if there were no special coupling enhancement near R. We calculate λ^P_{cut}, the coupling at pressure P due to all q-points at least $0.3(\pi/a_{\text{cubic}})$ away from R in reciprocal space, where a_{cubic} is the *sc* lattice constant. We then get a new value $\lambda_{\text{scaled}} = \lambda^{50\text{GPa}}\left(\lambda^{30\text{GPa}}_{\text{cut}}/\lambda^{50\text{GPa}}_{\text{cut}}\right)$, which is the estimated coupling at 30 GPa without the special coupling enhancement at R. We find $\lambda_{\text{scaled}} = 0.46$, while $\lambda^{30\text{GPa}} = 0.50$. Therefore, the extra coupling near R contributes a 0.04 increase in λ, whereas the overall increase in λ going from 50 to 30 GPa

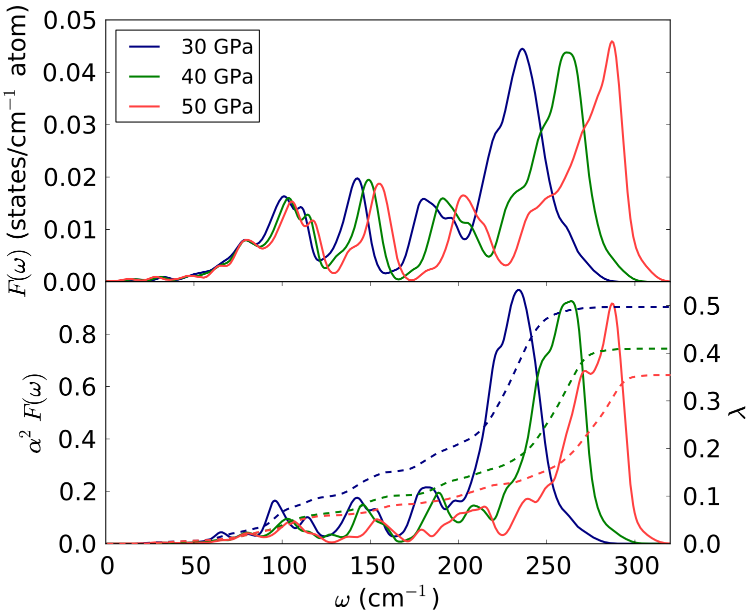

Figure 6.6: Phonon density of states $F(\omega)$ (top), Eliashberg spectral function $\alpha^2 F(\omega)$ (bottom, solid), and integrated λ (bottom, dashed) for *sc* As at 30, 40, and 50 GPa.

is 0.14. We conclude that the increase in total λ is not dominated by the R mode; rather, a broad range of modes contributes to the increase.

The overall trends in e-p parameters as a function of pressure will be dicussed further in Sec. 6.5.

6.4.3 As in the $A7$ structure

The calculated band structure (Fig. 6.7) and $N(\epsilon)$ (Fig. 6.8) at 0 GPa are in good agreement with previous theoretical studies [234, 236, 249]. As pressure increases to 20 GPa, the bands broaden and $N(\epsilon_F)$ increases significantly, as seen in the plot of $N(\epsilon)$ (Fig. 6.8). Values for $N(\epsilon_F)$ are given in Table 6.1. A similar increase in $N(\epsilon_F)$ was found in Ref. [18], although there are quantitative differences. Note also how the shape of $N(\epsilon)$ for $A7$ As approaches that of *sc* As (Fig. 6.3) as the pressure increases towards the structural transition pressure.

The phonon dispersions at 0, 10, and 20 GPa are given in Fig. 6.9. An overall hardening of phonons occurs with increased pressure. However, the optical phonon modes at Γ soften with increased pressure as the structural transition is approached. As pressure is increased and the structure moves closer to *sc*, the splitting between the optical modes at Γ decreases. These modes become degenerate when the *sc* structure is reached. The dispersion for 0 GPa is consistent with previous experimental [260] and theoretical [237] studies. Slight differences are likely due to the slightly smaller volume used for the present calculation. For all pressures considered, the calculated Γ_1 optical frequencies are in good agreement with previous frozen phonon calculations [18, 234]. The calculations, which include

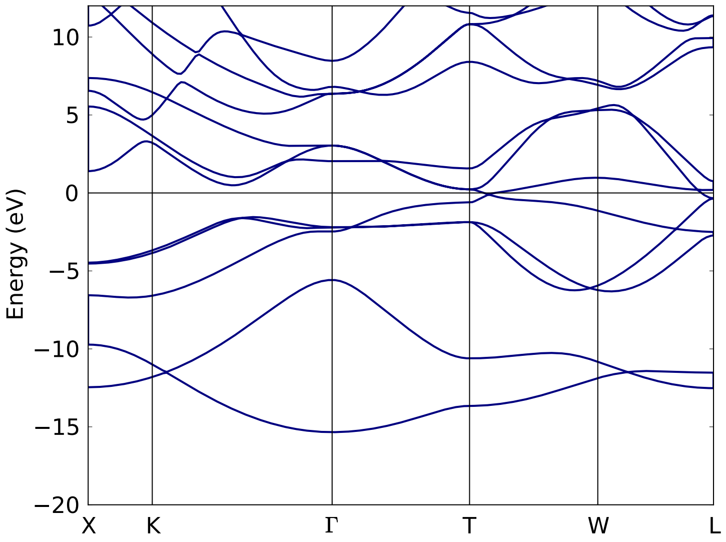

Figure 6.7: Electronic band structure for $A7$ As at 0 GPa. Energies are relative to ϵ_F.

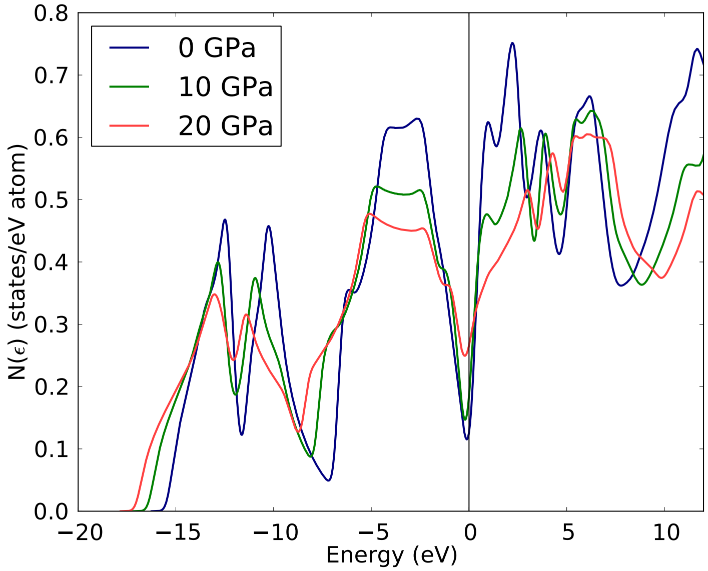

Figure 6.8: Electronic density of states $N(\epsilon)$ for $A7$ As at 0, 10, and 20 GPa. Energies are relative to ϵ_F.

only the harmonic contribution, underestimate the experimental Raman frequencies [232], with increasing error as the transition pressure is approached, indicating the increasing anharmonicity of this phonon mode.

Figure 6.10 (top) shows $F(\omega)$ for 0, 10, and 20 GPa. Separate contributions from the acoustic and optical branches are shown, as well as the total. In general, both branches shift towards higher frequencies with higher pressure; the acoustic branch broadens in frequency, while the width of the optical branch does not change much. A low frequency tail, corresponding to the optical modes near Γ, appears in $F(\omega)$ for higher pressures.

The total and separate acoustic and optical contributions to $\alpha^2F(\omega)$ are shown in Fig. 6.10 (bottom). The higher frequency optical modes have a greater e-p coupling than the lower frequency acoustic modes, as seen by comparing the spectral weight of $F(\omega)$ and $\alpha^2F(\omega)$. A similar effect for *sc* As was noted and explained qualitatively in Sec. 6.4.2.

The integrated λ is also shown in Fig. 6.10 (bottom). The total λ increases significantly, from 0.19 to 0.43, when pressure is increased from 0 GPa to 20 GPa. In the acoustic modes, a significant increase of ~ 0.1 in the integrated λ occurs when going from 0 to 10 GPa, while a further increase to 20 GPa does does not increase the contribution from acoustic modes to λ much. The optical mode contribution increases more than the acoustic mode contribution upon increase of pressure from 10 to 20 GPa.

The coupling of the optical modes at Γ is very large, with $\lambda_{\mathbf{q}}$ reaching a value of 20 at 20 GPa. Both an increasing e-p matrix element and phonon softening contribute to this large value of $\lambda_{\mathbf{q}}$. However, the phase space near Γ is small, as seen in Fig. 6.10 (top right), where in the range 100–200 cm^{-1}, the optical contribution to $F(\omega)$ is small. Therefore, although the coupling is large for the optical modes at Γ, the contribution of these modes to the increase in total λ with increasing pressure is quite modest. From the integrated λ curve, we estimate that the contribution of these modes to the increase in λ from 0 to 20 GPa is about 0.05, while the total increase in λ is 0.24. Furthermore, if anharmonic effects were included in the calculation, the e-p coupling of the optical modes near Γ would likely decrease due to an increased phonon frequency, leading to an even smaller contribution to the increase in total λ. Thus the phonon softening itself is not the main direct cause of the increase in λ with increasing pressure.

The primary importance of the phonon softening is indirect. Phonon softening leads to structural changes and changes in electronic structure, the most important of which is the increase in $N(\epsilon_F)$. As discussed in Sec. 6.5, the increase in $N(\epsilon_F)$ is the dominant cause of increasing λ with pressure in the $A7$ structure.

The e-p quantities for $A7$ As are summarized in Table 6.1.

6.5 Discussion

To understand the relative contributions of changes in phonon frequencies, $N(\epsilon_F)$, and e-p matrix elements to changes in λ as a function of pressure, we consider the relation [72]

$$\lambda = \frac{N(\epsilon_F)\langle g^2\rangle}{M\langle\omega^2\rangle}, \tag{6.9}$$

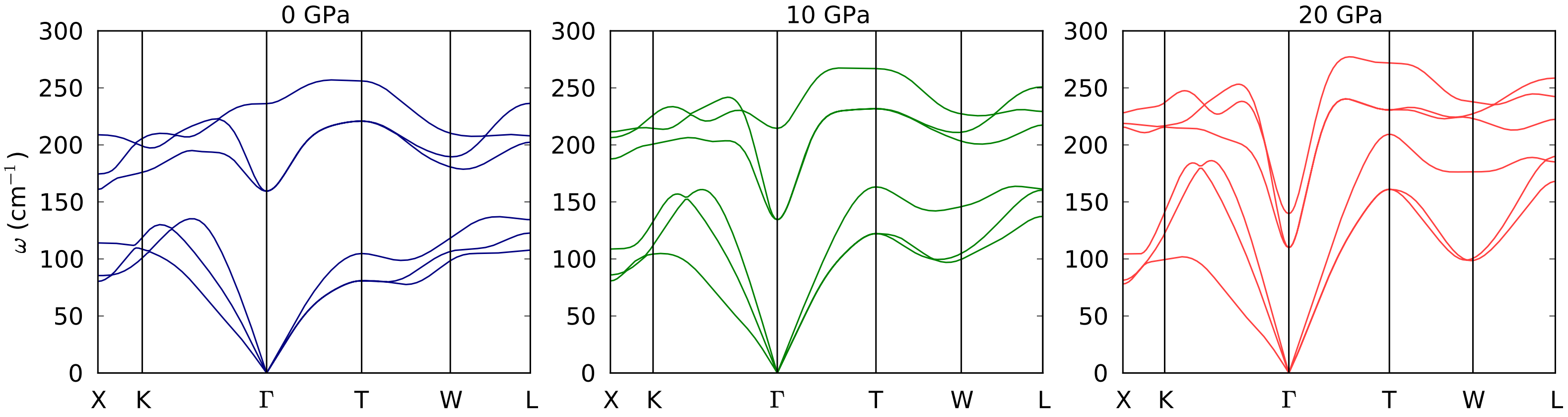

Figure 6.9: Phonon dispersion $\omega_{\mathbf{q}\nu}$ for $A7$ As at 0 GPa (left), 10 GPa (middle), and 20 GPa (right).

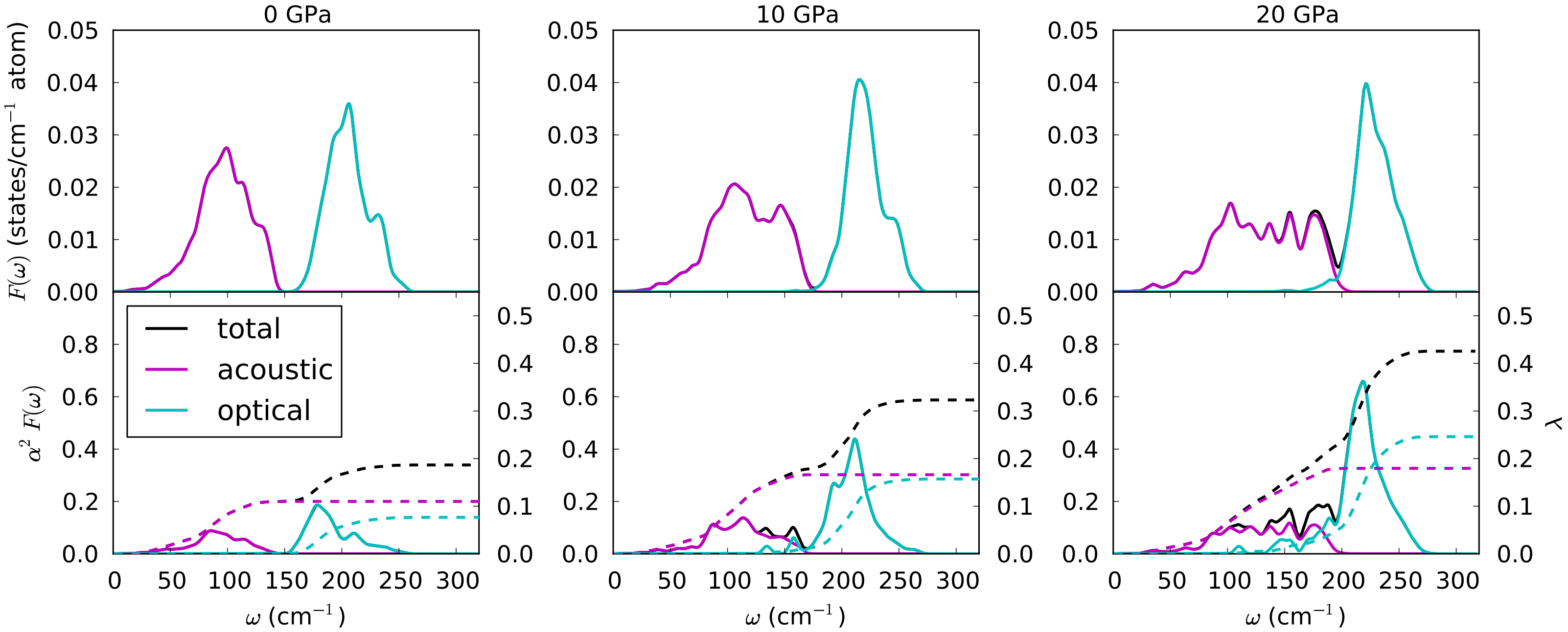

Figure 6.10: Total, acoustic, and optical contributions to the phonon density of states $F(\omega)$ (top), Eliashberg spectral function $\alpha^2 F(\omega)$ (bottom, solid), and integrated λ (bottom, dashed) for $A7$ As at 0 GPa (left), 10 GPa (middle), and 20 GPa (right).

Table 6.1: Calculated frequency moments, $N(\epsilon_F)$, electron-phonon coupling parameter λ, and superconducting transition temperature T_c for As at various pressures.

P (GPa)	Structure	$\omega_{\log}$ (K)	$\langle\omega^2\rangle^{1/2}$ (K)	$N(\epsilon_F)$ (states/eV atom)	λ	T_c (K)	
						$\mu^* = 0.10$	$\mu^* = 0.15$
0	*A7*	158	199	0.073	0.19	0.00	0.00
10	*A7*	194	232	0.148	0.32	0.19	0.01
20	*A7*	227	260	0.247	0.43	1.34	0.35
30	*sc*	253	284	0.290	0.50	2.99	1.19
40	*sc*	283	317	0.266	0.41	1.36	0.32
50	*sc*	298	341	0.253	0.35	0.58	0.07

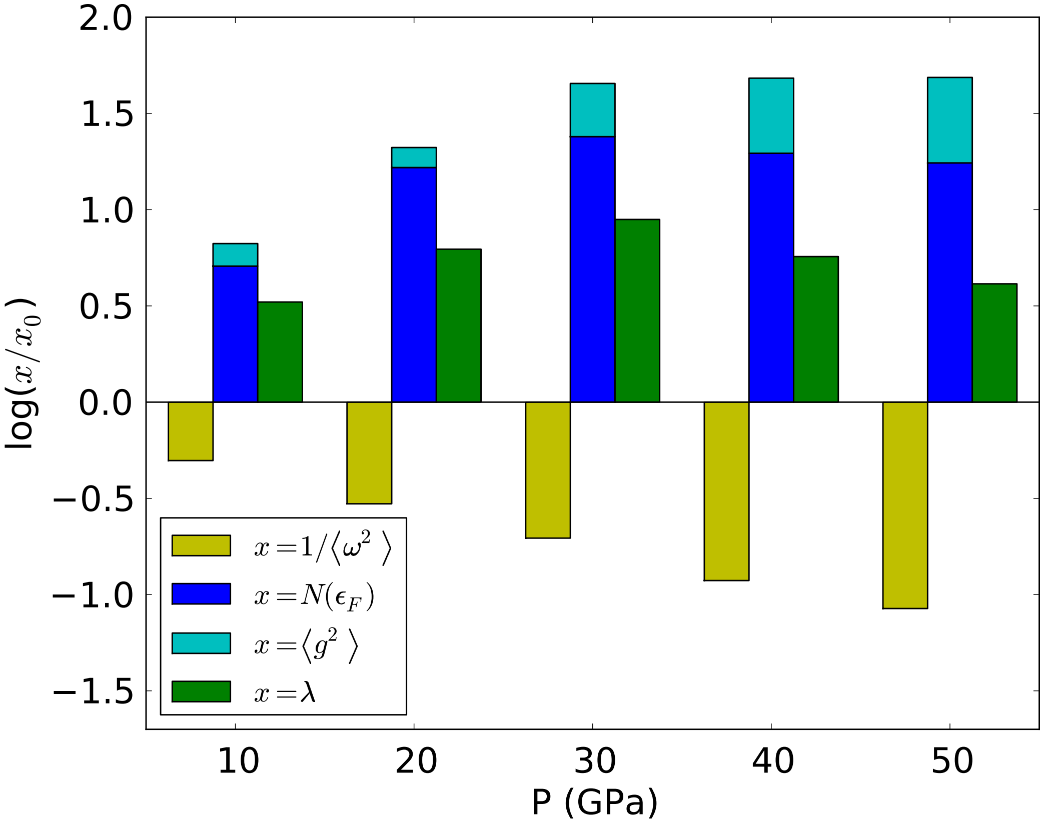

Figure 6.11: Trends in average phonon frequency $\langle\omega^2\rangle$, $N(\epsilon_F)$, average e-p matrix element $\langle g^2\rangle$, and e-p coupling λ as a function of pressure. The subscript 0 denotes the value at 0 GPa.

where $\langle g^2 \rangle$ is the average over the Fermi surface of the e-p matrix element, and M is the ionic mass. Values for $\langle g^2 \rangle$ are obtained indirectly using Eq. 6.9 from the calculated values of λ, $N(\epsilon_F)$, and $\langle \omega^2 \rangle$, as given in Table 6.1. (Other general relations between quantities relevant for superconductivity are presented in Ref. [261].)

To analyze relative changes as a function of pressure, we take the natural logarithm of the quantities, normalized to the value at 0 GPa, and plot them in Fig. 6.11 for the range 10-50 GPa. From Eq. 6.9, we have

$$\log \frac{\lambda}{\lambda_0} = \log \frac{N(\epsilon_F)}{N(\epsilon_F)_0} + \log \frac{\langle g^2 \rangle}{\langle g^2 \rangle_0} + \log \frac{\langle \omega^2 \rangle_0}{\langle \omega^2 \rangle}, \tag{6.10}$$

where the subscript 0 denotes the value at 0 GPa. Positive values of $\log(x/x_0)$ indicate an increase in the value of x as compared to the value at 0 GPa, while negative values indicate a decrease. Note also that for the McMillan-Hopfield parameter $\eta = N(\epsilon_F)\langle g^2 \rangle$, we have $\log(\eta/\eta_0) = \log(N(\epsilon_F)/N(\epsilon_F)_0) + \log(\langle g^2 \rangle / \langle g^2 \rangle_0)$, so that in Fig. 6.11 the sum of the contributions from $N(\epsilon_F)$ and $\langle g^2 \rangle$ equals the contribution from η. As discussed in Ref. [72], η can be considered as an electronic contribution to λ and $\langle \omega^2 \rangle$ a phononic contribution.

Figure 6.11 shows the following effects as pressure is increased. The increase in phonon frequencies acts in the direction of lowering λ. The average matrix elements $\langle g^2 \rangle$ generally increase, but the effect is not as significant as the effects from $N(\epsilon_F)$ and phonon frequencies. For $A7$ As, the dominant cause of the increase in λ is the large increase in $N(\epsilon_F)$, which overcomes the increase in $\langle \omega^2 \rangle$. For *sc* As, it is interesting that the decrease in $N(\epsilon_F)$ with increasing pressure is compensated by the increase in $\langle g^2 \rangle$, so that η is almost constant as a function of pressure. Equivalently, λ is almost proportional to $1/\langle \omega^2 \rangle$; i.e., the dominant effect in the decrease of λ with increasing pressure is the increase in phonon frequency. The overall trend for λ is to increase with pressure in the $A7$ structure, and decrease with pressure in the *sc* structure.

In Fig. 6.12, we compare our calculations for T_c as a function of pressure to experimental results from Chen et al [18]. The calculated values are shifted to the experimental pressures, following the procedure described in Sec. 6.4.1. For Calculations 1A and 2A, we use the EOS parameters from Kikegawa and Iwasaki [231] and Beister et al [232]. , respectively. For each set of points, one point (with calculated pressure 30 GPa) lies within the pressure range for which a finite T_c was experimentally measured by Chen et al. Using the McMillan equation, we adjust μ^* to match the calculated T_c to the experimental value at this pressure. Within each set of points, the same μ^* is used for the other pressures. We obtain $\mu^* = 0.128$ and 0.117 for Calculations 1A and 2A, respectively.

The validity of our results is supported by the fact that these values for μ^* are close to the accepted values for other conventional superconductors [72, 73]. In addition, we find that at pressures below and above the peak in T_c, the calculated T_c is below 1.7 K; this result is consistent with the experiment. However, we note that a transition from *sc* to another structure was observed experimentally at around 48 GPa (Ref. [262]) and is not accounted for in the present calculation.

We also consider how μ^* might change with pressure. We expect μ^* to vary with $N(\epsilon_F)$ as the pressure changes; a reasonable relation is given by a modified Bennemann-

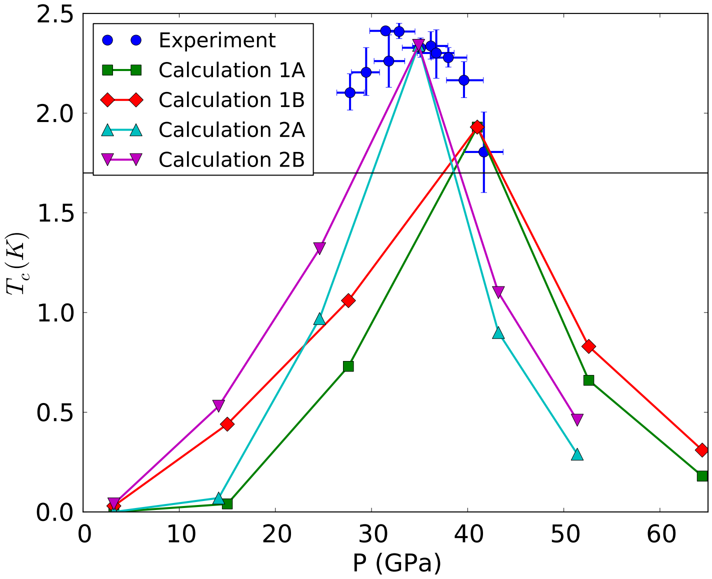

Figure 6.12: Superconducting transition temperature T_c as a function of pressure. Blue circles denote experimental results, with error bars, from Ref. [18]. For the calculated values, the pressure is determined from the experimental Murnaghan equation of state (EOS) parameters, using the calculated volume as input. For Calculations 1A (green squares) and 1B (red diamonds), $\mu^* = 0.128$ at 41 GPa, and the EOS parameters are from Ref. [231]. For Calculation 2A (cyan up-triangles) and 2B (magenta down-triangles), $\mu^* = 0.117$ at 35 GPa, and the EOS parameters are from Ref. [232]. For Calculations 1A and 2A, μ^* is constant for all pressures, while for Calculations 1B and 2B, μ^* varies with pressure according to Eq. 6.11 in the text. The horizontal line at 1.7 K denotes the lower limit of accessible temperatures in the experiment.

Garland formula [263–265]:

$$\mu^* = \frac{CN(\epsilon_F)}{1 + N(\epsilon_F)} \tag{6.11}$$

where C is a constant and $N(\epsilon_F)$ is given in states/eV atom. The effect on T_c is shown in Fig. 6.12. Calculations 1B and 2B are the same as 1A and 2A, respectively, except that μ^* is varied with pressure according to Eq. 6.11, using the calculated $N(\epsilon_F)$ values (Table 6.1). For Calculation 1B (2B), we set $C = 0.57$ (0.52) so that the μ^* of 0.128 (0.117) matches Calculation 1A (2A) at the point with a theoretical pressure of 30 GPa. If this variation in μ^* with pressure is included, the peak in T_c is somewhat broader than if μ^* is taken to be constant, but the results remain consistent with experiment. While the changes with pressure of μ^* and λ have opposite effects on T_c, the changes in λ dominate.

6.6 Conclusion

Our first-principles e-p coupling calculations for As at pressures above and below the $A7$ to *sc* transition show that the peak in T_c is indeed related to the structural transition, as suggested by previous studies. The main factor in the increase in λ and hence T_c with increasing pressure below the transition is the large increase in $N(\epsilon_F)$, while the decrease in λ above the transition is mainly due to the increase in average phonon frequency as pressure increases. The softening and large e-p coupling of the $A7$ Γ_1 optical and *sc* R modes as the transition is approached do not make a large direct contribution to the increase in λ; nevertheless, they play important roles in the peak in T_c because they drive the structural transition. The physical mechanisms discussed here have relevance for e-p coupling in other Group V elements as well [266].

Bibliography

[1] H. W. Kroto, J. R. Heath, S. C. O'Brien, R. F. Curl, and R. E. Smalley, Nature (London) **318**, 162 (1985).

[2] S. Iijima, Nature (London) **354**, 56 (1991).

[3] K. S. Novoselov, A. K. Geim, S. V. Morozov, D. Jiang, Y. Zhang, S. V. Dubonos, I. V. Grigorieva, and A. A. Firsov, Science **306**, 666 (2004).

[4] A. K. Geim and K. S. Novoselov, Nat. Mater. **6**, 183 (2007).

[5] A. K. Geim, Science **324**, 1530 (2009).

[6] N. W. Ashcroft and N. D. Mermin, *Solid State Physics* (New York: Harcourt, Inc., 1976).

[7] S.-W. Cheong and M. Mostovoy, Nat. Mater. **6**, 13 (2007).

[8] R. Ramesh and N. A. Spaldin, Nat. Mater. **6**, 21 (2007).

[9] E. Tsymbal and D. Pettifor, in *Solid State Physics*, edited by H. Ehrenreich and F. Spaepen (Academic Press, 2001), vol. 56, pp. 113 – 237.

[10] D. van Delft and P. Kes, Physics Today **63**, 38 (2010).

[11] J. Bardeen, L. N. Cooper, and J. R. Schrieffer, Phys. Rev. **108**, 1175 (1957).

[12] J. Nagamatsu, N. Nakagawa, T. Muranaka, Y. Zenitani, and J. Akimitsu, Nature (London) **410**, 63 (2001).

[13] K. Shimizu, H. Ishikawa, D. Takao, T. Yagi, and K. Amaya, Nature (London) **419**, 597 (2002).

[14] V. V. Struzhkin, M. I. Eremets, W. Gan, H.-k. Mao, and R. J. Hemley, Science **298**, 1213 (2002).

[15] S. Deemyad and J. S. Schilling, Phys. Rev. Lett. **91**, 167001 (2003).

[16] Y. Zhang, V. W. Brar, C. Girit, A. Zettl, and M. F. Crommie, Nat. Phys. **5**, 722 (2009).

[17] V. W. Brar, R. Decker, H.-M. Solowan, Y. Wang, L. Maserati, K. T. Chan, H. Lee, C. O. Girit, A. Zettl, S. G. Louie, M. L. Cohen, and M. F. Crommie, Nat. Phys. **7**, 43 (2011).

[18] A. L. Chen, S. P. Lewis, Z. Su, P. Y. Yu, and M. L. Cohen, Phys. Rev. B **46**, 5523 (1992).

[19] M. Born and R. Oppenheimer, Annalen der Physik **389**, 457 (1927).

[20] P. Hohenberg and W. Kohn, Phys. Rev. **136**, B864 (1964).

[21] W. Kohn and L. J. Sham, Phys. Rev. **140**, A1133 (1965).

[22] R. M. Martin, *Electronic Structure: Basic Theory and Practical Methods* (New York: Cambridge University Press, 2004).

[23] D. M. Ceperley and B. J. Alder, Phys. Rev. Lett. **45**, 566 (1980).

[24] J. P. Perdew and A. Zunger, Phys. Rev. B **23**, 5048 (1981).

[25] J. P. Perdew, J. A. Chevary, S. H. Vosko, K. A. Jackson, M. R. Pederson, D. J. Singh, and C. Fiolhais, Phys. Rev. B **46**, 6671 (1992).

[26] J. P. Perdew, K. Burke, and M. Ernzerhof, Phys. Rev. Lett. **77**, 3865 (1996).

[27] J. Ihm, A. Zunger, and M. L. Cohen, Journal of Physics C: Solid State Physics **12**, 4409 (1979).

[28] M. L. Cohen, Phys. Scr. **T1**, 5 (1982).

[29] W. E. Pickett, Computer Physics Reports **9**, 115 (1989).

[30] M. L. Cohen, M. Schlüter, J. R. Chelikowsky, and S. G. Louie, Phys. Rev. B **12**, 5575 (1975).

[31] C. Herring, Phys. Rev. **57**, 1169 (1940).

[32] J. C. Phillips and L. Kleinman, Phys. Rev. **116**, 287 (1959).

[33] E. Antončik, Journal of Physics and Chemistry of Solids **10**, 314 (1959).

[34] M. L. Cohen and V. Heine, in *Solid State Physics*, edited by F. S. Henry Ehrenreich and D. Turnbull (Academic Press, 1970), vol. 24, pp. 37 – 248.

[35] J. R. Chelikowsky and M. L. Cohen, Phys. Rev. B **14**, 556 (1976).

[36] D. R. Hamann, M. Schlüter, and C. Chiang, Phys. Rev. Lett. **43**, 1494 (1979).

[37] G. B. Bachelet, D. R. Hamann, and M. Schlüter, Phys. Rev. B **26**, 4199 (1982).

[38] N. Troullier and J. L. Martins, Phys. Rev. B **43**, 1993 (1991).

[39] L. Kleinman and D. M. Bylander, Phys. Rev. Lett. **48**, 1425 (1982).

[40] S. G. Louie, S. Froyen, and M. L. Cohen, Phys. Rev. B **26**, 1738 (1982).

[41] D. Vanderbilt, Phys. Rev. B **41**, 7892 (1990).

[42] P. E. Blöchl, Phys. Rev. B **50**, 17953 (1994).

[43] G. Kresse and D. Joubert, Phys. Rev. B **59**, 1758 (1999).

[44] O. K. Andersen, Phys. Rev. B **12**, 3060 (1975).

[45] P. Giannozzi and S. Baroni, in *Handbook of Materials Modeling*, edited by S. Yip (Springer, 2005), vol. 1, pp. 195–214.

[46] M. T. Yin and M. L. Cohen, Phys. Rev. B **26**, 3259 (1982).

[47] S. Baroni, S. de Gironcoli, A. Dal Corso, and P. Giannozzi, Rev. Mod. Phys. **73**, 515 (2001).

[48] X. Gonze, Phys. Rev. A **52**, 1096 (1995).

[49] X. Gonze, Phys. Rev. B **55**, 10337 (1997).

[50] X. Gonze and C. Lee, Phys. Rev. B **55**, 10355 (1997).

[51] J. Kondo, Progress of Theoretical Physics **32**, 37 (1964).

[52] P. W. Anderson, Phys. Rev. **124**, 41 (1961).

[53] J. Hubbard, Proceedings of the Royal Society of London. Series A, Mathematical and Physical Sciences **276**, 238 (1963).

[54] V. I. Anisimov, J. Zaanen, and O. K. Andersen, Phys. Rev. B **44**, 943 (1991).

[55] M. Cococcioni and S. de Gironcoli, Phys. Rev. B **71**, 035105 (2005).

[56] A. I. Liechtenstein, V. I. Anisimov, and J. Zaanen, Phys. Rev. B **52**, R5467 (1995).

[57] V. I. Anisimov and O. Gunnarsson, Phys. Rev. B **43**, 7570 (1991).

[58] V. I. Anisimov, I. V. Solovyev, M. A. Korotin, M. T. Czyżyk, and G. A. Sawatzky, Phys. Rev. B **48**, 16929 (1993).

[59] V. I. Anisimov, F. Aryasetiawan, and A. I. Lichtenstein, Journal of Physics: Condensed Matter **9**, 767 (1997).

[60] P. Zhang, W. Luo, V. H. Crespi, M. L. Cohen, and S. G. Louie, Phys. Rev. B **70**, 085108 (2004).

[61] H. Fröhlich, Phys. Rev. **79**, 845 (1950).

[62] H. Fröhlich, Proceedings of the Royal Society of London. Series A. Mathematical and Physical Sciences **215**, 291 (1952).

[63] Y. Nambu, Phys. Rev. **117**, 648 (1960).

[64] L. P. Gor'kov, ZhETF **34**, 735 (1958), on the energy spectrum of superconductors, Sov. Phys. JETP 7, 505-508 (1958).

[65] G. M. Eliashberg, Zh. Eksp. Teor. Fiz. **38**, 966 (1960).

[66] J. R. Schrieffer, *Theory of Superconductivity* (New York: Benjamin, 1964).

[67] G. Grimvall, *The Electron-Phonon Interaction in Metals* (New York: North-Holland, 1981).

[68] P. B. Allen and B. Mitrović, in *Solid State Physics*, edited by F. S. Henry Ehrenreich and D. Turnbull (Academic Press, 1983), vol. 37, pp. 1 – 92.

[69] G. D. Mahan, *Many-Particle Physics* (Kluwer Academic / Plenum Publishers, 2000), 3rd ed.

[70] A. B. Migdal, Zh. Eksp. Teor. Fiz. **34**, 1438 (1958).

[71] P. B. Allen, Phys. Rev. B **6**, 2577 (1972).

[72] W. L. McMillan, Phys. Rev. **167**, 331 (1968).

[73] P. B. Allen and R. C. Dynes, Phys. Rev. B **12**, 905 (1975).

[74] P. Morel and P. W. Anderson, Phys. Rev. **125**, 1263 (1962).

[75] K. T. Chan, J. B. Neaton, and M. L. Cohen, Phys. Rev. B **77**, 235430 (2008).

[76] R. Saito, G. Dresselhaus, and M. S. Dresselhaus, *Physical Properties of Carbon Nanotubes* (Imperial College Press, 1998).

[77] R. S. Lee, H. J. Kim, J. E. Fischer, A. Thess, and R. E. Smalley, Nature (London) **388**, 255 (1997).

[78] A. M. Rao, P. C. Eklund, S. Bandow, A. Thess, and R. E. Smalley, Nature (London) **388**, 257 (1997).

[79] M. Radosavljević, J. Appenzeller, P. Avouris, and J. Knoch, Appl. Phys. Lett. **84**, 3693 (2004).

[80] A. Bostwick, T. Ohta, T. Seyller, K. Horn, and E. Rotenberg, Nat. Phys. **3**, 36 (2007).

[81] J.-H. Chen, C. Jang, S. Adam, M. S. Fuhrer, E. D. Williams, and M. Ishigami, Nat. Phys. **4**, 377 (2008).

[82] T. Ohta, A. Bostwick, T. Seyller, K. Horn, and E. Rotenberg, Science **313**, 951 (2006).

[83] Y. Zhang, N. W. Franklin, R. J. Chen, and H. Dai, Chem. Phys. Lett. **331**, 35 (2000).

[84] B. C. Regan, S. Aloni, R. O. Ritchie, U. Dahmen, and A. Zettl, Nature (London) **428**, 924 (2004).

[85] A. Javey, J. Guo, Q. Wang, M. Lundstrom, and H. Dai, Nature (London) **424**, 654 (2003).

[86] Z. Chen, J. Appenzeller, J. Knoch, Y.-M. Lin, and P. Avouris, Nano Lett. **5**, 1497 (2005).

[87] M. Caragiu and S. Finberg, J. Phys.: Condens. Matter **17**, R995 (2005).

[88] E. Durgun, S. Dag, S. Ciraci, and O. Gulseren, J. Phys. Chem. B **108**, 575 (2004).

[89] J. Bormet, J. Neugebauer, and M. Scheffler, Phys. Rev. B **49**, 17242 (1994).

[90] R. D. Diehl and R. McGrath, J. Phys.: Condens. Matter **9**, 951 (1997).

[91] G. Kresse and J. Hafner, Phys. Rev. B **47**, 558 (1993).

[92] G. Kresse and J. Furthmúller, Computational Materials Science **6**, 15 (1996).

[93] G. Kresse and J. Furthmüller, Phys. Rev. B **54**, 11169 (1996).

[94] J. C. Slater, The Journal of Chemical Physics **41**, 3199 (1964).

[95] G. Makov and M. C. Payne, Phys. Rev. B **51**, 4014 (1995).

[96] J. Neugebauer and M. Scheffler, Phys. Rev. B **46**, 16067 (1992).

[97] H. Jónsson, G. Mills, and K. W. Jacobsen, *Classical and Quantum Dynamics in Condensed Phase Simulations* (World Scientific, Singapore, 1998), p. 385.

[98] C. Kittel, *Introduction to Solid Sate Physics* (John Wiley & Sons, Inc., 2005), eighth ed.

[99] F. Valencia, A. H. Romero, F. Ancilotto, and P. L. Silvestrelli, The Journal of Physical Chemistry B **110**, 14832 (2006).

[100] S. Meng and S. Gao, The Journal of Chemical Physics **125**, 014708 (pages 10) (2006).

[101] K. Rytkönen, J. Akola, and M. Manninen, Phys. Rev. B **75**, 075401 (2007).

[102] A. Lugo-Solis and I. Vasiliev, Phys. Rev. B **76**, 235431 (2007).

[103] F. J. Ribeiro, J. B. Neaton, S. G. Louie, and M. L. Cohen, Phys. Rev. B **72**, 075302 (2005).

[104] E. Ganz, K. Sattler, and J. Clarke, Surface Science **219**, 33 (1989).

[105] V. Maurice and P. Marcus, Surface Science **275**, 65 (1992).

[106] S. Srivastava and J. Almöf, Surface Science **274**, 113 (1992).

[107] I. Moullet, Surface Science **331–333, Part A**, 697 (1995).

[108] Q. Ma and R. A. Rosenberg, Surface Science **391**, L1224 (1997).

[109] Z. Zhu, G. Lu, and F. Wang, J. Phys. Chem. B **109**, 7923 (2005).

[110] P. Lindan, E. Duplock, C. Zhang, M. Thomas, R. Chatten, and A. Chadwick, Dalton Trans. pp. 3076–3084 (2004).

[111] M. I. Rojas and E. P. M. Leiva, Phys. Rev. B **76**, 155415 (2007).

[112] Y. Yagi, T. M. Briere, M. H. F. Sluiter, V. Kumar, A. A. Farajian, and Y. Kawazoe, Phys. Rev. B **69**, 075414 (2004).

[113] Q. Ma and R. A. Rosenberg, Phys. Rev. B **60**, 2827 (1999).

[114] P. Jensen, X. Blase, and P. Ordejn, Surface Science **564**, 173 (2004).

[115] J. Akola and H. Häkkinen, Phys. Rev. B **74**, 165404 (2006).

[116] G. M. Wang, J. J. BelBruno, S. D. Kenny, and R. Smith, Phys. Rev. B **69**, 195412 (2004).

[117] W. C. Martin and W. L. Wiese, *Atomic, Molecular, & Optical Physics Handbook* (American Institute of Physics, 1996), pp. 135–153.

[118] F. Ancilotto and F. Toigo, Phys. Rev. B **47**, 13713 (1993).

[119] D. Lamoen and B. N. J. Persson, J. Chem. Phys. **108**, 3332 (1998).

[120] L. Lou, L. Österlund, and B. Hellsing, J. Chem Phys. **112**, 4788 (2000).

[121] Z. Y. Li, K. M. Hock, R. E. Palmer, and J. F. Annett, J. Phys.: Condens. Matter **3**, S103 (1991).

[122] P. Bennich, C. Puglia, P. A. Brühwiler, A. Nilsson, A. J. Maxwell, A. Sandell, N. Mårtensson, and P. Rudolf, Phys. Rev. B **59**, 8292 (1999).

[123] J. Algdal, M. Breitholtz, T. Kihlgren, S.-A. . Lindgren, and L. Walldén, Phys. Rev. B **73**, 165409 (2006).

[124] S. Suzuki, C. Bower, Y. Watanabe, and O. Zhou, Appl. Phys. Lett. **76**, 4007 (2000).

[125] V. Barone, J. E. Peralta, J. Uddin, and G. E. Scuseria, J. Chem. Phys. **124**, 024709 (2006).

[126] G. A. Somorjai, *Introduction to Surface Chemistry and Catalysis* (John Wiley & Sons, Inc., 1994).

[127] Z. Y. Li, K. M. Hock, and R. E. Palmer, Phys. Rev. Lett. **67**, 1562 (1991).

[128] K. Hock and R. Palmer, Surface Science **284**, 349 (1993).

[129] L. Österlund, D. Chakarov, and B. Kasemo, Surface Science **420**, 174 (1999).

[130] K. T. Chan, H. Lee, and M. L. Cohen, Phys. Rev. B **83**, 035405 (2011).

[131] K. S. Novoselov, D. Jiang, F. Schedin, T. J. Booth, V. V. Khotkevich, S. V. Morozov, and A. K. Geim, Proceedings of the National Academy of Sciences of the United States of America **102**, 10451 (2005).

[132] J. C. Meyer, A. K. Geim, M. I. Katsnelson, K. S. Novoselov, T. J. Booth, and S. Roth, Nature (London) **446**, 60 (2007).

[133] C. Berger, Z. Song, T. Li, X. Li, A. Y. Ogbazghi, R. Feng, Z. Dai, A. N. Marchenkov, E. H. Conrad, P. N. First, and W. A. de Heer, The Journal of Physical Chemistry B **108**, 19912 (2004).

[134] A. Reina, X. Jia, J. Ho, D. Nezich, H. Son, V. Bulovic, M. S. Dresselhaus, and J. Kong, Nano Lett. **9**, 30 (2009).

[135] K. S. Kim, Y. Zhao, H. Jang, S. Y. Lee, J. M. Kim, K. S. Kim, J.-H. Ahn, P. Kim, J.-Y. Choi, and B. H. Hong, Nature (London) **457**, 706 (2009).

[136] Z. H. Ni, T. Yu, Y. H. Lu, Y. Y. Wang, Y. P. Feng, and Z. X. Shen, ACS Nano **2**, 2301 (2008).

[137] T. M. G. Mohiuddin, A. Lombardo, R. R. Nair, A. Bonetti, G. Savini, R. Jalil, N. Bonini, D. M. Basko, C. Galiotis, N. Marzari, K. S. Novoselov, A. K. Geim, *et al.*, Phys. Rev. B **79**, 205433 (2009).

[138] M. Y. Han, B. Özyilmaz, Y. Zhang, and P. Kim, Phys. Rev. Lett. **98**, 206805 (2007).

[139] X. Li, X. Wang, L. Zhang, S. Lee, and H. Dai, Science **319**, 1229 (2008).

[140] L. A. Ponomarenko, F. Schedin, M. I. Katsnelson, R. Yang, E. W. Hill, K. S. Novoselov, and A. K. Geim, Science **320**, 356 (2008).

[141] K. S. Novoselov, E. McCann, S. V. Morozov, V. I. Fal'ko, M. I. Katsnelson, U. Zeitler, D. Jiang, F. Schedin, and A. K. Geim, Nat. Phys. **2**, 177 (2006).

[142] A. Das, S. Pisana, B. Chakraborty, S. Piscanec, S. K., Saha, W. U.V., K. Novoselov, H. Krishnamurthy, A. Geim, A. Ferrari, and A. Sood, Nat. Nano. **3**, 210 (2008).

[143] D. K. Efetov and P. Kim, Phys. Rev. Lett. **105**, 256805 (2010).

[144] K. S. Novoselov, A. K. Geim, S. V. Morozov, D. Jiang, M. I. Katsnelson, I. V. Grigorieva, S. V. Dubonos, and A. A. Firsov, Nature (London) **438**, 197 (2005).

[145] Y. Zhang, Y.-W. Tan, H. L. Stormer, and P. Kim, Nature (London) **438**, 201 (2005).

[146] I. Gierz, C. Riedl, U. Starke, C. R. Ast, and K. Kern, Nano Lett. **8**, 4603 (2008).

[147] F. Schedin, A. K. Geim, S. V. Morozov, E. W. Hill, P. Blake, M. I. Katsnelson, and K. S. Novoselov, Nat. Mater. **6**, 652 (2007).

[148] D. A. Dikin, S. Stankovich, E. J. Zimney, R. D. Piner, G. H. B. Dommett, G. Evmenenko, S. T. Nguyen, and R. S. Ruoff, Nature (London) **448**, 457 (2007).

[149] D. C. Elias, R. R. Nair, T. M. G. Mohiuddin, S. V. Morozov, P. Blake, M. P. Halsall, A. C. Ferrari, D. W. Boukhvalov, M. I. Katsnelson, A. K. Geim, and K. S. Novoselov, Science **323**, 610 (2009).

[150] A. H. Castro Neto, F. Guinea, N. M. R. Peres, K. S. Novoselov, and A. K. Geim, Rev. Mod. Phys. **81**, 109 (2009).

[151] K. Sengupta and G. Baskaran, Phys. Rev. B **77**, 045417 (2008).

[152] J. Chen, W. G. Cullen, E. D. Williams, and M. S. Fuhrer, ArXiv e-prints (2010).

[153] N. A. Pradhan, N. Liu, C. Silien, and W. Ho, Phys. Rev. Lett. **94**, 076801 (2005).

[154] G. V. Nazin, X. H. Qiu, and W. Ho, Phys. Rev. Lett. **95**, 166103 (2005).

[155] F. Marczinowski, J. Wiebe, F. Meier, K. Hashimoto, and R. Wiesendanger, Phys. Rev. B **77**, 115318 (2008).

[156] K. Teichmann, M. Wenderoth, S. Loth, R. G. Ulbrich, J. K. Garleff, A. P. Wijnheijmer, and P. M. Koenraad, Phys. Rev. Lett. **101**, 076103 (2008).

[157] P. Giannozzi, S. Baroni, N. Bonini, M. Calandra, R. Car, C. Cavazzoni, D. Ceresoli, G. L. Chiarotti, M. Cococcioni, I. Dabo, A. D. Corso, S. de Gironcoli, *et al.*, J. Phys. Condens. Matter **21**, 395502 (2009).

[158] L. Bengtsson, Phys. Rev. B **59**, 12301 (1999).

[159] P. Gava, M. Lazzeri, A. M. Saitta, and F. Mauri, Phys. Rev. B **79**, 165431 (2009).

[160] M. S. Dresselhaus and G. Dresselhaus, Advances in Physics **30**, 139 (1981).

[161] T. O. Wehling, H. P. Dahal, A. I. Lichtenstein, M. I. Katsnelson, H. C. Manoharan, and A. V. Balatsky, Phys. Rev. B **81**, 085413 (2010).

[162] T. O. Wehling, A. V. Balatsky, M. I. Katsnelson, A. I. Lichtenstein, and A. Rosch, Phys. Rev. B **81**, 115427 (2010).

[163] D. Jacob and G. Kotliar, Phys. Rev. B **82**, 085423 (2010).

[164] K. Saha, I. Paul, and K. Sengupta, Phys. Rev. B **81**, 165446 (2010).

[165] B. Uchoa, L. Yang, S.-W. Tsai, N. M. R. Peres, and A. H. Castro Neto, Phys. Rev. Lett. **103**, 206804 (2009).

[166] H.-B. Zhuang, Q.-F. Sun, and X. C. Xie, Europhys. Lett. **86**, 58004 (2009).

[167] Z.-G. Zhu, K.-H. Ding, and J. Berakdar, Europhys. Lett. **90**, 67001 (2010).

[168] Y. Mao, J. Yuan, and J. Zhong, Journal of Physics: Condensed Matter **20**, 115209 (2008).

[169] C. Cao, M. Wu, J. Jiang, and H.-P. Cheng, Phys. Rev. B **81**, 205424 (2010).

[170] M. Ishigami, J. H. Chen, W. G. Cullen, M. S. Fuhrer, and E. D. Williams, Nano Lett. **7**, 1643 (2007).

[171] H. Lee, W. I. Choi, and J. Ihm, Phys. Rev. Lett. **97**, 056104 (2006).

[172] K. T. Chan, H. Lee, and M. L. Cohen, Phys. Rev. B **84**, 165419 (2011).

[173] M. A. Kastner, Rev. Mod. Phys. **64**, 849 (1992).

[174] D. Goldhaber-Gordon, H. Shtrikman, D. Mahalu, D. Abusch-Magder, U. Meirav, and M. A. Kastner, Nature (London) **391**, 156 (1998).

[175] S. M. Cronenwett, T. H. Oosterkamp, and L. P. Kouwenhoven, Science **281**, 540 (1998).

[176] W. Liang, M. P. Shores, M. Bockrath, J. R. Long, and H. Park, Nature (London) **417**, 725 (2002).

[177] S. Kubatkin, A. Danilov, M. Hjort, J. Cornil, J.-L. Bredas, N. Stuhr-Hansen, P. Hedegard, and T. Bjornholm, Nature (London) **425**, 698 (2003).

[178] J. Park, A. N. Pasupathy, J. I. Goldsmith, C. Chang, Y. Yaish, J. R. Petta, M. Rinkoski, J. P. Sethna, H. D. Abruna, P. L. McEuen, and D. C. Ralph, Nature (London) **417**, 722 (2002).

[179] G. P. Lansbergen, R. Rahman, C. J. Wellard, I. Woo, J. Caro, N. Collaert, S. Biesemans, G. Klimeck, L. C. L. Hollenberg, and S. Rogge, Nat. Phys. **4**, 656 (2008).

[180] G. P. Lansbergen, G. C. Tettamanzi, J. Verduijn, N. Collaert, S. Biesemans, M. Blaauboer, and S. Rogge, Nano Lett. **10**, 455 (2010), pMID: 20041698.

[181] A. Morello, J. J. Pla, F. A. Zwanenburg, K. W. Chan, K. Y. Tan, H. Huebl, M. Mottonen, C. D. Nugroho, C. Yang, J. A. van Donkelaar, A. D. C. Alves, D. N. Jamieson, *et al.*, Nature (London) **467**, 687 (2010).

[182] A. M. Suarez, L. R. Radovic, E. Bar-Ziv, and J. O. Sofo, Phys. Rev. Lett. **106**, 146802 (2011).

[183] J. O. Sofo, A. M. Suarez, G. Usaj, P. S. Cornaglia, A. D. Hernández-Nieves, and C. A. Balseiro, Phys. Rev. B **83**, 081411 (2011).

[184] H. Valencia, A. Gil, and G. Frapper, J. Phys. Chem. C **114**, 14141 (2010).

[185] M. Leslie and N. J. Gillan, Journal of Physics C: Solid State Physics **18**, 973 (1985).

[186] A. Y. Lozovoi, A. Alavi, J. Kohanoff, and R. M. Lynden-Bell, The Journal of Chemical Physics **115**, 1661 (2001).

[187] I. Dabo, B. Kozinsky, N. E. Singh-Miller, and N. Marzari, Phys. Rev. B **77**, 115139 (2008).

[188] A. Baldereschi, S. Baroni, and R. Resta, Phys. Rev. Lett. **61**, 734 (1988).

[189] P.-O. Löwdin, J. Chem. Phys. **18**, 365 (1950).

[190] M. Otani and O. Sugino, Phys. Rev. B **73**, 115407 (2006).

[191] P. A. Schultz, Phys. Rev. B **60**, 1551 (1999).

[192] P. A. Schultz, Phys. Rev. Lett. **84**, 1942 (2000).

[193] P. E. Blochl, The Journal of Chemical Physics **103**, 7422 (1995).

[194] C. L. Fu and K. M. Ho, Phys. Rev. Lett. **63**, 1617 (1989).

[195] K. P. Bohnen and D. M. Kolb, Surface Science **407**, L629 (1998).

[196] S. Heinze, X. Nie, S. Blgel, and M. Weinert, Chemical Physics Letters **315**, 167 (1999).

[197] A. Y. Lozovoi and A. Alavi, Phys. Rev. B **68**, 245416 (2003).

[198] J.-S. Filhol and M. Neurock, Angewandte Chemie **118**, 416 (2006).

[199] S. Kajita, T. Nakayama, and J. Yamauchi, Journal of Physics: Conference Series **29**, 120 (2006).

[200] C. D. Taylor, S. A. Wasileski, J.-S. Filhol, and M. Neurock, Phys. Rev. B **73**, 165402 (2006).

[201] S. Schnur and A. Groß, Catalysis Today **165**, 129 (2011), theoretical Catalysis for Energy Production and Utilization: from First Principles Theory to Microkinetics.

[202] H. Lee, J. Ihm, M. L. Cohen, and S. G. Louie, Nano Lett. **10**, 793 (2010), pMID: 20104855.

[203] K. T. Chan, J. D. Sau, P. Zhang, and M. L. Cohen, Phys. Rev. B **75**, 054304 (2007).

[204] S. Massidda, M. Posternak, A. Baldereschi, and R. Resta, Phys. Rev. Lett. **82**, 430 (1999).

[205] J.-H. Lee, Y.-C. Hsue, and A. J. Freeman, Phys. Rev. B **73**, 172405 (2006).

[206] O. Tchernyshyov, R. Moessner, and S. L. Sondhi, Phys. Rev. B **66**, 064403 (2002).

[207] F. Ye, Y. Ren, Q. Huang, J. A. Fernandez-Baca, P. Dai, J. W. Lynn, and T. Kimura, Phys. Rev. B **73**, 220404(R) (2006).

[208] K. E. Sickafus, J. M. Wills, and N. W. Grimes, J. Am. Ceram. Soc. **82**, 3279 (1999).

[209] J. B. Goodenough, Phys. Rev. **117**, 1442 (1960).

[210] K. Motida and S. Miyahara, J. Phys. Soc. Jpn. **28**, 1188 (1970).

[211] S.-H. Lee, C. Broholm, T. H. Kim, W. Ratcliff II, and S.-W. Cheong, Phys. Rev. Lett. **84**, 3718 (2000).

[212] R. Moessner and J. T. Chalker, Phys. Rev. Lett. **80**, 2929 (1998).

[213] A. B. Sushkov, O. Tchernyshyov, W. Ratcliff II, S. W. Cheong, and H. D. Drew, Phys. Rev. Lett. **94**, 137202 (2005).

[214] C. J. Fennie and K. M. Rabe, Phys. Rev. Lett. **96**, 205505 (2006).

[215] A. Toropova, G. Kotliar, S. Y. Savrasov, and V. S. Oudovenko, Phys. Rev. B **71**, 172403 (2005).

[216] A. Dal Corso and S. de Gironcoli, Phys. Rev. B **62**, 273 (2000).

[217] F. Favot and A. Dal Corso, Phys. Rev. B **60**, 11427 (1999).

[218] B. G. Pfrommer, M. Coté, S. G. Louie, and M. L. Cohen, J. Comput. Phys. **131**, 233 (1997).

[219] B. G. Pfrommer, J. Demmel, and H. Simon, J. Comp. Phys. **150**, 287 (1999).

[220] H. J. Monkhorst and J. D. Pack, Phys. Rev. B **13**, 5188 (1976).

[221] M. A. Korotin, V. I. Anisimov, D. I. Khomskii, and G. A. Sawatzky, Phys. Rev. Lett. **80**, 4305 (1998).

[222] C. J. Fennie and K. M. Rabe, Phys. Rev. B **72**, 214123 (2005).

[223] H. S. C. O'Neill and W. A. Dollase, Phys. Chem. Miner. **20**, 541 (1994).

[224] J. Himmrich and H. Lutz, Solid State Communications **79**, 447 (1991).

[225] S. Tinte, M. G. Stachiotti, C. O. Rodriguez, D. L. Novikov, and N. E. Christensen, Phys. Rev. B **58**, 11959 (1998).

[226] A. Dal Corso, S. Baroni, and R. Resta, Phys. Rev. B **49**, 5323 (1994).

[227] W. Luo, P. Zhang, and M. L. Cohen, unpublished.

[228] W. Baltensperger and J. S. Helman, Helv. Phys. Acta **41**, 668 (1968).

[229] K. T. Chan, B. D. Malone, and M. L. Cohen, Phys. Rev. B **86**, 094515 (2012).

[230] C. Buzea and K. Robbie, Superconductor Science and Technology **18**, R1 (2005).

[231] T. Kikegawa and H. Iwasaki, Journal of the Physical Society of Japan **56**, 3417 (1987).

[232] H. J. Beister, K. Strössner, and K. Syassen, Phys. Rev. B **41**, 5535 (1990).

[233] M. H. Cohen, L. M. Falicov, and S. Golin, IBM Journal of Research and Development **8**, 215 (1964).

[234] R. J. Needs, R. M. Martin, and O. H. Nielsen, Phys. Rev. B **33**, 3778 (1986).

[235] K. J. Chang and M. L. Cohen, Phys. Rev. B **33**, 7371 (1986).

[236] L. F. Mattheiss, D. R. Hamann, and W. Weber, Phys. Rev. B **34**, 2190 (1986).

[237] S. Shang, Y. Wang, H. Zhang, and Z.-K. Liu, Phys. Rev. B **76**, 052301 (2007).

[238] I. V. Berman and N. B. Brandt, Pis'ma Zh. Eksp Teor. Fiz. **10**, 88 (1969).

[239] H. Kawamura and J. Wittig, Physica B+C **135**, 239 (1985).

[240] D. Kasinathan, J. Kuneš, A. Lazicki, H. Rosner, C. S. Yoo, R. T. Scalettar, and W. E. Pickett, Phys. Rev. Lett. **96**, 047004 (2006).

[241] T. Bazhirov, J. Noffsinger, and M. L. Cohen, Phys. Rev. B **82**, 184509 (2010).

[242] T. Bazhirov, J. Noffsinger, and M. L. Cohen, Phys. Rev. B **84**, 125122 (2011).

[243] F. Giustino, M. L. Cohen, and S. G. Louie, Phys. Rev. B **76**, 165108 (2007).

[244] J. Noffsinger, F. Giustino, B. D. Malone, C.-H. Park, S. G. Louie, and M. L. Cohen, Computer Physics Communications **181**, 2140 (2010).

[245] D. Schiferl and C. S. Barrett, Journal of Applied Crystallography **2**, 30 (1969).

[246] R. J. Needs, R. M. Martin, and O. H. Nielsen, Phys. Rev. B **35**, 9851 (1987).

[247] K. Seifert, J. Hafner, J. Furthmuller, and G. Kresse, Journal of Physics: Condensed Matter **7**, 3683 (1995).

[248] C. R. da Silva and R. M. Wentzcovitch, Computational Materials Science **8**, 219 (1997).

[249] U. Häussermann, K. Söderberg, and R. Norrestam, Journal of the American Chemical Society **124**, 15359 (2002), pMID: 12487611.

[250] M. Durandurdu, Phys. Rev. B **72**, 073208 (2005).

[251] W. Feng, S. Cui, H. Hu, and H. Liu, Physica B: Condensed Matter **400**, 22 (2007).

[252] P. Silas, J. R. Yates, and P. D. Haynes, Phys. Rev. B **78**, 174101 (2008).

[253] E. S. Zijlstra, N. Huntemann, and M. E. Garcia, New Journal of Physics **10**, 033010 (2008).

[254] M. Methfessel and A. T. Paxton, Phys. Rev. B **40**, 3616 (1989).

[255] N. Marzari and D. Vanderbilt, Phys. Rev. B **56**, 12847 (1997).

[256] I. Souza, N. Marzari, and D. Vanderbilt, Phys. Rev. B **65**, 035109 (2001).

[257] A. A. Mostofi, J. R. Yates, Y.-S. Lee, I. Souza, D. Vanderbilt, and N. Marzari, Computer Physics Communications **178**, 685 (2008).

[258] F. D. Murnaghan, Proceedings of the National Academy of Sciences **30**, 244 (1944).

[259] B. Palanivel, M. Rajagopalan, and S. Natarajan, High Pressure Research **10**, 469 (1992).

[260] W. Reichardt and K. H. Rieder, in *Proceedings of the Conference on Neutron Scattering: Gatlinburg, Tennessee*, edited by R. M. Moon (Energy Research and Development Administration, 1976), vol. 1, p. 181.

[261] J. E. Moussa and M. L. Cohen, Phys. Rev. B **74**, 094520 (2006).

[262] R. G. Greene, H. Luo, and A. L. Ruoff, Phys. Rev. B **51**, 597 (1995).

[263] D. Papaconstantopoulos and B. Klein, Physica B+C **107**, 725 (1981).

[264] K. H. Bennemann and J. W. Garland, AIP Conference Proceedings **4**, 103 (1972).

[265] J. W. Garland and K. H. Bennemann, AIP Conference Proceedings **4**, 255 (1972).

[266] B. D. Malone, K. T. Chan, and M. L. Cohen, unpublished.